Prediction of breakdown pressures and fracture propagation surfaces in a rock material subjected to hydraulic fracturing using intact specimens and specimens with a replicated crack

By

Adam Karl Schwartzkopff

The School of Civil, Environmental and Mining Engineering

THE UNIVERSITY of ADELAIDE

This thesis is submitted in fulfilment of the requirements for the degree of

Doctor of Philosophy

in the Faculty of Engineering, Computer and Mathematical Sciences

January 2017

Abstract

Hydraulic fracturing is a mechanical process widely implemented by many resource industries to change the properties of rock material below the surface of the Earth. This method induces fracturing in a rock mass by injecting highly pressurised fluid into the crust. These resultant fractures can enhance the rock permeability and hence increase the efficiency of hydrocarbon extraction and geothermal energy production. Rock masses have pre-existing discontinuities, which act as weak planes for hydraulic fracturing. As such, the ability to predict the fracture propagation resulting from the interaction between these pre-existing cracks and the pressurised fluid is important to design effective hydraulic fracturing treatments. In addition, the maximum internal fluid pressure that the rock can withstand during this process provides an important parameter to assist these predictions. Therefore, the main research reported in the thesis focuses on the prediction of the hydraulic fracture propagation surfaces from the pre-existing cracks intersecting a pressurised section of a borehole, as well as the prediction of the maximum internal breakdown pressures of intact and discontinuous brittle rock materials.

The prediction of the propagation of arbitrarily orientated, pressurised cracks has been addressed by various numerical methods. However, published research on the crack propagation prediction using three dimensional analytical techniques is very limited. One such technique is proposed in this research, which only uses trivial computational time compared with other numerical simulations. This method could assist the design of hydraulic fracturing stimulations by providing a solution quickly for industry. The proposed analytical approach has been validated against a numerical method to ensure accuracy. Studies showed that the predicted propagating crack consistently realigned eventually perpendicular to the minor principal stress direction after the initial tortuous propagation that is dependent on the crack configuration and in-situ stress conditions.

In addition, there has been limited experimental research conducted to investigate the behaviour of pre-existing cracks intersecting a pressurised borehole section. In this research, a comprehensive set of experiments were conducted aiming to quantify the influence of the shear stress on the breakdown pressures and the resultant propagation surfaces of a circular crack intersecting a borehole. The study showed that by increasing the induced shear stress, produced by the combination of different external triaxial stresses, the realignment process of the hydraulic fracture propagation surface occurred more rapidly. However, it was found that under the shear stress conditions tested, this component had little influence on the measured breakdown pressures.

For the prediction of breakdown pressure, a new approach based on the theory of critical distances is proposed in this research. The proposed method assumes that a pressurised crack is formed at a critical distance into the material prior to the unstable crack propagation. The breakdown pressure is calculated using an analytical approximation of the mode I stress intensity factor for this pressurised crack, which significantly reduces the complexity of the prediction. The prediction using the proposed approach aligns well with the measurement in our experiments as well as with published results from other hydraulic fracturing experiments performed externally.

Acknowledgements

I thank my supervisors, Dr Nouné Sophie Melkoumian and A. Prof. Chaoshui Xu, for their belief in my work and in me. I am appreciative of the laboratory staff members that have contributed to the experiments: in particular, Adam Ryntjes and Simon Golding.

This thesis is dedicated to my ‘family’. I define ‘family’ by the people who care or have cared for me. Therefore, this includes many people. However, I have to name a few people that have helped me complete this thesis and through the difficulties of research. I thank my partner, June Sim, for her patience and love. I will always be grateful for the support from my mum, Jude Schwartzkopff. I would also like to acknowledge the strong bond that developed between my colleagues and friends. In particular, Arash Mir and Thomas Bruning, thank you for the discussions and the time we have spent together.

I am appreciative that I have had this opportunity and I acknowledge all the people who have contributed to my education.

Declaration

I certify that this work contains no material which has been accepted for the award of any other degree or diploma, in my name in any university or other tertiary institution and, to the best of my knowledge and belief, contains no material previously published or written by another person, except where due reference has been made in the text. In addition, I certify that no part of this work will, in the future, be used in a submission in my name for any other degree or diploma in any university or other tertiary institution without the prior approval of the University of Adelaide and where applicable, any partner institution responsible for the joint award of this degree.

I give consent to this copy of my thesis, when deposited in the library of the University of Adelaide, being made available for loan and photocopying, subject to the provisions of the Copyright Act 1968.

The author acknowledges that copyright of published works contained within this thesis resides with the copyright holder(s) of those works.

I also give permission for the digital version of my thesis to be made available on the web, via the University's digital research repository, the Library Search and also through web search engines, unless permission has been granted by the University of Adelaide to restrict access for a period of time.

Adam Karl Schwartzkopff

18 January 2017

Table of contents

Introduction

Hydraulic fracturing is a mechanical process whereby pressurised fluid causes unstable fracture propagations into a rock mass. These generated fractures alter the properties of the rock mass, including its permeability, strength and anisotropy. Hydraulic fracturing can occur by natural processes. However, since the early 1950s this mechanical process has been utilised by the hydrocarbon extraction, geothermal, mining and other related industries to take advantage of these altered rock mass properties (Fjær *et al.* 2008).

Increasing the permeability of the rock mass is the primary objective of hydraulic fracturing stimulations (Solberg *et al.* 1980). The hydraulic fracturing process increases permeability by producing new fractures in the rock and enhancing pre-existing discontinuities (Zhang and Chen 2010). The structural defects present in the rock mass (including fractures, joints, faults, fissures and bedding planes) before hydraulic fracturing is commenced can produce resultant fracture surfaces that are complex (Hossain and Rahman 2008). Since fluid and gas conductivity of the rock mass is governed primarily by these stimulated fractures, it is important to predict the resultant fracture geometry (Zhang *et al.* 2011). Validated predictions enable better design of hydraulic fracturing stimulations and mitigate the perceived risk that the resultant fracture geometry may intersect water reservoirs (Vengosh *et al.* 2014). This process is hence important to increase the oil and gas recovery from low permeability reservoirs with hydrocarbon resources (Gupta and Duarte 2014) and to create an efficient heat exchange pathway in low permeability hot dry rock masses in enhanced geothermal systems (Frash *et al.* 2014). Additional oil and gas is produced from stimulated fractures allowing reservoir fluid in the rock mass to flow into the production well. Enhanced geothermal energy extraction requires the linking of the fracture geometry between at least two wells (Ghassemi 2012). Therefore, it is of great importance to be able to predict the shape, orientation and roughness of the produced hydraulic fracture, especially for unconventional energy applications.

Mining operations use hydraulic fracturing to reduce the overall strength of the rock mass. Block caving operations use hydraulic fracturing to precondition the rock mass to allow better fragmentation (Jeffrey *et al.* 2001a). In addition, the hydraulic fracturing process is used to predict the stress regime of the rock mass (Haimson and Cornet 2003). For these applications, it is important to understand the hydraulic fracturing process in order to predict properly the fragmentation effects with preconditioning and to assess the stress regime of rock masses.

For the estimation of the stress regime of rock masses, it is essential to have a good understanding of the pressure that initiates unstable fracture propagation in an intact rock. In addition, the pressure that causes unstable propagation of a pre-existing discontinuity is a major factor that will affect the non-planar fracture surface geometry. Hence, one of the major aims of this research is to derive techniques that can provide a closer prediction to the measured breakdown pressures that causes unstable hydraulic fracture propagation in intact and fractured rocks as well as the resultant fracture propagation surface. In particular, the techniques developed in this research are within the regime of linear elastic fracture mechanics (LEFM) theories, although some concepts of the fracture process zone are used.

1.1 State of the art knowledge and historical contributions

The following sections provide the background to the conducted research. First, an introduction to the literature is provided to relate the work, presented in this thesis, to the resource industries. The general concepts used in this research are then discussed, and subsequently detailed literature review is provided. The latter includes discussions on the three main topics covered by this work, namely breakdown pressure prediction of an intact rock, breakdown pressure prediction of a specimen with a replicated crack, and prediction of non-planar fracture propagation surfaces resulting from hydraulic fracturing. Finally, a conclusion section is presented to illustrate how the three main topics are related.

1.1.1 Introduction and review of industrial importance

The initial conditions from hydraulic fracturing, i.e. the internal pressure and fracture propagation surfaces, require closer predictions to accurately model its effect on a rock mass. These predictions are important since resource industries use the hydraulic fracturing technique for various applications such as fracturing of hydrocarbon reservoirs; producing heat from geothermal reservoirs; artificially weakening a rock mass to induce caving or relieve stress; and for measuring in-situ stresses (Adachi *et al.* 2007).

Hydrocarbons account for about 63% of global energy consumption, with oil and gas accounting for 36% and 27%, respectively (Caineng et al. 2010). Unconventional hydrocarbon reservoirs account for a large amount of global hydrocarbon production. For example, in the United States of America about 46% of gas production is from unconventional resources (Holditch and Madani 2010). Unconventional gas and oil reserves cannot be extracted by the technology usually used for the conventional reserves, because of technical and/or economic reasons. The boundary between

conventional and unconventional resources depends on the access and availability of a technology to the region, geography and market prices. Technology advancement is one of the major factors affecting the definition of this boundary and shifting it between the conventional and unconventional resources. Unconventional natural gas requires elaborate drilling technologies and well stimulation (i.e., hydraulic fracturing) or liquid-gas and gas-gas separation equipment (Rogner 1997). Therefore, understanding the hydraulic fracturing process is important to enhance these unconventional hydrocarbon reserves.

Geothermal energy, which is essentially natural heat of the earth, is an abundant renewable energy resource (Ghassemi 2012). At the end of 2010, geothermal resources were utilised in 24 countries and had a combined capacity of 10,898 MW, resulting in 67,246 GWh of electricity produced. In general, the heat at the base of the continental crust is estimated to be between 200°C and 1,000°C. The interior heat from the centre of the earth, where it is estimated to be in the order of 3,500°C to 4,500°C, is transferred to the surface by conduction. Temperatures rise with increasing depth in the crust on an average of 25°C to 30°C per km (Fridleifsson and Freeston 1994). The energy extracted from these geothermal systems by reducing the in-situ temperature by 1°C from one cubic kilometre of rock it is equivalent to the energy content of 70 kt of coal (Smith 1973).

Naturally fractured hydrothermal systems are the easiest geothermal resources to extract heat from, but they are limited and are restricted to certain regions. These hydrothermal systems are difficult to discover and are a risky investment (Fridleifsson and Freeston 1994). Conversely, engineering conditions underground generally are less risky in terms of costs and assist the expansion of the available global resource (Majer *et al.* 2007). The enhanced geothermal systems are engineered subsurface heat exchangers modified to either extract geothermal energy from sub-economic reservoirs via conventional production methods, or increase the rate and amount of heat transfer of economic reservoirs (Majer *et al.* 2007). For these heat exchangers to be economic they need to be efficient in producing electricity and heat for human use (Häring *et al.* 2008). In these systems, energy is produced by passing fluid into injection well(s) where the heat is exchanged to this fluid inside the discontinuities of the rock mass. This injection fluid transfers to the production wells, where at the surface the heat is depleted. This cooled fluid is then injected back continuously into the injection well(s) (see Fig. 1).

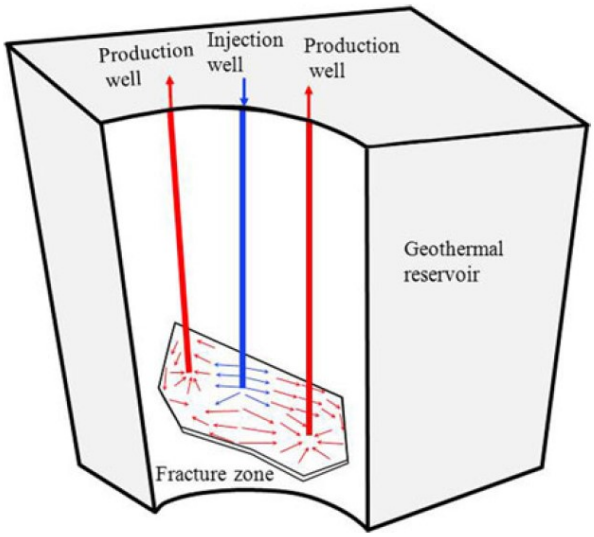

Fig. 1 Engineered geothermal system illustration (from Ghassemi 2012)

One natural mechanism increasing the permeability is when the rock cools. This transfer of heat from the rock to the injection fluid dissolves some minerals (Charlez *et al.* 1996), thus exposing more hot rock mass for heat exchange (Majer *et al.* 2007). However, in some cases this natural mechanism does not provide enough permeability hence these systems can be enhanced by a combination of the following (Allis 1982; Batra *et al.* 1984; Beauce *et al.* 1991; Fehler 1989):

- Hydraulic fracturing (Sharma *et al.* 2004)
- High rate water injection
- Chemical stimulations (Bartko *et al.* 2003; Hardin *et al.* 2003; Nami *et al.* 2008; Rae and di Lullo 2003).

The permeability of geothermal systems must be much higher than for oil wells (Fridleifsson and Freeston 1994). Hence, hydraulic fracturing is an important method utilised in engineered geothermal systems.

Preconditioning is used in cave mining to artificially weaken an orebody to induce caving. These hydraulic fracturing treatments assist the fragmentation and therefore the flow of rock into the draw points under the orebody. These stimulations are also implemented when the caving process arrests (Araneda *et al.* 2007; Catalan *et al.* 2012; Jeffrey 2000; Jeffrey and Mills 2000; van As *et al.* 2004; van As and Jeffrey 2000). In addition, in coal mining hydraulic fracturing is used to increase coal seam permeability (Puri *et al.* 1991a; Puri *et al.* 1991b; Wright *et al.* 1995; Zhai *et al.* 2012). To achieve these stimulations, boreholes are drilled from the surface or underground excavations and then multiple hydraulic fracturing treatments are completed (He *et al.* 2016b). These procedures are similar to the one applied in the hydrocarbon industry for unconventional

resources, however, there are some differences for its application to cave mining (Adams and Rowe 2013; Bunger *et al.* 2011):

- The hydraulic fracture size: in cave mining the resultant fracture radius is about 30 m, whereas in shale gas industry the radii of the resultant fractures are in the order of hundreds of metres.
- The fracturing fluid: in cave mining no additives or proppants are used, whereas in the shale gas reservoirs additives and proppants are used during or after the fracturing process. In cave mining 8 to 20 m^3 of water is injected per fracture at a flow rate of about 5 to 10 litres per second, whereas in the shale gas application 135 to 1,000 m^3 of fluid is used per stage at a flow rate of about 75 to 250 litres per second.
- The fracture spacing: in cave mining the spacing is about 1 to 2.5 m, whereas for shale gas production the spacing can be about 100 m.

In addition to traditional uncased borehole hydraulic fracturing, directional hydraulic fracturing can be used. Directional hydraulic fracturing in the mining industry is similar to using perforations through cased boreholes in the hydrocarbon industry. Directional hydraulic fracturing uses a cutting machine to create a notch to provide an initiation point to start the hydraulic fracture. The cutting of this initial notch reduces the required maximum internal pressure to cause fracturing. If the notch is not created perpendicular to the minor principal stress direction, the hydraulic fracture is predicted to initially deviate then realign to this plane. This directional hydraulic fracturing method has been used in coal mining to control rock bursts (Chernov 1982; Fan *et al.* 2012; He *et al.* 2012; Jeffrey 2000; Jeffrey *et al.* 2013; Jeffrey and Mills 2000; Jeffrey *et al.* 2001b; Lekontsev and Sazhin 2014) and enhance top coal caveability (Huang *et al.* 2011; Huang *et al.* 2015). However, there have been limited investigations to understand the mechanism of hydraulic fracture realignment from a notch that is not aligned perpendicular to the minor principal stress direction (He *et al.* 2016b). He *et al.* (2016a) investigated the fracture propagation realignment process from a notched borehole and found that this process is governed by the in-situ stress condition and the rock mass heterogeneity.

The hydraulic fracturing technique is also used to measure the in-situ stress conditions of a rock mass (Haimson and Cornet 2003). The presented calculations for in-situ principal stresses are for vertical boreholes (commonly used for hydraulic fracturing) and for tests producing vertical fractures (both within approximately $\pm 15°$). This requires the vertical stress component to be in a principal stress direction and the minor principal stress to be

horizontal. Therefore, understanding the mechanisms of hydraulic fracturing is important for the measurement of in-situ stress conditions.

Hydraulic fracturing is an important technique in the resource industries. Predicting the internal pressure to cause fracturing and the fracture propagation surfaces due to hydraulic fracturing is of significant importance to these applications. The subsequent sections of the literature review will discuss current theories used to predict these initial conditions of hydraulic fracturing.

1.1.2 General concepts

The overall topic covered by this research is the unstable fracture propagation of a brittle rock material via the hydraulic fracturing process. Unstable fracture propagation in hydraulic fracturing is defined by the uncontrollable and rapid fracturing process after the maximum internal (i.e. breakdown) pressure is reached. This internal pressure is usually plotted against the time of the pressurisation period (see Fig. 2). Hence, the breakdown pressure is an important parameter that affects the hydraulic fracture propagation process.

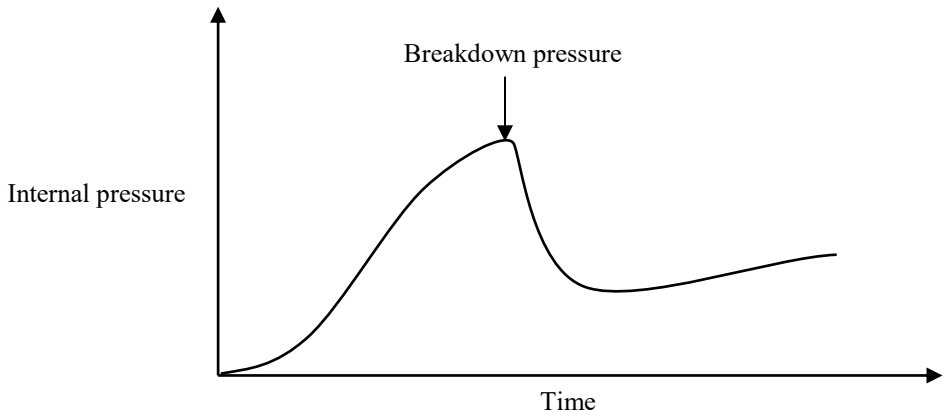

Fig. 2 Conceptual internal pressure versus time graph

Non-planar fracture propagation during the hydraulic fracturing process can occur due to the presence and influence of pre-existing discontinuities in the rock mass. The first influence of these discontinuities can be related to a section of the pressurised borehole, i.e. when there are pre-existing cracks intersecting the borehole. Once the fracture propagates into the rock mass, the discontinuities can further affect the development of the fracture network. The former statement is studied in this research; i.e. the propagation of an arbitrarily orientated crack intersecting a pressurised section of a borehole.

To investigate the breakdown pressures and fracture propagation surfaces from hydraulic fracturing it is important to take into consideration the fact that tectonic forces and

gravity are subjecting rock masses to stress. The general stress state (see Fig. 3) at a local point can always be defined by the principal stresses by rotating the considered coordinates.

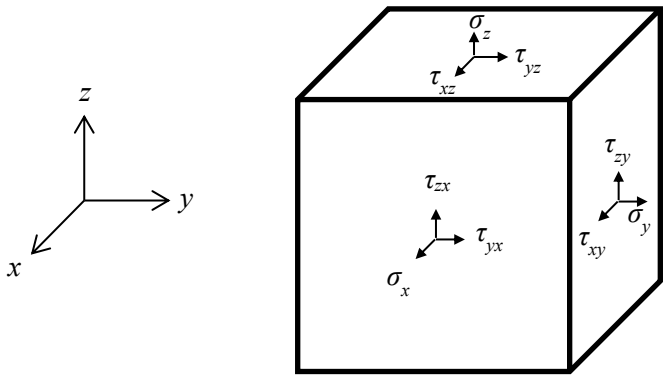

Fig. 3 General state of stress defined using a Cartesian coordinate system (adapted from Young and Budynas 2002)

These principal stresses are defined as the major σ_1, intermediate σ_2, and minor σ_3 principal stresses (where $\sigma_1 \geq \sigma_2 \geq \sigma_3$). Note that in rock mechanics, a positive principal stress value is defined as compressive and hence a negative principal stress value is defined as tensile. This convention is followed in rock mechanics because the in-situ stress conditions are usually compressive. Therefore, the general state of three dimensional stress σ, and its rotated equivalent σ^*, can be expressed by the following stress tensor and principal stress tensor accordingly, as in Eq. (1):

$$\sigma = \begin{bmatrix} \sigma_x & \tau_{xy} & \tau_{zx} \\ \tau_{yx} & \sigma_y & \tau_{yz} \\ \tau_{zx} & \tau_{zy} & \sigma_z \end{bmatrix} \quad \text{or} \quad \sigma^* = \begin{bmatrix} \sigma_1 & 0 & 0 \\ 0 & \sigma_2 & 0 \\ 0 & 0 & \sigma_3 \end{bmatrix} \tag{1}$$

Generally, it is assumed that one of these remote principal stresses in a rock mass is vertical and the other two are horizontal. These are denoted as σ_H and σ_h for the major and minor horizontal principal stresses, respectively, and σ_v for the vertical principal stress. Hence, there are three different compressive stress regimes possible using this assumption; normal $(\sigma_v \geq \sigma_H \geq \sigma_h)$, strike-slip $(\sigma_H \geq \sigma_v \geq \sigma_h)$, and reverse faulting $(\sigma_H \geq \sigma_h \geq \sigma_v)$.

Another important concept used in this research is the resolution of the general stress tensor into normal and shear stresses along an arbitrarily orientated plane. Young and Budynas (2002) present the following expressions in Eq. (2) to calculate the normal

stress σ_n, and the shear stress τ, on an arbitrarily orientated surface, defined by the normal unit vector given by (l,m,n), from the general stress state:

$$\sigma_n = \sigma_x l^2 + \sigma_y m^2 + \sigma_z n^2 + 2\tau_{xy} lm + 2\tau_{yz} mn + 2\tau_{zx} nl$$
$$\tau = \sqrt{\left(\sigma_x l + \tau_{xy} m + \tau_{zx} n\right)^2 + \left(\tau_{xy} l + \sigma_y m + \tau_{yz} n\right)^2 + \left(\tau_{zx} l + \tau_{yz} m + \sigma_z n\right)^2 - \sigma_n{}^2} \quad (2)$$

The following directional cosines, in Eq. (3), define the direction of the shear component:

$$l_\tau = \frac{1}{\tau}\left[\left(\sigma_x - \sigma_n\right) l + \tau_{xy} m + \tau_{zx} n\right]$$
$$m_\tau = \frac{1}{\tau}\left[\tau_{xy} l + \left(\sigma_y - \sigma_n\right) m + \tau_{yz} n\right] \quad (3)$$
$$n_\tau = \frac{1}{\tau}\left[\tau_{zx} l + \tau_{yz} m + \left(\sigma_z - \sigma_n\right) n\right]$$

1.1.3 Breakdown pressure theories for intact rock material

Current breakdown pressure theories for an intact rock are based on the linear elastic stress distribution around a pressurised cylindrical borehole. Considering a borehole with an internal pressure P, orientated along the z axis of the general stress state, the stress domain is disturbed (see Fig. 4 for the definition of the cylindrical stress components).

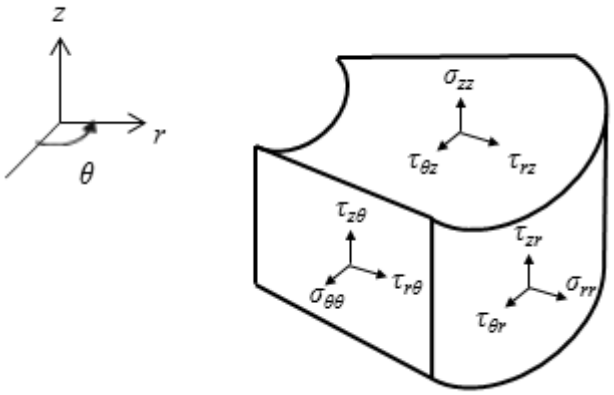

Fig. 4 Cylindrical stress components for an element near a pressurised borehole

Kirsch (1898) solved this stress field, shown in Eq. (4), as a function of radial distance away from the borehole wall r, with radius R, and with θ defined from σ_x (these equations were sourced from Bradley (1979)):

$$
\begin{aligned}
\sigma_{rr} &= \left(\frac{\sigma_x+\sigma_y}{2}\right)\left(1-\frac{R^2}{r^2}\right)+\left(\frac{\sigma_x-\sigma_y}{2}\right)\left(1+\frac{3R^4}{r^4}-\frac{4R^2}{r^2}\right)\cos(2\theta) \\
&+\tau_{xy}\left(1+\frac{3R^4}{r^4}-\frac{4R^2}{r^2}\right)\sin(2\theta)+P\frac{R^2}{r^2} \\
\sigma_{\theta\theta} &= \left(\frac{\sigma_x+\sigma_y}{2}\right)\left(1+\frac{R^2}{r^2}\right)-\left(\frac{\sigma_x-\sigma_y}{2}\right)\left(1+\frac{3R^4}{r^4}\right)\cos(2\theta) \\
&-\tau_{xy}\left(1+\frac{3R^4}{r^4}\right)\sin(2\theta)-P\frac{R^2}{r^2} \\
\sigma_{zz} &= \sigma_z-\upsilon\left[2(\sigma_x-\sigma_y)\frac{R^2}{r^2}\cos(2\theta)+4\tau_{xy}\frac{R^2}{r^2}\sin(2\theta)\right] \\
\tau_{r\theta} &= \left(\frac{\sigma_x-\sigma_y}{2}\right)\left(1-\frac{3R^4}{r^4}+\frac{2R^2}{r^2}\right)\sin(2\theta)+\tau_{xy}\left(1-\frac{3R^4}{r^4}+\frac{2R^2}{r^2}\right)\cos(2\theta) \\
\tau_{\theta z} &= \left[-\tau_{xz}\sin(\theta)+\tau_{yz}\cos(\theta)\right]\left(1+\frac{R^2}{r^2}\right) \\
\tau_{rz} &= \left[\tau_{xz}\cos(\theta)+\tau_{yz}\sin(\theta)\right]\left(1-\frac{R^2}{r^2}\right)
\end{aligned}
\tag{4}
$$

The remote in-situ principal stresses are transformed so that σ_z aligns with the axis of the borehole. Thus, these transformed remote in-situ stresses (σ_x, σ_y, σ_z, τ_{xy}, τ_{xz}, and τ_{yz}) are used in Eq. (4).

Conventionally, the breakdown pressure P_f, is derived from when the tangential stress $\sigma_{\theta\theta}$, on the pressurised borehole wall reaches the tensile strength σ_t (Zoback *et al.* 1977). The borehole axis orientation can be drilled in any direction. Therefore, as expressed in Eq. (4), the borehole orientation with respect to the in-situ stress conditions subsequently determines this tangential stress component $\sigma_{\theta\theta}$. Hence, during pressurisation the breakdown pressure is calculated when the tangential stress $\sigma_{\theta\theta}$, at a point on the pressurised borehole wall defined by angle θ, reaches the tensile strength.

To simplify the analysis in laboratory studies, when using this conventional theory to consider a pressurised borehole, the borehole axis is usually orientated along the major σ_1 or intermediate σ_2 principal stress direction (Ito and Hayashi 1991; Zoback *et al.* 1977). Under these simplified conditions, the principal stress σ_1 or σ_2, i.e. orientated perpendicular to the axis of the borehole, influences this tangential stress. Hence, the

breakdown pressure by this conventional theory, when considering the pore pressure p_0 in the material, is as shown in Eq. (5) according to Zoback *et al.* (1977):

$$P_f = \sigma_t + 3\sigma_h - \sigma_H - p_0 \tag{5}$$

where the tensile strength of the rock is denoted as σ_t. Since the minor principal stress σ_3, is perpendicular to the axis of the borehole, the produced hydraulic fracture should propagate along the axis of the borehole. This is supported by Hubbert and Willis (1957), who revealed that in an intact material subjected to the hydraulic fracturing process, the direction of the resultant fracture is perpendicular to the minor principal stress direction.

This conventional breakdown pressure theory has proven to be problematic (Guo *et al.* 1993; Haimson and Zhao 1991; Ito and Hayashi 1991; Morita *et al.* 1996; Zoback *et al.* 1977). One such problem occurs when back calculating the tensile strength of the material using this breakdown pressure formula. This apparent tensile strength is usually significantly higher than the measured tensile strength of the material (Guo *et al.* 1993; Zoback *et al.* 1977). Also, when Guo *et al.* (1993) compared the breakdown pressure values against the minor principal stress and against the stress component of the conventional theory $(3\sigma_3 - \sigma_{1\text{or}2})$, they revealed that, for their experiments, the coefficient of determination (R^2) was higher for the breakdown pressures versus the minor principal stress than that between the breakdown pressure and the tangential stress via the linear least squares fit. In addition, evidence has been presented that the breakdown pressure is dependent on the radius of the borehole, which is ignored in Eq. (5). Whereby, as the borehole radius increases, the breakdown pressure values decrease (Haimson and Zhao 1991; Ito and Hayashi 1991). Therefore, modifications to the conventional breakdown pressure theory are necessary to provide better predictions, which are closer to the measured breakdown pressure values.

Haimson (1968) derived a breakdown pressure expression, by analysing the stress at the borehole wall using poro-elastic theory:

$$P_f = \frac{\sigma_t + 3\sigma_3 - \sigma_{1\text{or}2} - A\dfrac{1-2\upsilon}{1-\upsilon}p_0}{2 - A\dfrac{1-2\upsilon}{1-\upsilon}} \tag{6}$$

In this expression, υ is the Poisson's ratio and A is a poro-elastic constant, introduced by Biot and Willis (1957). Haimson (1968) argued that the tensile strength, in Eq. (6), is the apparent tensile strength calculated from the hydraulic fracturing experiments and not the tensile strength from the Brazilian disc or direct tensile tests. However, there should

be only one set of values for the tensile strength. Therefore, the tensile strength values from the Brazilian disc or direct tensile tests should be used in this proposed theory. Due to this inconsistency, the breakdown pressure predicted from Eq. (6) is usually lower than the measured values.

Schmitt and Zoback (1989) modified the theory by Haimson (1968) by introducing a different effective stress σ', defied as $\sigma' = \sigma - Bp_0$, where the coefficient B ranges from 0 to 1. This modification produces the following breakdown pressure expression:

$$P_f = \frac{\sigma_t + 3\sigma_3 - \sigma_{1\text{ or }2} - A\dfrac{1-2\upsilon}{1-\upsilon}p_0}{1 + B - A\dfrac{1-2\upsilon}{1-\upsilon}} \tag{7}$$

The coefficient B is back calculated from hydraulic fracturing tests, hence it is suggested that this confounds the issue and cannot provide a genuine prediction theory, since the hydraulic fracturing experiment is used to derive the coefficient B and this is not determined via another experiment. Therefore, the breakdown pressure values are matched by altering the coefficient B.

A genuine prediction theory in this thesis is defined by using fundamental material properties, derived by experiments other than hydraulic fracturing tests. In summary, using this definition, since Haimson (1968) and Schmitt and Zoback (1989) use hydraulic fracturing experiments to derive their material inputs, their proposed expressions are not classified as genuine prediction theories. In addition, it is well known that when using the tensile strength from International Society of Rock Mechanics (ISRM) the conventional theory described above consistently and significantly underestimates the breakdown pressure of rock. Hence, since the conventional theory underestimates the breakdown pressures consistently (by using the definition of a genuine prediction theory proposed in this thesis) a more accurate theory is required.

Ito and Hayashi (1991) introduced a theory stating that, via hydraulic fracturing, initiation of a fracture orientated along the axis of the borehole occurs at a distance into the material. As discussed above, to simplify the calculations, the borehole axis aligns with either the major or the intermediate principal stress. This critical distance a_{Ic}, between the wall of the borehole and the initiation point within the material, is considered a material constant and is calculated as follows:

$$a_{Ic} = \frac{1}{2\pi}\left(\frac{K_{Ic}}{\sigma_t}\right)^2 \tag{8}$$

where the tensile strength is σ_t and the mode I fracture toughness is K_{Ic} (see discussion in Section 1.1.4). The complete stress distribution of the tangential stress is calculated by superimposing the conventional stress field, in this case Eq. (9), and the stress from fluid permeation, i.e., Eq. (10):

$$\sigma_{\theta\theta}^{(1)} = \left(\frac{\sigma_{1or2}+\sigma_3}{2}\right)\left(1+\frac{R^2}{r^2}\right) - \left(\frac{\sigma_{1or2}-\sigma_3}{2}\right)\left(1+\frac{3R^4}{r^4}\right)\cos(2\theta) - P\frac{R^2}{r^2} \tag{9}$$

$$\sigma_{\theta\theta}^{(2)} = A\frac{1-2\upsilon}{1-\upsilon}\left[\frac{1}{r^2}\int_R^r (p-p_0)pdp - (p-p_0)\right] \tag{10}$$

The function p is the pore pressure distribution. Ito and Hayashi (1991) provided this pore pressure distribution for a constant pressurisation rate. Note, the constant pressurisation rate method is not the recommended process for rock stress estimation via hydraulic fracturing (Haimson and Cornet 2003). It is recommended that a constant flow rate be used. The difference between constant pressurisation and constant flow rates is which parameter has been controlled during the fluid pressurisation. Constant pressurisation rate maintains a constant increase in pressure for each time step, whereas constant flow rate maintains a constant increase in flow volume per time step. However, using a constant pressurisation rate, lower and upper bound expressions were derived for the fracture initiation pressure P_i. The upper limit was derived as the following, corresponding to very high pressurisation rates, approaching ∞ MPa per second:

$$P_i = \left(1+\frac{a_{Ic}}{R}\right)^2 \left\{\sigma_t - \left[\begin{array}{l} \dfrac{\sigma_{1or2}+\sigma_3}{2}\left(1+\dfrac{R^2}{(R+a_{Ic})^2}\right) \\ -\dfrac{\sigma_{1or2}-\sigma_3}{2}\left(1+3\dfrac{R^4}{(R+a_{Ic})^4}\right)\end{array}\right]\right\} \tag{11}$$

The lower limit is expressed by the following, associated with very low pressurisation rates, approaching 0 MPa per second:

$$P_i = \frac{\sigma_t - \left[\dfrac{\sigma_{1or2}+\sigma_3}{2}\left(1+\dfrac{R^2}{(R+a_{Ic})^2}\right) - \dfrac{\sigma_{1or2}-\sigma_3}{2}\left(1+3\dfrac{R^4}{(R+a_{Ic})^4}\right)\right]}{\left(1-\dfrac{A}{2}\right)\left\{1+\dfrac{1}{(1+a_{Ic}/R)^2}\right\}} \tag{12}$$

Numerical analysis is required to derive the fracture initiation pressure between these two theoretical constant pressurisation rates.

In summary, the prediction of the breakdown pressures is complex and is dependent on many factors including the borehole radius, external compressive stresses, material

properties and flow rate of fluid injection. In addition, it appears that current theory cannot accurately predict the breakdown pressure for constant flow rate experiments, using material properties sourced solely from non-hydraulic fracturing tests.

1.1.4 Breakdown pressure theories for notched or pre-existing flaws intersecting a pressurised borehole section in rock materials

There are limited hydraulic fracturing experimental studies on analysing the breakdown pressures with notches or pre-existing flaws intersecting a pressurised borehole section in rock materials. Yan *et al.* (2011) provided one such hydraulic fracturing study where they investigated a material with a flaw intersecting the pressurised borehole section. They positioned an A4 piece of paper in the concrete material to simulate a pre-existing crack. There were two experiments conducted with the piece of paper intersecting the pressurised borehole section. One experiment placed the flaw perpendicular to the axis of the borehole and the other placed it parallel to the axis of the borehole. The latter was placed at an angle to the external lateral principal stress directions. They found that the presence of the piece of paper in the material caused a reduction in the breakdown pressure. However, they do not provide any theory to predict the breakdown pressures of these experiments. The number of samples tested in this configuration resulted in a limited understanding regarding the breakdown pressures in a discontinuous material. Zhang and Chen (2010) studied a related problem, where they considered the influence of the injection point in an intact rock. This perforation orientation controls the initial fracture location. Hence, they did not study the breakdown pressure of a discontinuous material; rather they studied the re-orientation of a fracture initiated at an angle to the principal stress directions. Considering there are limited hydraulic fracturing experimental studies into a discontinuous material, the background information in this section is re-focussed to a more fundamental review.

The pre-existing cracks in rocks change the stress distribution in the material. To analyse the elastic stress distribution caused by these pre-existing cracks, the concept of stress intensity factors has been introduced. Consider a spherical coordinate system defined, at a point on the crack front, by the radial r, tangential t, and inclination angle θ, as shown in Fig. 5:

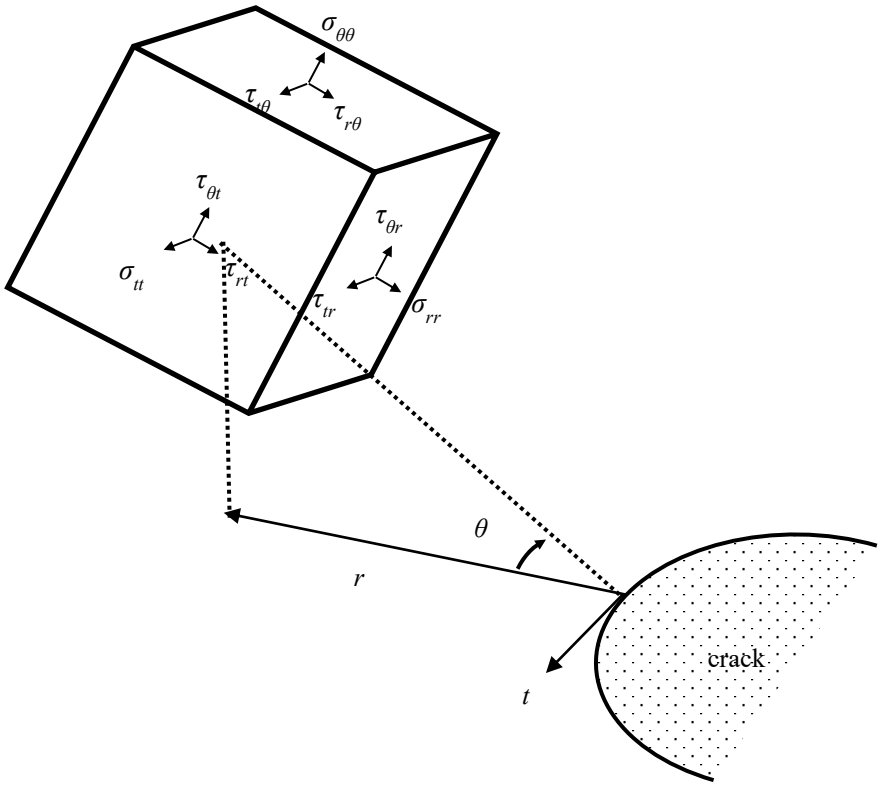

Fig. 5 Stress on an element near the crack front

Theory of elasticity can define the stress distribution near the crack front. Using the theory of elasticity, the magnitudes of the stress components asymptote to infinity, as the position of consideration approaches the crack front. This stress distribution is not realistic; however, stress intensity factors provide a means to quantify the influence of the crack in a material under load. There are three stress intensity factors corresponding to the three modes of fracture (see Fig. 6).

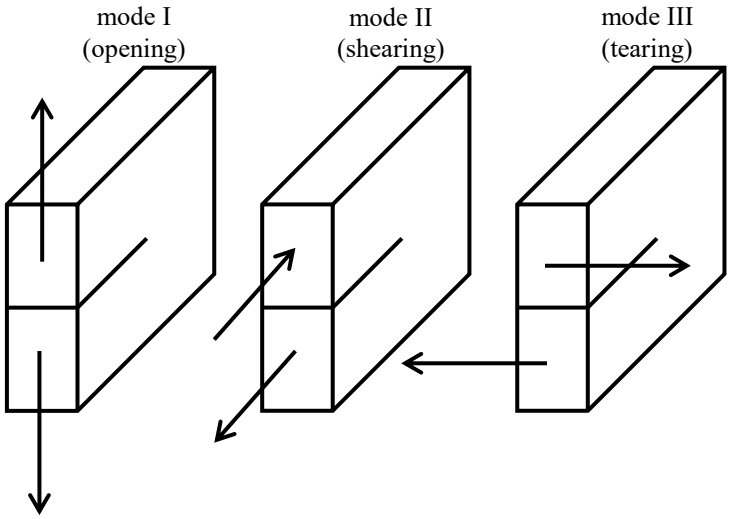

Fig. 6 Modes of fracture

Note, the difference in mode II (shearing) and mode III (tearing) is in the force vector direction. The force vector direction in mode II (shearing) is perpendicular to the front of the crack and is in the same plane as the crack, whereas in mode III (tearing) the force vector is parallel to the front of the crack (and is in the same plane as the crack). Mode II and III are also known as in plane shearing and out of plane tearing.

Stress intensity factors are defined by the following expressions (Rooke and Cartwright 1976):

$$K_I = \lim_{r\to 0} \sigma_{\theta\theta}(r,t,\theta=0)\sqrt{2\pi r}$$
$$K_{II} = \lim_{r\to 0} \tau_{r\theta}(r,t,\theta=0)\sqrt{2\pi r} \quad (13)$$
$$K_{III} = \lim_{r\to 0} \tau_{t\theta}(r,t,\theta=0)\sqrt{2\pi r}$$

In this thesis, the concept of net pressure is used to derive the mode I stress intensity factors around the crack front of a circular (and elliptical) crack. The net pressure is defined as the internal pressure, caused in hydraulic fracturing by fluid pressure, minus the normal compressive stress on the plane of the crack, caused by the in-situ stresses. This therefore considers the summation of normal tensile stress on the surface (or plane) of the crack. The net pressure can be used for stress intensity factor calculations because the internal pressure has more influence on the stress conditions around the crack front the closer the point of consideration is to that edge. This concept of net pressure equates to mode I stress intensity factors, because, by definition, this value is the tangential stress value multiplied by $\sqrt{2\pi r}$ as the point of consideration along the plane of the crack front approaches to the edge of the crack. The internal pressure has the greatest influence on

this tangential stress inside the crack and inside the material, just in front of the crack edge. This concept could be applied to mode II and III, if required; for example, if there were opposing shear or tearing components along the face (or plane) of the crack. However, since water was used as the pressurising fluid in this study, and as such it has low viscosity (or shear strength), the concept of net pressure was not applied to mode II or III. The opposing shear or tearing stress components are negligible compared with the stresses used in this work. Therefore, this concept could be applied to mode II and III with scenarios using high viscosity fluid, where the shear strength of the fluid is not negligible, and/or having low compressive in-situ stress values.

Fracture toughness values (critical stress intensity factors) are used to determine the loading conditions that cause unstable propagation of the crack in the material. Griffith (1921, 1925) introduced this concept of fracture initiation by testing pre-existing cracks in glass. It was revealed that by multiplying the tensile stress at failure by the square root of the half-length of the pre-existing crack produced a constant for the material. Therefore, a crack under mode I loading conditions propagates through the material, when the mode I stress intensity factor K_I, reaches the mode I fracture toughness of the material K_{Ic}, i.e., when $K_I \geq K_{Ic}$. In addition, there have been many mixed mode fracture criteria proposed (Erdogan and Sih 1963; Kaung Jain 1981; Koo and Choy 1991; Shen and Stephansson 1994; Sih 1974; Smith *et al.* 2001). Two of the most prominent theories are the maximum energy release rate criterion and the maximum tangential stress criterion. The maximum energy release rate criterion uses the energy components of mode I, II and III. When the crack is under plane strain conditions (i.e., in the case of an embedded crack) the energy components are as follows:

$$\begin{aligned} G_I &= \left(1-\upsilon^2\right)\frac{K_I{}^2}{E} \\ G_{II} &= \left(1-\upsilon^2\right)\frac{K_{II}{}^2}{E} \\ G_{III} &= \left(1+\upsilon\right)\frac{K_{III}{}^2}{E} \end{aligned} \tag{14}$$

where E is the elastic modulus and υ is the Poisson's ratio. The critical energy components under plane strain can be expressed by the following:

$$\begin{aligned} G_{Ic} &= \left(1-\upsilon^2\right)\frac{K_{Ic}{}^2}{E} \\ G_{IIc} &= \left(1-\upsilon^2\right)\frac{K_{IIc}{}^2}{E} \\ G_{IIIc} &= \left(1+\upsilon\right)\frac{K_{IIIc}{}^2}{E} \end{aligned} \tag{15}$$

Mode I, II and III fracture toughness values are defined as K_{Ic}, K_{IIc}, and K_{IIIc}, respectively. Therefore, normalising the energy components by their associated critical energy components, the following expression is derived:

$$\left(\frac{K_I}{K_{Ic}}\right)^2+\left(\frac{K_{II}}{K_{IIc}}\right)^2+\left(\frac{K_{III}}{K_{IIIc}}\right)^2\geq 1 \tag{16}$$

Eq. (16) illustrates that using the maximum energy release rate criterion each mode has equal weight with respect to its fracture toughness. This above expression physically means that each mode contributes to fracture propagation and the method of relating each mode is in terms of its corresponding energy. The reason for adding these terms in the above equation is to capture under what conditions mixed mode crack growth will occur. Note that to the author's knowledge there is no current method of determining the mode III fracture toughness.

The maximum tangential stress criterion compares the maximum tangential stress component to the mode I fracture toughness. For example, Erdogan and Sih (1963) state that the tangential stress for a straight crack, subjected to plane strain or generalised plane stress conditions is defined by the mode I and II stress intensity factors:

$$\sigma_\theta=\frac{\cos\left(\frac{\theta}{2}\right)}{\sqrt{2\pi r}}\left[K_I\cos^2\left(\frac{\theta}{2}\right)-\frac{3}{2}K_{II}\sin\left(\frac{\theta}{2}\right)\right] \tag{17}$$

Eq. (17) is modified by dividing this expression by $\sqrt{\pi}$ in accordance to the stress intensity factor definition outlined by Rooke and Cartwright (1976), as stated in Eq. (13).

The tangential stress is therefore maximised when the critical angle is the following:

$$\theta_c=\begin{cases}0^\circ & \text{if } K_{II}=0\\ 2\arctan\left[\dfrac{K_I\pm\sqrt{{K_I}^2+8{K_{II}}^2}}{4K_{II}}\right] & \text{if } K_{II}\neq 0\end{cases} \tag{18}$$

Hence, the critical angles produced are evaluated by substituting them into the expression:

$$\sigma_\theta\sqrt{2\pi r}=\cos\left(\frac{\theta}{2}\right)\left[K_I\cos^2\left(\frac{\theta}{2}\right)-\frac{3}{2}K_{II}\sin\left(\frac{\theta}{2}\right)\right] \tag{19}$$

For this configuration, the criterion then becomes the following:

$$\cos\left(\frac{\theta}{2}\right)\left[K_I\cos^2\left(\frac{\theta}{2}\right)-\frac{3}{2}K_{II}\sin\left(\frac{\theta}{2}\right)\right]\geq K_{Ic} \tag{20}$$

To determine the mode I fracture toughness of rock there has been three methods suggested by the International Society for Rock Mechanics (ISRM) using the following types of specimen:

- Cracked chevron notched Brazilian disc (CCNBD) specimens (Fowell 1995)
- Chevron bend specimens (Ouchterlony 1988)
- Short rod specimens (Ouchterlony 1988)

Also, the ISRM has suggested the use of a punch through shear specimen to determine the mode II fracture toughness of rock (Backers and Stephansson 2012).

A new concept implemented in this research is the theory of critical distances. The theory of critical distances is a group of methods that use a characteristic material length parameter, the critical distance a_{Ic}, and linear elastic analysis. The critical distance is related to the fracture process zone and is expressed in Eq. (8) of Section 1.1.3.

This group of methods lies in between the two extremes of linear elastic fracture mechanics (LEFM) and micro-mechanistic approaches. The theory of critical distances is closer to the continuum mechanics end of the spectrum. Predictions by the theory of critical distances are achieved by using elastic stress analysis information only (estimations of the elastic stresses and strains in the material). This analytical approach is unrealistic since there is no introduced yielding or damage causing permanent strains and non-linear stress-strain behaviour (Taylor 2008). However, it has been demonstrated to provide accurate predictions of tensile failure in brittle materials (Taylor 2010).

This theory assumes crack propagation is a discontinuous process occurring in steps of four times the critical distance, rather than continuously and smoothly, as with LEFM theory. This assumption is supported by observations of crack growth in experiments. The crack growth process was shown to be discontinuous in slow cracking at a constant load in bone alloy (Hazenberg *et al.* 2006). In this case, the crack growth rate cycles (with peaks and troughs) the minimum crack growth rate was associated with microstructural boundaries, i.e. Volkmann's canals in the bone. Microstructural barriers (due to grain boundaries and voids) to crack growth may occur in rocks and produce a toughening mechanism, i.e. they can reduce the crack growth rate. This discontinuous crack growth can also occur in materials with no microstructural barriers. For example, this was observed in amorphous polymers such as epoxy resin (Kinloch *et al.* 1983). The mechanism for this discontinuous crack growth in this material was attributed to periodic blunting and sharping of the crack front. Therefore, this assumption of discontinuous crack growth rate in rock, i.e. using the theory of critical distances, can be used to provide accurate predictions of tensile failure (Ito 2008).

The simplest form of the critical distance theory is the point method. This method predicts the failure of the material will occur at a critical distance a_{Ic}, from the crack front r, when the stress at this point is equal to the tensile strength σ_t:

$$\sigma\left(r = a_{Ic}\right) = \sigma_t \tag{21}$$

As another approach, the line method uses the same direction of failure as the point method, but the failure is predicted to occur when the average stress from the crack front to four times the critical distance, reaches the tensile strength:

$$\frac{1}{4a_{Ic}} \int_0^{4a_{Ic}} \sigma\left(r\right) = \sigma_t \tag{22}$$

Additional methods include the area method and the volume method where, using a similar method, they average the elastic stresses near the crack front over a defined shape.

A related analytical technique is the imaginary crack method. For prediction purposes, a crack is inserted into the body at a critical distance a_{Ic}, from the notched region. The LEFM theory is then implemented to predict the influence of this assumed crack on the failure of the material. In other words, when the mode I stress intensity factor of this assumed crack equals the mode I fracture toughness of the material, the maximum stress is reached, i.e., failure occurs.

In summary, there has been limited experimental research regarding the breakdown pressures of a discontinuous material. Hence, a fundamental review was focused on the LEFM theories.

1.1.5 Non-planar hydraulic fracture propagation theories

In hydraulic fracturing, a non-planar fracture propagation surface can occur due to an arbitrarily orientated crack intersecting the pressurised section of a borehole. A planar fracture growth is predicted when the pre-existing crack plane is aligned perpendicular to the remote minor principal stress direction. Since there is a high probability that at least one crack is present near the pressurised section of the borehole, it is important to predict and validate the tortuosity (twisting and turning) of the propagating fracture for an arbitrarily orientated crack.

The main theories to calculate the fracturing direction include the maximum tangential stress criterion, the minimum strain energy density criterion, and the maximum energy density criterion. The latter two criteria assess the elastic energy produced around a crack region, whereas the former uses only the stress distribution around the crack front.

The maximum tangential stress criterion (Erdogan and Sih 1963) predicts the angle of fracturing θ_c, from the local crack front plane using the direction of the maximum circumferential stress, i.e., the direction with maximum $\sigma_{\theta\theta}$. As discussed in Section 1.1.4, for a straight crack subjected to plane strain or plane stress conditions, the tangential stress is maximised when the critical angle is:

$$\theta_c = \begin{cases} 0° & \text{if } K_{II} = 0 \\ 2\arctan\left[\dfrac{K_I \pm \sqrt{{K_I}^2 + 8{K_{II}}^2}}{4K_{II}}\right] & \text{if } K_{II} \neq 0 \end{cases} \tag{23}$$

These critical angles are evaluated by the following expression:

$$\sigma_\theta \sqrt{2\pi r} = \cos\left(\frac{\theta}{2}\right)\left[K_I \cos^2\left(\frac{\theta}{2}\right) - \frac{3}{2} K_{II} \sin\left(\frac{\theta}{2}\right)\right] \tag{24}$$

For configurations that cannot express the stress field analytically, the tangential stress distribution can be assessed numerically.

The minimum strain energy density criterion (Sih 1974) states the crack growth occurs in the direction where the strain energy density factor is the minimum. The strain energy density factor is the elastic energy W, stored in an element with an infinitesimal area A, near the crack front, and with a radial distance r. For example, for a two-dimensional stress system, under plane strain conditions, the local strain energy density field is:

$$\frac{\mathrm{d}W}{\mathrm{d}A} = \frac{1}{r}\left\{\begin{array}{l} \left[\dfrac{1+\upsilon}{8E}\left(\left(1+\cos(\theta)\right)\left(3-4\upsilon-\cos(\theta)\right)\right)\right]{K_I}^2 \\ +\dfrac{1+\upsilon}{2E}\sin(\theta)\left[\cos(\theta)-(1-2\upsilon)\right]K_I K_{II} \\ +\dfrac{1+\upsilon}{8E}\left[(4-4\upsilon)(1-\cos(\theta))+(1+\cos(\theta))(3\cos(\theta)-1)\right]{K_{II}}^2 \end{array}\right\} \tag{25}$$

Therefore, the magnitude of strain energy density is determined, in this case, by $r\dfrac{\mathrm{d}W}{\mathrm{d}A}$ and is called the strain energy density factor. The angle θ, that minimises this strain energy density factor provides the direction of fracture.

On the other hand, to predict the direction of the fracture, the maximum strain energy release rate criterion uses the strain energy change in a linear elastic material ∂W, when the crack grows by one unit of length a. Hence, the energy change per unit length can be approximated by the following expression (Shen and Stephansson 1994):

$$\frac{\partial W}{\partial a} \approx \frac{\left[W(a+\Delta a) - W(a)\right]}{\Delta a} \tag{26}$$

The crack is stated to grow in the angle θ that maximises $\frac{\partial W}{\partial a}$. Since the above expression requires the calculation of the energy of a kinked crack, the calculation of this fracture angle is usually achieved using numerical analysis methods.

The numerical methods, used to predict the final geometry of non-planar cracks, are computationally intensive and therefore are not appropriate for routine design tasks undertaken in industry. Hence, Rahman *et al.* (2000) introduced a two dimensional analytical method to approximate the mixed mode propagation of a pressurised crack, using the maximum tangential stress criterion. This method has not been extended to three dimensions.

Despite the implementation time needed for these numerical methods, these models are used predominantly in the literature to simulate non-planar hydraulic fracture propagation. The most common numerical techniques used in conjunction with these theories are the boundary element method (Crouch 1976; Kuriyama and Mizuta 1993), and finite element method (Kuna 2013). A brief overview of some of the hydraulic fracturing numerical simulations is provided below. However, these hydraulic fracturing models, in general, lack experimental verification of the non-planar fracture propagation.

Lam and Cleary (1987) developed a numerical scheme, coupling the fluid flow and material deformation, and using the finite element method, to model a vertical planar fracture that was perpendicular to the minor principal stress. This model captured the influence of different maximum horizontal stress distributions, and internal pressure gradients within the fracture. However, since this fracture was aligned perpendicular to the minor principal stress direction, the fracture reorientation process was not captured.

An example of the three dimensional fracture reorientation process was simulated by Sousa *et al.* (1993), using a boundary element method, and coupling the internal fluid flow and material deformation of the fracture. This simulation illustrated the realignment of an elliptical crack that was at an inclination of 75° from the final propagation plane (perpendicular to the remote minor principal stress direction). However, experimental validation of this fracture propagation surface was not attempted.

Using a two dimensional displacement discontinuity method (a boundary element method) and the maximum tangential stress criterion, Dong and de Pater (2001) investigated the reorientation process of a pressurised initially straight crack that was slightly offset from the minimum horizontal principal stress direction. By changing the internal pressure of the crack while keeping the maximum and minimum horizontal stresses and material properties constant, it was shown that the higher the internal

pressure the more gradual the reorientation path is. In addition, by changing the maximum horizontal stress while keeping all other parameters constant, it was illustrated that an increase in the maximum horizontal principal stress resulted in a more rapid crack reorientation path. In all these examples, the fracture propagation paths reorientated to be perpendicular to the minimum horizontal stress direction.

Hossain and Rahman (2008) presented hydraulic fracturing simulations of non-planar fracture growth using a boundary element model developed by Carter *et al.* (2000). They investigated the fracture propagation from preferred (orientated to be perpendicular to the minor principal stress direction) and non-preferred crack orientations. This study illustrated the resultant complex fracture geometry from cracks in a non-preferred orientation. However, only several propagation steps were modelled in each example, due to the computationally intensive method used.

Zhang *et al.* (2011) investigated, using the two dimensional displacement discontinuity method, the propagation of an inclined, initially straight crack intersecting the cross-section of a borehole aligned with the remote major or intermediate principal stress direction. This study assumed plane strain conditions (where no strain occurs perpendicular to the plane of investigation), which implies the initial crack has a larger length along the axis of the borehole compared to its radial depth from the borehole wall. The presented model coupled the viscous fluid flow and material deformation. The resultant non-uniform pressure distribution along the fracture due to the fluid with high viscosity caused the propagation path to reorientate more gradually to be perpendicular to the minor principal stress direction. However, the assumption of the uniform internal pressure is valid for fluids with low viscosity (such as water).

Huang *et al.* (2012) developed a virtual multidimensional internal bond model to simulate a three dimensional fracture propagation. The material solid was considered as a set of bonded randomised micro particles. Since the model relied on this constitutive relationship, fracture propagation theory was not required. There were four hydraulic fracturing examples with non-planar fracture growth; for case one angle of inclination (from horizontal) was set to 45°, and for the other three cases was set to 30°. The external horizontal compressive principal stresses were set at 0.8 MPa for each of the scenarios. Case one to four had the vertical compressive principal stress values of 0.8 MPa, 1.6 MPa, 2.0 MPa, and 2.4 MPa, respectively. Case one to four had the internal fluid pressure set at 1.6 MPa, 2.4 MPa, 2.8 MPa, and 3.2 MPa, respectively. Even with this increased internal pressure, they illustrated that increasing the vertical compressive principal stress (from hydrostatic conditions) resulted in the fracture surface realigning more rapidly in the vertical direction (perpendicular to the minor principal stress

direction). Hence, in these numerical models, the larger the difference in compressive principal stresses, the shorter the reorientation process. Segmentation of the fracture front was observed for the highest vertical remote compressive stress, however, there is a lack of experimental data to validate this segmentation process.

To simulate the propagation of the non-planar hydraulic fractures, Gupta and Duarte (2014) implemented an extended finite element method (XFEM). A fracture propagation simulation of an initially elliptical planar crack was presented. The result illustrates the complex three dimensional geometry produced when considering non-uniform remote lateral principal stress distributions.

Cherny *et al.* (2016) provided simulations of a non-planar hydraulic fracture growth using a three dimensional boundary element method. They illustrate the variability of such a model in predicting the non-planar hydraulic fracturing process.

The numerical modelling based research studies discussed above demonstrate the importance of developing experimental verification examples of non-planar hydraulic fracture propagation. In addition, developing a three dimensional analytical method to predict efficiently the non-planar hydraulic fracture propagation is advantageous since current numerical methods are computationally intensive.

1.1.6 Conclusions

Hydraulic fracturing is a key method utilised by the resource industries. Estimating the fracture network produced from hydraulic fracturing is crucial to target effective zones to increase permeability and fragmentation. Hence, predicting the breakdown pressures and fracture propagation surfaces of intact and notched rock materials from hydraulic fracturing treatments are important parameters to assist in determining the resultant fracture networks. Therefore, from the literature review above, there is a need for producing experimentally derived fracture propagation surfaces from notched specimens to assist with the development of fracture propagation algorithms. In addition, it is beneficial to derive fracture propagation algorithms that approximate these surfaces quickly for use in industry. In order to model the fracture propagation surfaces from notched rock material the breakdown pressure must be predicted. In addition, to assist in predicting the resultant fracture network produced from hydraulic fracturing the breakdown pressure from intact rock material must also be accurately predetermined. These research tasks will help with understanding which zones to target for effective hydraulic fracturing stimulations.

1.2 Addressed gaps in knowledge

The following gaps in knowledge are addressed in this work:

- An efficient analytical method to assess the three dimensional propagation of a pressurised, initially circular (or elliptical) fracture surface in an ideally brittle rock material subjected to unequal remote compressive principal stresses. This analytical approach should be validated using available three dimensional numerical methods. The final fracture geometry for these arbitrarily orientated cracks should realign to become perpendicular to the minor principal stress direction.
- To predict accurately the breakdown pressure for an intact rock material based on minimal material properties using an analytical approach. To claim that this approach is predictive, these material properties must not be obtained from hydraulic fracturing experiments, rather solely obtained using conventional International Society of Rock Mechanics (ISRM) suggested methods. In addition, this approach must be able to predict the breakdown pressures from a vertically aligned pressurised borehole in a material subjected to reverse faulting conditions (i.e., where the remote vertical principal stress is the minor principal stress component).
- A comprehensive experimental data set to provide verification examples of the breakdown pressures and the resultant non-planar hydraulic fracture propagation surfaces. These experiments, using pre-existing initially inclined notches in a brittle material, should also investigate the shear stress magnitude influence on the breakdown pressures and the generated fracture propagation surfaces. The digitised fracture propagation surfaces should be compared to the three dimensional models.

1.3 General problem statements

The general problem statements investigated are as follows:

- Prediction of the fracture propagation surface from an arbitrarily orientated circular pressurised crack in a brittle rock material, subjected to different remote loading conditions.
- Prediction of the maximum injection (breakdown) pressure of a circular crack intersecting a borehole section in a brittle rock material, subjected to remote triaxial compressive stress conditions.

- Prediction of the maximum injection (breakdown) pressure of a pressurised borehole section aligned with one remote principal stress direction axes, in an intact brittle rock material.

1.4 Contributions to knowledge and outline

In paper 1, a three dimensional analytical method is proposed to approximate the mixed mode propagation for a pressurised circular crack. The approximation is validated against the numerical results. In addition, the fracture propagation surfaces align with the published two dimensional analytical models. This method provides a reason for the fracture propagation surface to realign perpendicular to the remote minor principal stress direction.

In paper 2, a new fracture mechanics approach is suggested to predict the breakdown pressures of an intact brittle rock material. The results from this approach align well with the experimental results of the current study and previous published research. Specifically, the actual and predicted breakdown pressure distributions (based on the measured material properties) agree very well. This approach suggests that the high breakdown pressures may be caused by an equivalent stable crack being produced during hydraulic fracturing.

Paper 3 experimentally investigates the breakdown pressures and propagation surfaces from pressurised circular notches. The test results illustrate that the fracture propagation surfaces realign more rapidly in the direction perpendicular to the minor principal stress when the surface of the circular crack has a greater resultant shear stress magnitude. The observed fracture propagation surfaces align with the numerical models. In addition, under the shear stress conditions tested, the shear stress magnitude had no perceivable influence on the breakdown pressure values recorded. These observed fracture propagation surfaces and measured breakdown pressures will provide a comprehensive dataset for the verification of the analytical or numerical models in the future.

References

Adachi, J, Siebrits, E, Peirce, A and Desroches, J 2007, 'Computer simulation of hydraulic fractures', *International Journal of Rock Mechanics and Mining Sciences*, vol. 44, no. 5, pp. 739-757.

Adams, J and Rowe, C 2013, 'Differentiating applications of hydraulic fracturing'.

Allis, R 1982, 'Mechanism of induced seismicity at The Geysers geothermal reservoir, California', *Geophysical Research Letters*, vol. 9, no. 6, pp. 629-632.

Araneda, O, Morales, R, Henriquez, J, Rojas, E and Molina, R 2007, 'Rock preconditioning application in virgin caving condition in a panel caving mine, Codelco Chile El Teniente Division', *Proceedings Deep and High Stress Mining, Australian Centre for Geomechanics, Perth, Australia*, pp. 111-120.

Backers, T and Stephansson, O 2012, 'ISRM suggested method for the determination of mode II fracture toughness', *Rock Mechanics and Rock Engineering*, pp. 1-12.

Bartko, K, Nasr-El-Din, H, Rahim, Z and Al-Muntasheri, G 2003, 'Acid fracturing of a gas carbonate reservoir: the impact of acid type and lithology on fracture half length and width', *SPE Annual Technical Conference and Exhibition*.

Batra, R, Albright, JN and Bradley, C 1984, *Downhole seismic monitoring of an acid treatment in the Beowawe Geothermal Field*, Los Alamos National Lab., NM (USA).

Beauce, A, Fabriol, H, Le Masne, D, Cavoit, C, Mechler, P and CHEN, XK 1991, 'Seismic studies on the HDR site of Soultz-sous-Forets (Alsace, France)', *Geothermal science and technology*, vol. 3, no. 1-4, pp. 239-266.

Biot, M and Willis, D 1957, 'The Theory of Consolidation', *J. Appl Elastic Coefficients of the Mech*, vol. 24, pp. 594-601.

Bradley, WB 1979, 'Failure of Inclined Boreholes', *Journal of Energy Resources Technology*, vol. 101, no. 4, pp. 232-239.

Bunger, AP, Jeffrey, RG, Kear, J, Zhang, X and Morgan, M 2011, 'Experimental investigation of the interaction among closely spaced hydraulic fractures'.

Caineng, Z, Guangya, Z, Shizhen, T, Suyun, H, Xiaodi, L, Jianzhong, L, Dazhong, D, Rukai, Z, Xuanjun, Y, Lianhua, H, Hui, Q, Xia, Z, Jinhua, J, Xiaohui, G, Qiulin, G, Lan, W and Xinjing, L 2010, 'Geological features, major discoveries and unconventional petroleum geology in the global petroleum exploration', *Petroleum Exploration and Development*, vol. 37, no. 2, pp. 129-145.

Carter, B, Desroches, J, Ingraffea, A and Wawrzynek, P 2000, 'Simulating fully 3D hydraulic fracturing', *Modeling in Geomechanics*, pp. 525-557.

Catalan, A, Dunstan, G, Morgan, M, Green, S, Jorquera, M, Thornhill, T, Onederra, I and Chitombo, G 2012, 'How can an intensive preconditioning concept be implemented at mass mining method? Application to Cadia East panel caving project'.

Charlez, P, Lemonnier, P, Ruffet, C, Boutéca, M and Tan, C 1996, 'Thermally induced fracturing: analysis of a field case in North Sea', *European Petroleum Conference*.

Chernov, OI 1982, 'Hydrodynamic stratification of petrologically uniform strong rocks as a means of controlling intransigent roofs', *Soviet Mining*, vol. 18, no. 2, pp. 102-107.

Cherny, S, Lapin, V, Esipov, D, Kuranakov, D, Avdyushenko, A, Lyutov, A and Karnakov, P 2016, 'Simulating fully 3D non-planar evolution of hydraulic fractures', *International Journal of Fracture*, pp. 1-31.

Crouch, SL 1976, 'Solution of plane elasticity problems by the displacement discontinuity method. I. Infinite body solution', *International Journal for Numerical Methods in Engineering*, vol. 10, no. 2, pp. 301-343.

Dong, CY and de Pater, CJ 2001, 'Numerical implementation of displacement discontinuity method and its application in hydraulic fracturing', *Computer Methods in Applied Mechanics and Engineering*, vol. 191, no. 8–10, pp. 745-760.

Erdogan, F and Sih, GC 1963, 'On the crack extension in plates under plane loading and transverse Shear', *Journal of Basic Engineering*, vol. 85, no. 4, pp. 519-525.

Fan, J, Dou, L, He, H, Du, T, Zhang, S, Gui, B and Sun, X 2012, 'Directional hydraulic fracturing to control hard-roof rockburst in coal mines', *International Journal of Mining Science and Technology*, vol. 22, no. 2, pp. 177-181.

Fehler, MC 1989, 'Stress control of seismicity patterns observed during hydraulic fracturing experiments at the Fenton Hill Hot Dry Rock geothermal energy site, New Mexico', *International Journal of Rock Mechanics and Mining Sciences & Geomechanics Abstracts,* vol. 26, pp. 211-219.

Fjær, E, Holt, RM, Horsrud, P, Raaen, AM and Risnes, R 2008, 'Chapter 11 Mechanics of hydraulic fracturing', in RMHPHAMR E. Fjær and R Risnes (eds), *Developments in Petroleum Science*, vol. Volume 53, Elsevier, pp. 369-390.

Fowell, RJ 1995, 'Suggested method for determining mode I fracture toughness using cracked chevron notched Brazilian disc (CCNBD) specimens', *International Journal of Rock Mechanics and Mining Sciences & Geomechanics Abstracts,* vol. 32, pp. 57-64.

Frash, LP, Gutierrez, M and Hampton, J 2014, 'True-triaxial apparatus for simulation of hydraulically fractured multi-borehole hot dry rock reservoirs', *International Journal of Rock Mechanics and Mining Sciences*, vol. 70, no. 0, pp. 496-506.

Fridleifsson, IB and Freeston, DH 1994, 'Geothermal energy research and development', *Geothermics*, vol. 23, no. 2, pp. 175-214.

Ghassemi, A 2012, 'A review of some rock mechanics issues in geothermal reservoir development', *Geotechnical and Geological Engineering*, vol. 30, no. 3, pp. 647-664.

Griffith, A 1921, 'The phenomena of rupture and flow in solids', *Philosophical Transactions*, no. A221, pp. 163-198.

Griffith, A 1925, 'Theory of rupture', paper presented at First International Congress for Applied Mechanics, Delft, South Holland, Netherlands.

Guo, F, Morgenstern, NR and Scott, JD 1993, 'An experimental investigation into hydraulic fracture propagation—Part 2. Single well tests', *International Journal of Rock Mechanics and Mining Sciences & Geomechanics Abstracts*, vol. 30, no. 3, pp. 189-202.

Gupta, P and Duarte, C 2014, 'Simulation of non-planar three-dimensional hydraulic fracture propagation', *International Journal for Numerical and Analytical Methods in Geomechanics*.

Haimson, BC 1968, 'Hydraulic fracturing in porous and nonporous rock and its potential for determining in-situ stresses at great depth', University of Minnesota.

Haimson, BC and Cornet, F 2003, 'ISRM suggested methods for rock stress estimation—part 3: hydraulic fracturing (HF) and/or hydraulic testing of pre-existing fractures (HTPF)', *International Journal of Rock Mechanics and Mining Sciences*, vol. 40, no. 7, pp. 1011-1020.

Haimson, BC and Zhao, Z 1991, 'Effect of borehole size and pressurization rate on hydraulic fracturing breakdown pressure'.

Hardin, F, Barry, M, Shuchart, C, Gdanski, R, Ritter, D and Huynh, D 2003, 'Sandstone acidizing treatment of a horizontal openhole completion using coiled tubing from a deepwater floating production platform', *SPE Annual Technical Conference and Exhibition*.

Häring, MO, Schanz, U, Ladner, F and Dyer, BC 2008, 'Characterisation of the Basel 1 enhanced geothermal system', *Geothermics*, vol. 37, no. 5, pp. 469-495.

Hazenberg, JG, Taylor, D and Clive Lee, T 2006, 'Mechanisms of short crack growth at constant stress in bone', *Biomaterials*, vol. 27, no. 9, pp. 2114-2122.

He, H, Dou, L, Fan, J, Du, T and Sun, X 2012, 'Deep-hole directional fracturing of thick hard roof for rockburst prevention', *Tunnelling and Underground Space Technology*, vol. 32, pp. 34-43.

He, Q, Suorineni, F and Oh, J 2016a, 'Modeling directional hydraulic fractures in heterogeneous rock masses', *MassMin, Sydney*.

He, Q, Suorineni, FT and Oh, J 2016b, 'Review of hydraulic fracturing for preconditioning in cave mining', *Rock Mechanics and Rock Engineering*, vol. 49, no. 12, pp. 4893-4910.

Holditch, SA and Madani, H 2010, 'Global Unconventional Gas-It is There, But is it Profitable?', *Journal of Petroleum Technology*, vol. 62, no. 12, pp. 42-48.

Hossain, MM and Rahman, MK 2008, 'Numerical simulation of complex fracture growth during tight reservoir stimulation by hydraulic fracturing', *Journal of Petroleum Science and Engineering*, vol. 60, no. 2, pp. 86-104.

Huang, B, Liu, C, Fu, J and Guan, H 2011, 'Hydraulic fracturing after water pressure control blasting for increased fracturing', *International Journal of Rock Mechanics and Mining Sciences*, vol. 48, no. 6, pp. 976-983.

Huang, B, Wang, Y and Cao, S 2015, 'Cavability control by hydraulic fracturing for top coal caving in hard thick coal seams', *International Journal of Rock Mechanics and Mining Sciences*, vol. 74, pp. 45-57.

Huang, K, Zhang, Z and Ghassemi, A 2012, 'Modeling three-dimensional hydraulic fracture propagation using virtual multidimensional internal bonds', *International Journal for Numerical and Analytical Methods in Geomechanics*, vol. 37, pp. 2021-2038.

Hubbert, MK and Willis, DG 1957, 'Mechanics of hydraulic fracturing', *Journal of American Association of Petroleum Geologists*, vol. 18, no. 12.

Ito, T 2008, 'Effect of pore pressure gradient on fracture initiation in fluid saturated porous media: Rock', *Engineering Fracture Mechanics*, vol. 75, no. 7, pp. 1753-1762.

Ito, T and Hayashi, K 1991, 'Physical background to the breakdown pressure in hydraulic fracturing tectonic stress measurements', *International Journal of Rock Mechanics and Mining Sciences & Geomechanics Abstracts*, vol. 28, no. 4, pp. 285-293.

Jeffrey, R, Zhang, X, Settari, A, Mills, K and Detournay, E 2001a, 'Hydraulic fracturing to induce caving: fracture model development and comparison to field data', *DC Rocks 2001, The 38th US Symposium on Rock Mechanics (USRMS)*.

Jeffrey, RG 2000, *Hydraulic fracturing of ore bodies*, Google Patents.

Jeffrey, RG, Chen, Z, Mills, KW and Pegg, S 2013, 'Monitoring and measuring hydraulic fracturing growth during preconditioning of a roof rock over a coal longwall panel'.

Jeffrey, RG and Mills, KW 2000, 'Hydraulic fracturing applied to inducing longwall coal mine goaf falls'.

Jeffrey, RG, Zhang, X, Settari, A, Mills, KW and Detournay, E 2001b, 'Hydraulic fracturing to induce caving: fracture model development and comparison to field data'.

Kaung Jain, C 1981, 'On the maximum strain criterion—a new approach to the angled crack problem', *Engineering Fracture Mechanics*, vol. 14, no. 1, pp. 107-124.

Kinloch, AJ, Shaw, SJ, Tod, DA and Hunston, DL 1983, 'Deformation and fracture behaviour of a rubber-toughened epoxy: 1. Microstructure and fracture studies', *Polymer*, vol. 24, no. 10, pp. 1341-1354.

Kirsch, G 1898, 'Theory of elasticity and application in strength of materials', *Zeitchrift Vevein Deutscher Ingenieure*, vol. 42, no. 29, pp. 797-807.

Koo, JM and Choy, YS 1991, 'A new mixed mode fracture criterion: maximum tangential strain energy density criterion', *Engineering Fracture Mechanics*, vol. 39, no. 3, pp. 443-449.

Kuna, M 2013, 'Finite Elements in Fracture Mechanics'.

Kuriyama, K and Mizuta, Y 1993, 'Three-dimensional elastic analysis by the displacement discontinuity method with boundary division into triangular leaf elements', *International Journal of Rock Mechanics and Mining Sciences & Geomechanics Abstracts,* vol. 30, pp. 111-123.

Lam, KY and Cleary, MP 1987, 'Three-dimensional analysis of hydraulic fracturing', *Computers and Geotechnics*, vol. 3, no. 4, pp. 213-228.

Lekontsev, YM and Sazhin, PV 2014, 'Directional hydraulic fracturing in difficult caving roof control and coal degassing', *Journal of Mining Science*, vol. 50, no. 5, pp. 914-917.

Majer, EL, Baria, R, Stark, M, Oates, S, Bommer, J, Smith, B and Asanuma, H 2007, 'Induced seismicity associated with Enhanced Geothermal Systems', *Geothermics*, vol. 36, no. 3, pp. 185-222.

Morita, N, Black, A and Fuh, G-F 1996, 'Borehole breakdown pressure with drilling fluids—I. Empirical results', *International Journal of Rock Mechanics and Mining Sciences,* vol. 33, pp. 39-51.

Nami, P, Schellschmidt, R, Schindler, M and Tischner, T 2008, 'Chemical stimulation operations for reservoir development of the deep crystalline HDR/EGS system at Soultz-sous-Forêts (France)', *Proceedings, 32rd Workshop on Geothermal Reservoir Engineering*.

Ouchterlony, F 1988, 'Suggested methods for determining the fracture toughness of rock', *International Journal of Rock Mechanics and Mining Sciences*, vol. 25, no. 2, pp. 71-96.

Puri, R, King, GE and Palmer, ID 1991a, 'Damage to coal permeability during hydraulic fracturing'.

Puri, R, Yee, D, Buxton, TS and Majahan, O 1991b, *Method of increasing the permeability of a coal seam*, Google Patents.

Rae, P and di Lullo, G 2003, 'Matrix Acid Stimulation-A Review of the State-Of-The-Art', *SPE European Formation Damage Conference*.

Rahman, MK, Hossain, MM and Rahman, SS 2000, 'An analytical method for mixed-mode propagation of pressurized fractures in remotely compressed rocks', *International Journal of Fracture*, vol. 103, no. 3, pp. 243-258.

Rogner, H-H 1997, 'An assessment of world hydrocarbon resources', *Annual Review of Energy and the Environment*, vol. 22, pp. 217-262.

Rooke, DP and Cartwright, DJ 1976, *Compendium of stress intensity factors*, Procurement Executive, Ministry of Defence. H. M. S. O. 1976, 330.

Schmitt, DR and Zoback, MD 1989, 'Poroelastic effects in the determination of the maximum horizontal principal stress in hydraulic fracturing tests—a proposed breakdown equation employing a modified effective stress relation for tensile failure', *International Journal of Rock Mechanics and Mining Sciences & Geomechanics Abstracts,* vol. 26, pp. 499-506.

Sharma, M, Gadde, P, Richard, S, Richard, S, Robin, F, David, C, Larry, G and Leen, W 2004, 'Slick water and hybrid fracs in the Bossier: Some lessons learnt', *SPE Annual Technical Conference and Exhibition*.

Shen, B and Stephansson, O 1994, 'Modification of the G-criterion for crack propagation subjected to compression', *Engineering Fracture Mechanics*, vol. 47, no. 2, pp. 177-189.

Sih, GC 1974, 'Strain-energy-density factor applied to mixed mode crack problems', *International Journal of Fracture*, vol. 10, no. 3, pp. 305-321.

Smith, DJ, Ayatollahi, MR and Pavier, MJ 2001, 'The role of T-stress in brittle fracture for linear elastic materials under mixed-mode loading', *Fatigue & Fracture of Engineering Materials & Structures*, vol. 24, no. 2, pp. 137-150.

Smith, MC 1973, *Geothermal energy*, Los Alamos Scientific Lab., N. Mex.(USA).

Solberg, P, Lockner, D and Byerlee, JD 1980, 'Hydraulic fracturing in granite under geothermal conditions', *International Journal of Rock Mechanics and Mining Sciences*, vol. 17, no. 1, pp. 25-33.

Sousa, JL, Carter, BJ and Ingraffea, AR 1993, 'Numerical simulation of 3D hydraulic fracture using Newtonian and power-law fluids', *International Journal of Rock Mechanics and Mining Sciences & Geomechanics Abstracts*, vol. 30, no. 7, pp. 1265-1271.

Taylor, D 2008, 'The theory of critical distances', *Engineering Fracture Mechanics*, vol. 75, no. 7, pp. 1696-1705.

Taylor, D 2010, *The theory of critical distances: a new perspective in fracture mechanics*, Elsevier.

van As, A, Jeffrey, R, Chacon, E and Barrera, V 2004, 'Preconditioning by hydraulic fracturing for block caving in a moderately stressed naturally fractured orebody', *Proceedings of MassMin 2004*, pp. 535-541.

van As, A and Jeffrey, RG 2000, 'Caving induced by hydraulic fracturing at Northparkes mines'.

Vengosh, A, Jackson, RB, Warner, N, Darrah, TH and Kondash, A 2014, 'A critical review of the risks to water resources from unconventional shale gas development and hydraulic fracturing in the United States', *Environmental science & technology*, vol. 48, no. 15, pp. 8334-8348.

Wright, CA, Tanigawa, JJ, Shixin, M and Li, Z 1995, 'Enhanced hydraulic fracture technology for a coal seam reservoir in Central China'.

Yan, T, Li, W and Bi, X 2011, 'An experimental study of fracture initiation mechanisms during hydraulic fracturing', *Petroleum Science*, vol. 8, no. 1, pp. 87-92.

Young, WC and Budynas, RG 2002, *Roark's formulas for stress and strain*, vol. 7, McGraw-Hill New York.

Zhai, C, Li, M, Sun, C, Zhang, J, Yang, W and Li, Q 2012, 'Guiding-controlling technology of coal seam hydraulic fracturing fractures extension', *International Journal of Mining Science and Technology*, vol. 22, no. 6, pp. 831-836.

Zhang, GQ and Chen, M 2010, 'Dynamic fracture propagation in hydraulic re-fracturing', *Journal of Petroleum Science and Engineering*, vol. 70, no. 3–4, pp. 266-272.

Zhang, X, Jeffrey, RG, Bunger, AP and Thiercelin, M 2011, 'Initiation and growth of a hydraulic fracture from a circular wellbore', *International Journal of Rock Mechanics and Mining Sciences*, vol. 48, no. 6, pp. 984-995.

Zoback, MD, Rummel, F, Jung, R and Raleigh, CB 1977, 'Laboratory hydraulic fracturing experiments in intact and pre-fractured rock', *International Journal of Rock Mechanics and Mining Sciences*, vol. 14, no. 2, pp. 49-58.

Paper 1

Statement of Authorship

Title of Paper	Approximation of mixed mode propagation for an internally pressurised circular crack
Publication Status	☑ Published ☐ Accepted for Publication ☐ Submitted for Publication ☐ Unpublished and Unsubmitted w ork w ritten in manuscript style
Publication Details	

Principal Author

Name of Principal Author (Candidate)	Adam Karl Schwartzkopff
Contribution to the Paper	Developed theory and code, wrote manuscript and acted as corresponding author.
Overall percentage (%)	90%
Certification:	This paper reports on original research I conducted during the period of my Higher Degree by Research candidature and is not subject to any obligations or contractual agreements with a third party that would constrain its inclusion in this thesis. I am the primary author of this paper.
Signature	Date Friday 19 August 2016

Co-Author Contributions

By signing the Statement of Authorship, each author certifies that:

i. the candidate's stated contribution to the publication is accurate (as detailed above);
ii. permission is granted for the candidate in include the publication in the thesis; and
iii. the sum of all co-author contributions is equal to 100% less the candidate's stated contribution.

Name of Co-Author	Chaoshui Xu
Contribution to the Paper	Supervised development of work and reviewed manuscript.
Signature	Date Friday 19 August 2016

Name of Co-Author	Nouné Sophie Melkoumian
Contribution to the Paper	Supervised development of work and reviewed manuscript.
Signature	Date Friday 19 August 2016

Approximation of mixed mode propagation for an internally pressurised circular crack

Adam K. Schwartzkopff [a]
Chaoshui Xu [a]
Nouné S. Melkoumian [a]

[a]School of Civil, Environmental and Mining Engineering, Faculty of Engineering, Computer and Mathematical Sciences, The University of Adelaide, SA 5005 Australia

Abstract

Hydraulic fracturing of rocks has various engineering applications. However, there has been limited research into crack propagation prediction by three dimensional analytical techniques. This paper discusses such a technique for predicting the propagation surface of a pressurised circular crack subjected to various loading conditions. The propagation surfaces predicted from the proposed crack front propagation algorithm align well with published results. The suggested method consumes only a fraction of the time needed for a numerical simulation, and therefore it could be useful in assisting the design of hydraulic fracturing operations.

Keywords: fracture mechanics, crack propagation, stress intensity factors, hydraulic fracturing

Nomenclature

a	radius or major axis of the elliptical crack (m)
a_{median}	median crack increment input for FRANC3D (m)
b	minor axis of the elliptical crack (m)
inc	predefined incremental length for the proposed analytical method (m)
$inc_{FRANC3D}(\varphi)$	incremental length used in FRANC3D (m)
$K_{I(median)}$	median stress intensity factor for mode I along the crack front (Pa$\sqrt{\text{m}}$)
$K_I(\varphi)$	stress intensity factor for mode I (Pa$\sqrt{\text{m}}$)
$K_{II}(\varphi)$	stress intensity factor for mode II (Pa$\sqrt{\text{m}}$)
$K_{III}(\varphi)$	stress intensity factor for mode III (Pa$\sqrt{\text{m}}$)
$K_{I(kinked)}(\varphi)$	kinked crack analytical stress intensity factor for mode I (Pa$\sqrt{\text{m}}$)
$K_{II(kinked)}(\varphi)$	kinked crack analytical stress intensity factor for mode II (Pa$\sqrt{\text{m}}$)
$K_{III(kinked)}(\varphi)$	kinked crack analytical stress intensity factor for mode III (Pa$\sqrt{\text{m}}$)
n	power input for calculating the incremental length in FRANC3D
α	dip direction (°)
β	dip angle (°)
γ	ellipse angle – the direction from the projected dip direction on the crack plane to the major axis of the ellipse (°)
θ	crack front angle – from the normal to the crack front towards the positive z axis direction (°)
$\theta_c(\varphi)$	critical crack front angle (°)
$\theta_{kink}(\varphi)$	difference from the radial vector of the current fictitious plane to the kinked radial line (°)
υ	Poisson's ratio
$\sigma_{n(eff)}$	effective normal stress on the surface of the crack (Pa)
$\sigma_{n(external)}$	normal stress on the surface of the crack (Pa)
σ_t	tensile strength (Pa)
τ	shear stress along the surface of the crack (Pa)

τ_{eff}	effective shear stress along the surface of the crack (Pa)
φ	crack front angle – from the x axis direction clockwise around the normal vector in the positive z axis direction (°)
ω	shear angle – clockwise around the normal vector in the positive z axis direction (°)
$B = \left(k^2 - \upsilon\right)E(k) + \upsilon k'^2 K(k)$	constant used to calculate the elliptical crack stress intensity factors
$C = \left(k^2 + \upsilon k'^2\right)E(k) - \upsilon k'^2 K(k)$	constant used to calculate the elliptical crack stress intensity factors
$E(k) = \int_0^{\pi/2} \sqrt{1 - k^2 \sin^2(\alpha)}\, d\alpha$	elliptical integral of the second kind
$k = \sqrt{1 - \left(\frac{b}{a}\right)^2}$	intermediate eccentricity parameter used to calculate the elliptical crack stress intensity factors
$k' = \frac{b}{a}$	ratio of the minor to the major axis of the elliptical crack
$K(k) = \int_0^{\pi/2} \frac{d\alpha}{\sqrt{1 - k^2 \sin^2(\alpha)}}$	elliptical integral of the first kind
LEFM	linear elastic fracture mechanics

1 Introduction

It is important to predict the propagation paths of pressurised cracks in hydraulic fracturing operations in order to design and optimise the extraction of resources, such as geothermal energy and unconventional oil and gas. Hydraulic fracturing is the primary and most effective method used to increase productivity in these applications [1, 2] as it can enhance the rock mass permeability significantly via the resultant fractures.

In an industrial setting, a method is needed for the quick initial assessment of the resultant fracture propagation surface according to the local stress conditions [3]. Establishing such an analytical method has clear advantages including ease of implementation and quick processing times. Numerical methods to address the problem exist [4], however, most of them have been limited to two dimensional [5, 6] or highly intensive computational methods [7]. The numerical method proposed by Huang *et al.* [4] aims to solve a similar problem addressed by this paper. Their numerical method uses a virtual multidimensional internal bond model that is implemented in a three dimensional finite element code.

Rahman *et al.* [3] developed a two dimensional analytical method to predict the propagation of inclined cracks. Their calculated two dimensional stress intensity factors were close to those obtained from the boundary element analysis using FRANC3D. The propagation paths from their case studies exhibited close alignment with those obtained from FRANC3D and literature. To the knowledge of the authors, the work presented in this paper is the first attempt to extend the method described in Rahman *et al.* [3] to three dimensional applications.

The key advantage of the three dimensional methods is that they allow determination of the way a pre-existing crack re-orientates in the presence of various in-situ compressive stress regimes. In order to design effective hydraulic fracturing operations, it is important to determine this resultant crack propagation surface since the resultant fracture network provides the major permeable pathways for fluid or gas flow. A properly established three dimensional hydraulic fracturing propagation model can assist in the design of the stimulated fracture network to better target the gas zone or geothermal energy resources. Therefore, it is of significant practical importance to develop an efficient and accurate method to predict the three dimensional propagation surfaces resulting from hydraulic fracturing.

To assist the development of such a mixed mode propagation method, the primary problem is simplified to a uniformly pressurised circular crack in an infinite medium subjected to uniform far-field stresses. Kassir and Sih [8] developed an analytical method

to evaluate stress intensity factors of all three fracturing modes (opening, shearing and tearing) for a circular and an elliptical planar crack given an arbitrarily loading regime based on the linear elastic fracture mechanics (LEFM) theory. It is well documented that these fracturing modes have a combined effect on the resultant crack propagation surface in rocks and other brittle materials [9-12].

In this paper, an analytical approach is developed to approximate the mixed mode propagation of a circular crack, by considering a fictitious equivalent elliptical crack and utilising the maximum tangential stress criterion [13]. This fictitious elliptical crack assumes the surface and front formed by the propagation process are on the same plane. This assumption proved effective and satisfactory as the predicted propagation surfaces closely align with published results. Another simplification is using the effective normal and shear stresses to calculate the stress intensity factors, which is justified by the close alignment of their resultant values with the numerical results obtained from FRANC3D [14]. The stress tensor for the fictitious planar crack is also comparable to the stress tensor obtained from ABAQUS for the equivalent kinked crack. The finite element method (FEM) and the boundary element method (BEM) are still slower than the proposed analytical approach, even if the above approximations are used.

In summary, this paper presents an approximate three dimensional analytical method that can solve the crack propagation problem efficiently for an arbitrarily orientated circular internal crack. A planar crack propagation surface and front are assumed to simplify the problem and the maximum tangential stress criterion is used.

2 Theory and calculations

2.1 Problem setup

Consider a circular crack with a radius of a and orientated with a normal vector $\bar{v}_n$ in an infinite ideally brittle rock block subjected to a three dimensional stresses. The crack is internally pressurised by a fluid pressure P. The three principal effective stresses: σ'_x, σ'_y and σ'_z are orientated along the *x*, *y* and *z* axes, respectively (see Fig. 1).

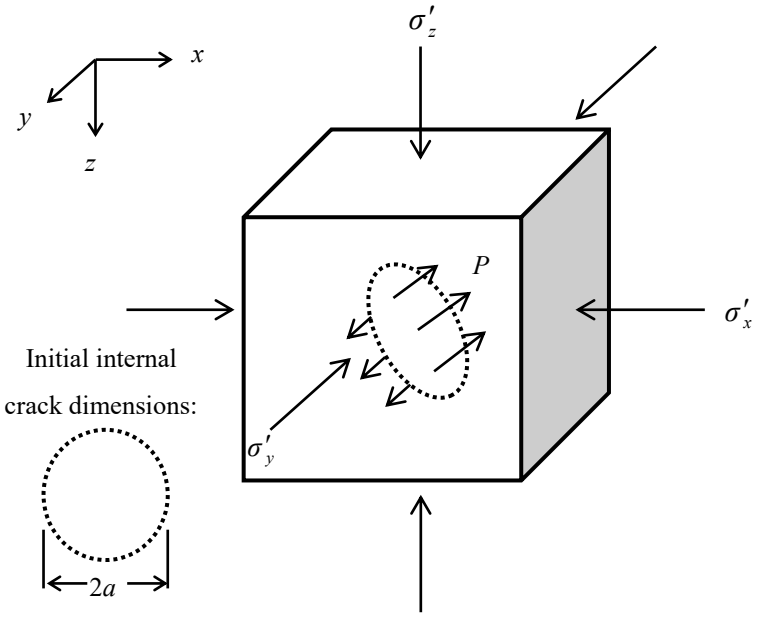

Fig. 1 Problem formulation

This is a mixed-mode problem, so opening and shearing modes are considered together when analysing the propagation of this circular crack. The shearing mode is produced by unequal remote external compressive stresses.

Using spherical coordinates r, φ, and θ (see Fig. 3), the stress state at the crack front can be defined by the stress intensity factors. The stress intensity factors are defined as the product of the stress at the crack front at $\theta = 0$ and $\sqrt{2\pi r}$ when $r \to 0$, i.e., [15]:

$$\begin{aligned} K_I(\varphi) &= \lim_{r\to 0} \sigma_\theta(r,\varphi,\theta=0)\sqrt{2\pi r} \\ K_{II}(\varphi) &= \lim_{r\to 0} \tau_{r\theta}(r,\varphi,\theta=0)\sqrt{2\pi r} \\ K_{III}(\varphi) &= \lim_{r\to 0} \tau_{t\theta}(r,\varphi,\theta=0)\sqrt{2\pi r} \end{aligned} \quad (1)$$

It has been observed that the concept of stress intensity factors, defined above, can predict the propagation of pre-existing macroscopic cracks [13]. These definitions are used below to convert the stress intensity factors of the fictitious planar elliptical crack to the stress intensity factors of the kinked crack. Note that this work is explicitly for an embedded circular crack.

2.2 Approximated stress intensity factors for an initially circular planar crack

The stress intensity factors of mode I, II and III for a circular crack can be evaluated using the formulations outlined by Tada *et al.* [16]. Note, in this paper the shear angle ω, is defined in the crack plane, clockwise around the normal vector in the positive z axis direction, following the system used in FRANC3D. Since Tada *et al.* [16] defined the

shear angle ω, clockwise around the negative z direction, the $K_{II}(\varphi)$ and $K_{III}(\varphi)$ values defined by Tada *et al.* [16] must be modified accordingly to obtain the stress intensity factors consistent to the definitions used in FRANC3D. The stress intensity factors given in Eq. 2 are considered approximate since the net pressure is used, rather than considering the internal pressure and the external compressive stress separately. Using the notations from Rahman *et al.* [3], the stress intensity factors can be expressed in the following general forms:

$$
\begin{aligned}
K_I(\varphi) &= 2\sqrt{\frac{a}{\pi}}\sigma_{n(eff)} \\
K_{II}(\varphi) &= -\frac{4\cos(\varphi-\omega)}{(2-\upsilon)}\sqrt{\frac{a}{\pi}}\tau_{eff} \\
K_{III}(\varphi) &= \frac{4(1-\upsilon)\sin(\varphi-\omega)}{(2-\upsilon)}\sqrt{\frac{a}{\pi}}\tau_{eff}
\end{aligned}
\tag{2}
$$

The normal unit vector $\bar{v}_n$ of the crack can be calculated from the dip direction α, and dip angle β, of the crack plane (see Fig. 2), as shown in Eq. 3. The dip direction here is defined as the clockwise rotation angle around the positive z axis from the positive x axis.

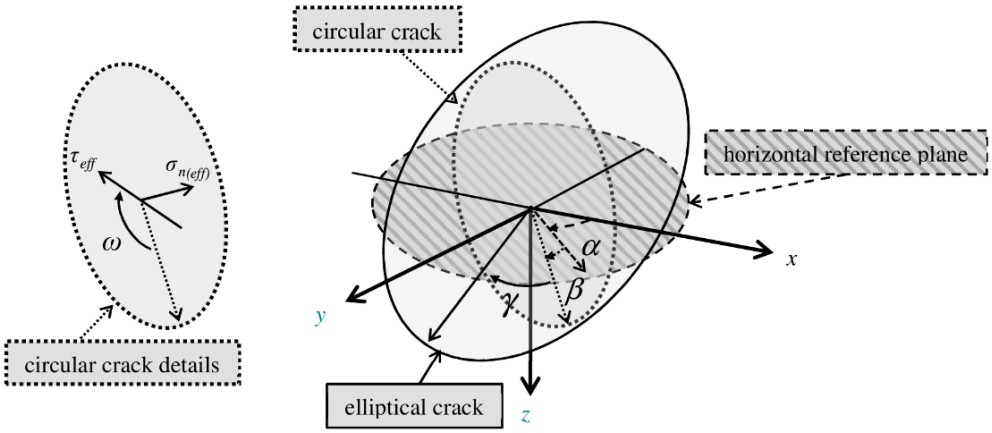

Fig. 2 Net pressure $\sigma_{n(eff)}$, shear stress τ_{eff}, shear angle ω, dip direction α, dip angle β, and ellipse angle γ definitions

$$
\bar{v}_n = \begin{bmatrix} l \\ m \\ n \end{bmatrix} = \begin{bmatrix} \cos(90°-\beta)\cos(\alpha) \\ \cos(90°-\beta)\sin(\alpha) \\ \sin(\beta-90°) \end{bmatrix}
\tag{3}
$$

Young and Budynas [17] published expressions to calculate the normal and shear stresses on a plane using the normal vector (l,m,n) for a given external three dimensional stress configuration. Since it is assumed that σ'_x, σ'_y, and σ'_z are the effective principal

stresses, then τ_{xy}, τ_{yz} and τ_{xz} are equal to zero. Therefore, for our considered system, the expressions for normal and shear stresses on a plane can be simplified to the following:

$$\begin{aligned}\sigma_{n(external)} &= \sigma'_x l^2 + \sigma'_y m^2 + \sigma'_z n^2 \\ \tau &= \sqrt{(\sigma'_x l)^2 + (\sigma'_y m)^2 + (\sigma'_z n)^2 - \sigma_{n(external)}{}^2}\end{aligned} \tag{4}$$

where the directional cosines of the shear vector are reduced to the following:

$$\begin{bmatrix} l_\tau \\ m_\tau \\ n_\tau \end{bmatrix} = \frac{1}{\tau}\begin{bmatrix} (\sigma'_x - \sigma_{n(external)})l \\ (\sigma'_y - \sigma_{n(external)})m \\ (\sigma'_z - \sigma_{n(external)})n \end{bmatrix} \tag{5}$$

The shear angle ω, is the angle between the shear direction (Eq. 5) and the vector obtained by projecting the dip direction on the crack plane (Eq. 6):

$$\begin{bmatrix} l_o \\ m_o \\ n_o \end{bmatrix} = \begin{bmatrix} \cos(\beta)\cos(\alpha) \\ \cos(\beta)\sin(\alpha) \\ \sin(\beta) \end{bmatrix} \tag{6}$$

and can be calculated as:

$$\omega = \arccos\left(\frac{l_\tau l_o + m_\tau m_o + n_\tau n_o}{\sqrt{l_\tau{}^2 + m_\tau{}^2 + n_\tau{}^2}\sqrt{l_o{}^2 + m_o{}^2 + n_o{}^2}}\right) \tag{7}$$

The net normal pressure $\sigma_{n(eff)}$ is calculated as:

$$\sigma_{n(eff)} = P - \sigma_{n(external)} = P - \left(\sigma'_x l^2 + \sigma'_y m^2 + \sigma'_z n^2\right) \tag{8}$$

Since the shear resistance τ_r, for the case of a crack opened by the fluid pressure is very small compared to the shear stress (as crack surfaces are not in contact and there is only small frictional resistance due to fluid viscosity), it can be neglected and therefore the effective shear stress becomes:

$$\tau_{eff} = \tau - \tau_r = \sqrt{(\sigma'_x l)^2 + (\sigma'_y m)^2 + (\sigma'_z n)^2 - \sigma_{n(external)}{}^2} \tag{9}$$

The reason for presenting the normal and shear stresses and shear angle using the normal vector of the arbitrarily orientated plane is to provide direct expressions for the stress intensity factors that make the analytical propagation method easier to apply or extend, as discussed below.

2.3 Crack propagation directions using maximum tangential stress criterion

The maximum tangential stress criterion, proposed by Erdogan and Sih [13], is utilised to determine the crack propagation direction. This criterion uses the maximum

circumferential tangential stress σ_θ, near the crack front. Hence, the formulation of Sih and Liebowitz [18] on the stress distribution near a circular (or elliptical) crack is used (see Fig. 3). These stress definitions are normalised by $\sqrt{\pi}$ to be consistent with the definition of the stress intensity factor given in Section 2.1, where higher order terms are omitted because of their negligible influence:

$$
\begin{aligned}
\sigma_n &= \frac{K_I(\varphi)}{4\sqrt{2\pi r}}\left[3\cos\left(\frac{\theta}{2}\right)+\cos\left(\frac{5\theta}{2}\right)\right]-\frac{K_{II}(\varphi)}{4\sqrt{2\pi r}}\left[7\sin\left(\frac{\theta}{2}\right)+\sin\left(\frac{5\theta}{2}\right)\right]\\
\sigma_t &= \frac{K_I(\varphi)}{\sqrt{2\pi r}}2\upsilon\cos\left(\frac{\theta}{2}\right)-\frac{K_{II}(\varphi)}{\sqrt{2\pi r}}2\upsilon\sin\left(\frac{\theta}{2}\right)\\
\sigma_z &= \frac{K_I(\varphi)}{4\sqrt{2\pi r}}\left[5\cos\left(\frac{\theta}{2}\right)-\cos\left(\frac{5\theta}{2}\right)\right]-\frac{K_{II}(\varphi)}{4\sqrt{2\pi r}}\left[\sin\left(\frac{\theta}{2}\right)-\sin\left(\frac{5\theta}{2}\right)\right]\\
\tau_{tz} &= \frac{K_{III}(\varphi)}{\sqrt{2\pi r}}\cos\left(\frac{\theta}{2}\right)\\
\tau_{zn} &= -\frac{K_I(\varphi)}{4\sqrt{2\pi r}}\left[\sin\left(\frac{\theta}{2}\right)-\sin\left(\frac{5\theta}{2}\right)\right]+\frac{K_{II}(\varphi)}{4\sqrt{2\pi r}}\left[3\cos\left(\frac{\theta}{2}\right)+\cos\left(\frac{5\theta}{2}\right)\right]\\
\tau_{nt} &= -\frac{K_{III}(\varphi)}{\sqrt{2\pi r}}\sin\left(\frac{\theta}{2}\right)
\end{aligned}
\tag{10}
$$

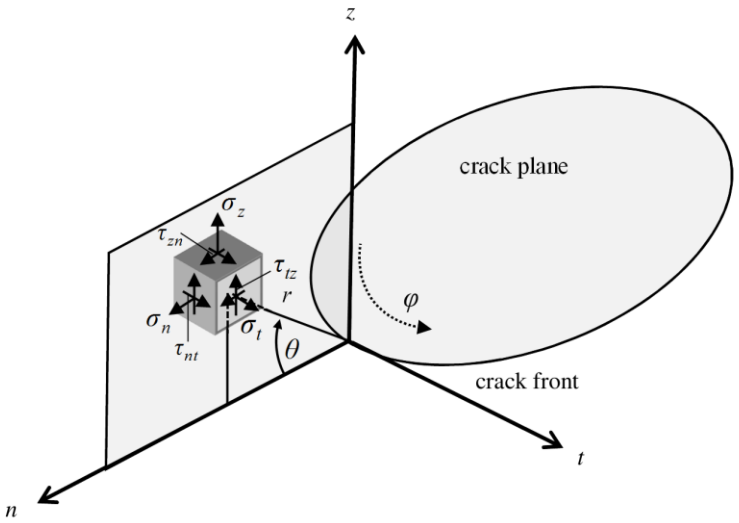

Fig. 3 Rectangular stress components in a plane normal to the crack border

According to the maximum tangential stress criterion [13], the crack extends from the crack front radially in the direction of the greatest tension.

The local stresses at the crack front can be obtained by converting the stresses in Eq. 10 from a cylindrical coordinate system to a spherical coordinate system using a rotation matrix defined by rotation against the t axis by θ (as shown in Fig. 3) i.e.:

$$
\begin{aligned}
\sigma_r &= \frac{1}{\sqrt{2\pi r}}\left[K_I(\varphi)\left(2\cos\left(\frac{\theta}{2}\right)-\cos^3\left(\frac{\theta}{2}\right)\right)+K_{II}(\varphi)\left(\sin\left(\frac{\theta}{2}\right)-3\sin^3\left(\frac{\theta}{2}\right)\right)\right]\\
\sigma_t &= \frac{2\upsilon}{\sqrt{2\pi r}}\left[K_I(\varphi)\cos\left(\frac{\theta}{2}\right)-K_{II}(\varphi)\sin\left(\frac{\theta}{2}\right)\right]\\
\sigma_\theta &= \frac{\cos^2\left(\frac{\theta}{2}\right)}{\sqrt{2\pi r}}\left[K_I(\varphi)\cos\left(\frac{\theta}{2}\right)-3K_{II}(\varphi)\sin\left(\frac{\theta}{2}\right)\right]\\
\tau_{rt} &= \frac{K_{III}(\varphi)}{\sqrt{2\pi r}}\sin\left(\frac{\theta}{2}\right)\\
\tau_{r\theta} &= \frac{\cos\left(\frac{\theta}{2}\right)}{2\sqrt{2\pi r}}\left[K_I(\varphi)\sin\theta+K_{II}(\varphi)(3\cos\theta-1)\right]\\
\tau_{t\theta} &= \frac{K_{III}(\varphi)}{\sqrt{2\pi r}}\cos\left(\frac{\theta}{2}\right)
\end{aligned}
\tag{11}
$$

Therefore σ_θ is a maximum when:

$$
\theta_c(\varphi)=\begin{cases}0^\circ & \text{if } K_{II}(\varphi)=0\\ 2\arctan\left[\dfrac{K_I(\varphi)\pm\sqrt{{K_I}^2(\varphi)+8{K_{II}}^2(\varphi)}}{4K_{II}(\varphi)}\right] & \text{if } K_{II}(\varphi)\neq 0\end{cases}
\tag{12}
$$

Using these critical θ values, the maximum tangential tensile stress in the crack front can be evaluated using the following expression:

$$
\sigma_\theta\sqrt{2\pi r}=\cos^2\left(\frac{\theta_c(\varphi)}{2}\right)\left[K_I(\varphi)\cos\left(\frac{\theta_c(\varphi)}{2}\right)-3K_{II}(\varphi)\sin\left(\frac{\theta_c(\varphi)}{2}\right)\right]
\tag{13}
$$

2.4 Crack front propagation path modelling

In this paper, the focus is placed on developing an approximate but simple, purely analytical method for the evaluation of stress intensity factors for the discussed problem, which is well defined. If the crack propagation increment is constant around the circumference of the crack, the crack front will not be on the same plane after propagation due to different θ_c values at different φ points. If the subsequent crack front is not planar, the stress intensity factors for the next step cannot be calculated analytically. Hence, to calculate the stress intensity factors using the analytical solution developed by Kassir and Sih [8], it is necessary to consider a fictitious planar crack front. Note that segmentation from mode III fracturing is not considered with this approach, since the maximum tangential stress criterion is used. Details of the calculation for the fictitious planar crack front used in this work are given in Appendix A and B. Note that the elliptical planar (fictitious) crack front is assumed in this case only to solve the

propagation problem analytically. It is acknowledged that in reality, the geometry of actual crack propagation front in each time step may be more complex.

2.5 Approximated stress intensity factors for a planar elliptical fictitious crack

The stress intensity factors for a planar elliptical fictitious crack can be approximated by the following expressions as outlined in Tada *et al.* [16] using the same concept described in Section 2.2.

$$
\begin{aligned}
K_I(\varphi) &= \frac{\sigma_{n(eff)}}{E(k)}\sqrt{\frac{\pi b}{a}}\left[a^2\sin^2(\varphi)+b^2\cos^2(\varphi)\right]^{1/4} \\
K_{II}(\varphi) &= -\frac{\tau_{eff}k^2\sqrt{\pi ab}}{\left[a^2\sin^2(\varphi)+b^2\cos^2(\varphi)\right]^{1/4}}\left[\frac{k'}{B}\cos(\omega)\cos(\varphi)+\frac{1}{C}\sin(\omega)\sin(\varphi)\right] \\
K_{III}(\varphi) &= \frac{\tau_{eff}k^2(1-\upsilon)\sqrt{\pi ab}}{\left[a^2\sin^2(\varphi)+b^2\cos^2(\varphi)\right]^{1/4}}\left[\frac{1}{B}\cos(\omega)\sin(\varphi)-\frac{k'}{C}\sin(\omega)\cos(\varphi)\right]
\end{aligned}
\tag{14}
$$

The concept of a fictitious crack is used where the effective normal stress $\sigma_{n(eff)}$, and shear stress τ_{eff}, are calculated using the dip direction α, and dip angle β, of the plane defined by the crack propagation front.

To compare the result of the fictitious crack with that of the kinked crack from FRANC3D; the analytical stress intensity factors based on the fictitious plane (Eq. 14) were converted to their kinked coordinate system values by using the spherical coordinate stress system (Eq. 11). The angles of interest $\theta_{kink}(\varphi)$ are the difference from the radial vector of the current fictitious plane to the kinked radial lines (see Fig. 4 for a graphical representation of the definition).

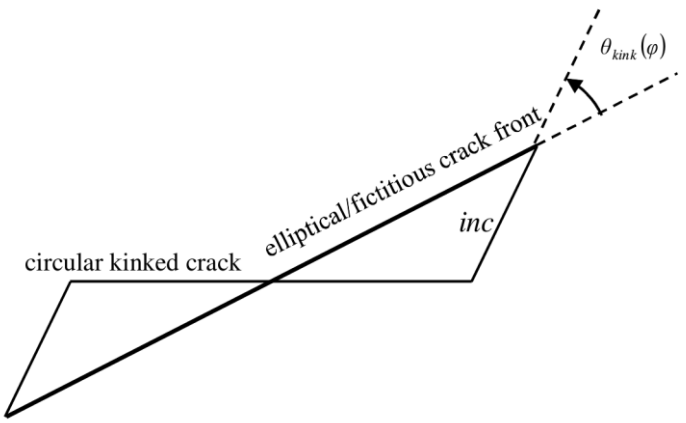

Fig. 4 Definition of the angle of interest (to convert the fictitious planar stress intensity factors to a kinked coordinate system defined and used in FRANC3D)

Note the two definitions for stress intensity factors of the planar fictitious crack and the kinked crack are fundamentally different since the planar fictitious crack does not consider the kink of the propagation surface. To compare the stress tensor of the planar fictitious crack from Eq. 11 with those from finite element analysis (ABAQUS), the stress intensity factors for a kinked crack were assessed (Eq. 15). The stress components of the numerical and analytical models were compared in Section 3. Note the angles of interest are generally not zero since the radial directions from planar fictitious crack to the radial vectors of the kinked section of the crack are not aligned. This concept produces a spatial stress tensor comparable to that obtained from finite element analysis.

$$
\begin{aligned}
&K_{I(kinked)}(\varphi) = \sigma_\theta \sqrt{2\pi r} \\
&= \cos^2\left(\frac{\theta_{kink}(\varphi)}{2}\right)\left[K_I(\varphi)\cos\left(\frac{\theta_{kink}(\varphi)}{2}\right) - 3K_{II}(\varphi)\sin\left(\frac{\theta_{kink}(\varphi)}{2}\right)\right] \\
&K_{II(kinked)}(\varphi) = \tau_{r\theta} \sqrt{2\pi r} \\
&= \frac{1}{2}\cos\left(\frac{\theta_{kink}(\varphi)}{2}\right)\left[K_I(\varphi)\sin\theta_{kink}(\varphi) + K_{II}(\varphi)(3\cos\theta_{kink}(\varphi) - 1)\right] \\
&K_{III(kinked)}(\varphi) = \tau_{t\theta} \sqrt{2\pi r} = K_{III}(\varphi)\cos\left(\frac{\theta_{kink}(\varphi)}{2}\right)
\end{aligned}
\tag{15}
$$

The pressure P, is maintained from the previous step during crack propagation. For details of the propagation surface modelling when the crack front is elliptical, see Appendix B. By using a planar fictitious crack and following the process described, the entire propagation path of the crack can be traced in the three dimensional space.

3 Results and discussion

This section presents a comparison study between the published results of Rahman *et al.* [3] and the current results using the method proposed in this paper.

The geometric and mechanical properties of the model analysed in this study are shown in Table 1. Note, that the principal compressive stresses and breakdown pressure used are higher than those for practical hydraulic fracturing operations. These stresses and pressure are chosen to be comparable with the study described in Rahman *et al.* [3].

Table 1 Model geometric and mechanical properties

Property type	Properties	Value
Geometric	Model X dimension	1 m
	Model Y dimension	1 m
	Model Z dimension	1 m
	Initial crack shape	Circular
	Initial crack radius	0.1 m
	Crack position	At the centre of the block
	Crack inclination	Case 1 – dip direction = 0° and dip angle = 15° Case 2 – dip direction = 0° and dip angle = 30° Case 3 – dip direction = 0° and dip angle = 45°
Mechanical	σ'_x	92 MPa
	σ'_y	92 MPa
	σ'_z	63 MPa
	Pressure inside the crack	80 MPa
	Poisson's ratio	0.25
	Elastic modulus	20 GPa

The FRANC3D software package is designed to simulate crack growth in materials with a complex geometry, loading conditions and crack configuration [14]. In FRANC3D, the stress intensity factors are calculated using the M-integral [19] based on the finite element analysis results obtained from commercial codes such as ABAQUS, NASTRAN or ANSYS. FRANC3D can then determine the propagation directions of the crack front using the maximum tangential stress criterion. To determine the subsequent crack front, FRANC3D varies the extension lengths $inc_{FRANC3D}(\varphi)$ using inputs of the median crack increment value a_{median}, and a power value n. The extension lengths are calculated by multiplying the median crack increment value by the relative change in mode I stress intensity factor with respect to the median mode I stress intensity factor $K_{I(median)}$ to the power of n:

$$inc_{FRANC3D}(\varphi) = a_{median}\left[\frac{K_I(\varphi) - K_{I(median)}}{K_{I(median)}}\right]^n \tag{16}$$

This crack front is then smoothed by fitting a polynomial curve (with a user defined order that will give the best fit) to these calculated points. However, this propagation method implemented is problematic, since the crack is initially circular and hence the mode I stress intensity factors do not vary significantly. The lack of change in this stress intensity factor produces almost constant extension lengths in FRANC3D. Consequently, once the crack kinks, the mesh cannot be generated properly in the first or subsequent steps. In addition, in FRANC3D the increment length $inc_{FRANC3D}(\varphi)$, cannot be below a critical value, as the mesh generator will then have difficulty to generate the mesh rosette required by the program. Consequently, the finite element model cannot be updated and the stress intensity factors and propagation for this particular scenario cannot be

predicted. The analytical propagation method proposed does not have these issues. Note however, using an elliptical crack front in the first propagation step in FRANC3D solves the mesh generation issue of the kinked crack, but not the increment length issue.

The stress intensity factors for the pre-existing circular crack of case 3 calculated by FRANC3D and our proposed analytical method (see Eq. 2), follow each other closely, and overlap, as presented in Fig. 5. The normalised crack front value (horizontal axis) is the circumference of the crack front from the x axis in the positive φ direction.

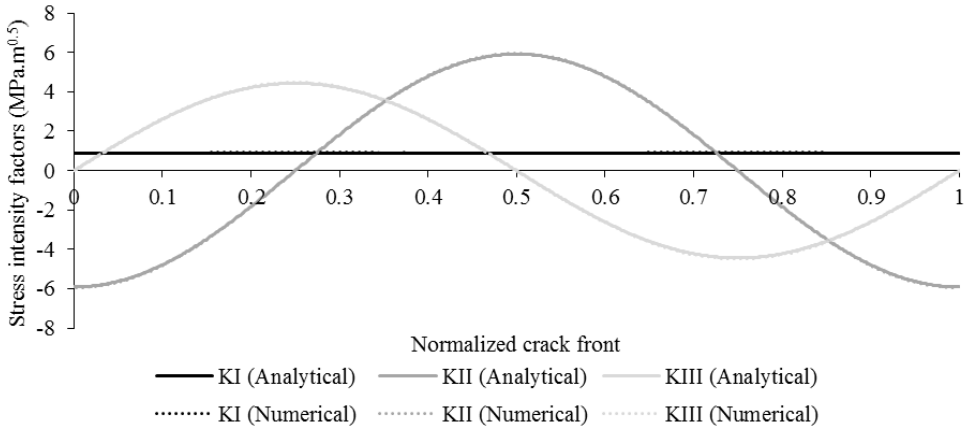

Fig. 5 Comparison of stress intensity factors using the pre-existing crack for case 3 from Table 1 (analytical values and numerical results)

The coefficient of determination (R^2) regression values between the two methods for mode I, II and III are 0.9999369, 0.9999985, and 0.9999979, respectively. In addition, the factors generated by the linear regression for mode I, II and III analytical values were 1.015, 1.007 and 1.012, respectively, which demonstrate that the results between the two approaches agree extremely well in this case.

Similarly, the analytical stress intensity factors for the kinked crack in case 3 (Table 1), generated from the fictitious spatial stress tensor, after the application of the conversion above, were compared to the numerical results obtained from FRANC3D, as shown in Fig. 6 (see Section 2.5 for details of this conversion). The coefficient of determination (R^2) for mode I, II, and III for the kinked crack are 0.99707, 0.98331, and 0.99810, respectively, which indicate that the results from the two methods are closely related. The regression coefficients generated from the linear regression for modes I, II and III were 1.018, 1.572, and 1.498, respectively, suggesting the mode I stress intensity factors agree well, but mode II and III stress intensity factors differ by a proportion. However, the trends of variations from the two methods still align closely with each other (see Fig. 6). As the mode III stress intensity factor will not affect the determination of the

propagation path when the maximum tangential stress criterion is used, only mode I and II are needed to predict the propagation direction and surface in the present study. The stress intensity factors for mode I and II from the two methods aligned well with each other along the crack front, especially for $\varphi = 0°,\ 90°,\ 180°,$ and $270°$ (see Fig. 6). Therefore, the two methods are expected to produce similar propagation surfaces. It is worthwhile to emphasise that the key purpose of the proposed method is not to evaluate the accurate stress intensity factors for a kinked crack, but to provide a simplified method to assess the overall trend of the propagation surface of an arbitrarily orientated crack.

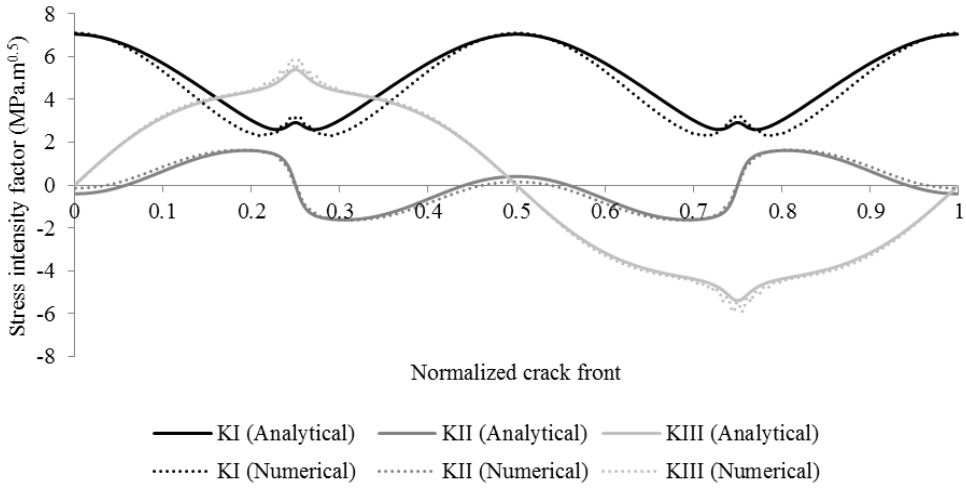

Fig. 6 Comparison of stress intensity factors using a kinked crack for case 3 from Table 1 (analytical values with regression factors applied and numerical results)

Using a propagation step size of 10% of the initial crack radius ($inc = 0.01$ m), a three dimensional propagation path for 20 steps was computed using the proposed method for case 3 (see Table 1) and the result is shown in Fig. 7, and Fig. 8 (note that for clarity the plot scale is exaggerated in z direction in these figures). The increment length of 10% of the initial crack radius was chosen based on the experience of Rahman *et al.* [3], where a range between 5% to 10% provides reasonably accurate results for their two dimensional model. This increment value could be related or equal to the critical distance [20]. The crack only twists in the vertical direction and realigns to the horizontal plane, because the horizontal stresses are equal and the vertical stress is lower than the horizontal stresses. The angles when the tangential stress is a maximum determine the propagation surface. Therefore, for this configuration the maximum tangential stress is produced when the crack realigns to the horizontal plane.

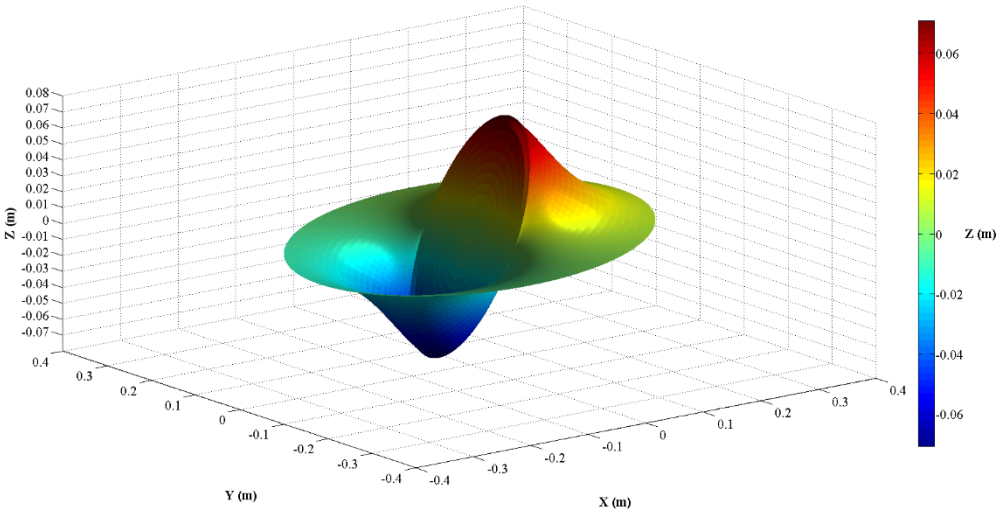

Fig. 7 Propagation surface for case 3 derived from the analytical method

The propagation path on the XZ cross section through the middle of the model aligns well with the two dimensional results from the previous study by Rahman *et al.* [3] (see Fig. 8).

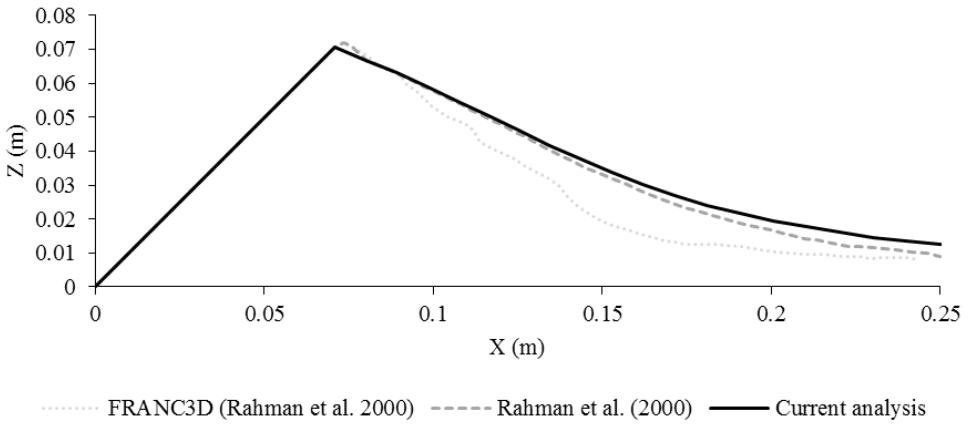

Fig. 8 Cross section along the *x* axis of propagation surface for case 3 compared with the previous study by Rahman *et al.* [3]

For case 2 in Table 1, using the same settings, a three dimensional propagation surface was calculated using the proposed method and the result is shown in Fig. 9.

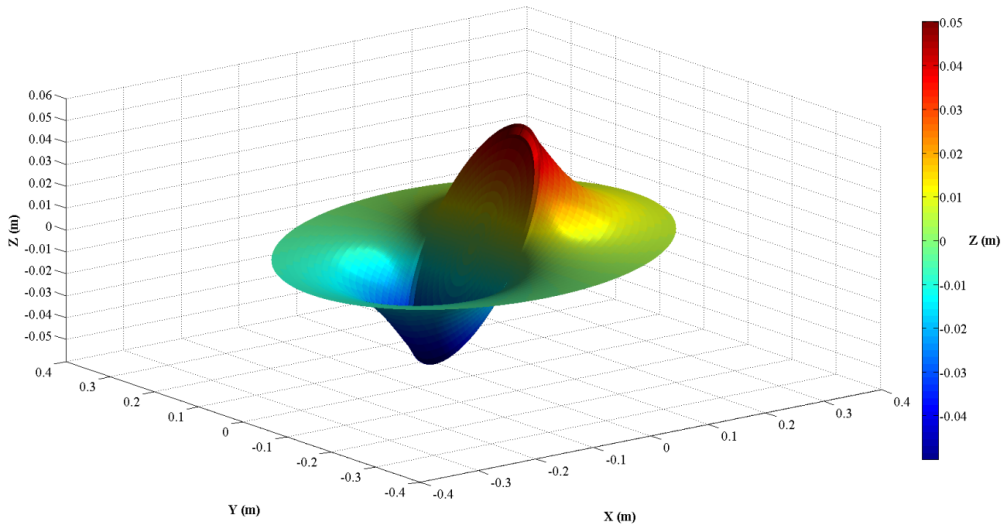

Fig. 9 Propagation surface for case 2 derived from the analytical method

Similar to case 3, the propagation profile on XZ cross section closely aligns with the results of the previous two dimensional study [3] (see Fig. 10).

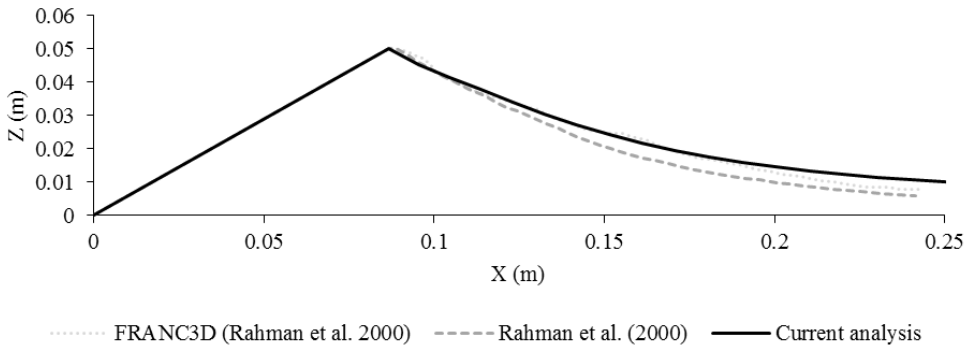

Fig. 10 Cross section along the *x* axis of propagation surface for case 2 compared with the previous study by Rahman *et al.* [3]

For case 1 in Table 1, the result using the same settings is shown in Fig. 11.

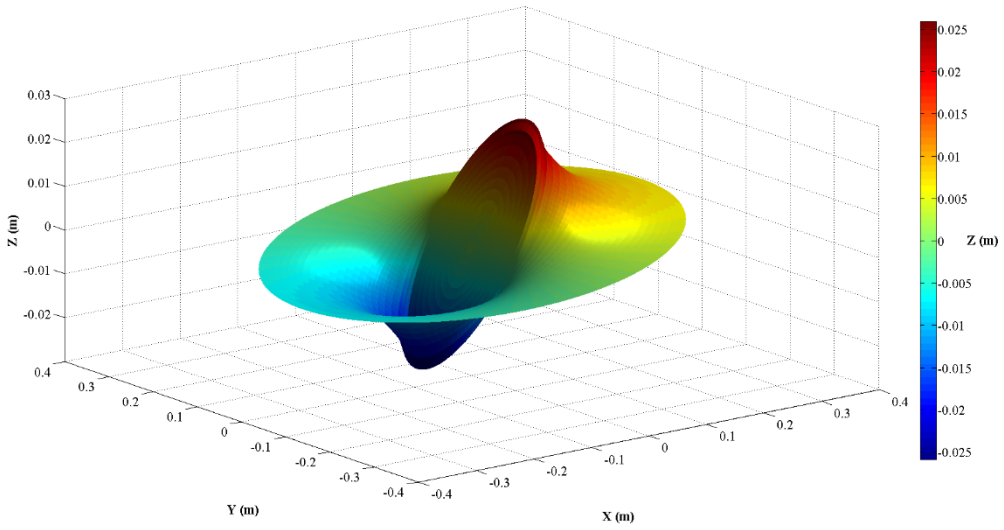

Fig. 11 Propagation surface for case 1 derived from the analytical method

The propagation profile on XZ cross section follows the same trend as that of previous analyses by Rahman *et al.* [3], but the current analysis produces a slightly higher propagation path (see Fig. 7).

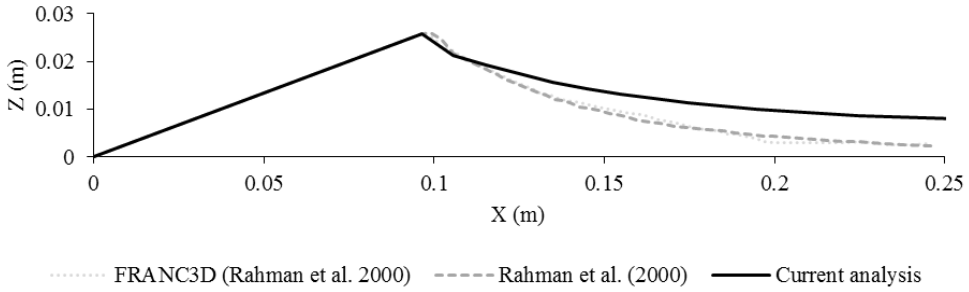

Fig. 12 Cross section along the *x* axis of propagation surface for case 1 compared with the previous study by Rahman *et al.* [3]

The higher propagation path for case 1 is because the calculation of the stress intensity factors in the proposed method is based on an elliptical crack rather than on a circular or two dimensional linear crack and this is considered to be more realistic to represent the actual situation. Detailed examinations of case 2 (see Fig. 10) and case 3 (see Fig. 8) indicate that both resultant propagation paths defined by the analytical method are higher than the results from Rahman *et al.* [3], but with little significance. This suggests a trend where the difference is greater for pre-existing cracks with lower dip angles. This can be explained by using the same parameters as for the discussed three cases and assuming 0.1 m as the major axis of ellipse dimensions. When the ratio of minor to major axes of the ellipse becomes less than one, the crack becomes elliptical and the absolute value of $\theta_{c(\max)}$ is smaller than the absolute value of $\theta_{c(\max)}$ when a circular crack front is

assumed. A smaller absolute value of $\theta_{c(\max)}$ produces a higher crack propagation path, since this determines how much the crack kinks. Therefore, using stress intensity factors based on elliptical cracks, the absolute value of $\theta_{c(\max)}$ is always smaller and hence produces a higher propagation path compared with that when the stress intensity factors based on circular cracks are used, as with Rahman *et al.* [3]. In other words, if the stress intensity factors based on elliptical cracks are not used, the resultant height of the crack propagation is underestimated, especially for cracks with lower dip angles. The value of $\theta_{c(\max)}$ is accurate at the apex of the crack, since the stress intensity factors for a kinked crack are aligned to the analytical values at these points; for example, see Fig. 6 when $\varphi = 0°,$ and $180°.$ For cracks with higher dip angles, the results from the proposed method align closely with the published results of Rahman *et al.* [3].

4 Conclusions

In this paper, an efficient three dimensional analytical method using the LEFM theory was developed to solve the propagation problem of an arbitrarily orientated pressurised circular crack under different external compressive stresses. The stepwise solution is derived from the concept of a fictitious crack surface and the maximum tangential stress criterion.

The proposed method is efficient and can produce results using a fraction of the time needed for a full finite element or boundary element analysis. However, it is not intended to replace finite element or boundary element analyses, but rather to provide a propagation algorithm that can be used for a quick assessment or in conjunction with these numerical analyses. As demonstrated, the results obtained from the proposed method align closely with published two dimensional studies.

As demonstrated in this study, the transformation from the initial crack geometry to the final crack surface is a complex process and generally involves curved propagation surfaces. It is important to be able to predict these curved propagation surfaces to understand the detailed fracture network developed by hydraulically fracturing the reservoir. The proposed analytical method provides an efficient tool to help to address this problem, though an extension to cover interacting propagating cracks is necessary. In addition, experimental validation of the results produced by the proposed method will need to be conducted.

Appendix

A. Crack propagation path when the initial crack is circular

The subsequent planar propagated crack front can be defined using all the corresponding crack propagation angles $\theta_c(\varphi)$ from the previous crack front, even if the propagation process kinks the crack. See Fig. A.1 for the geometric description of variables used to model the crack front.

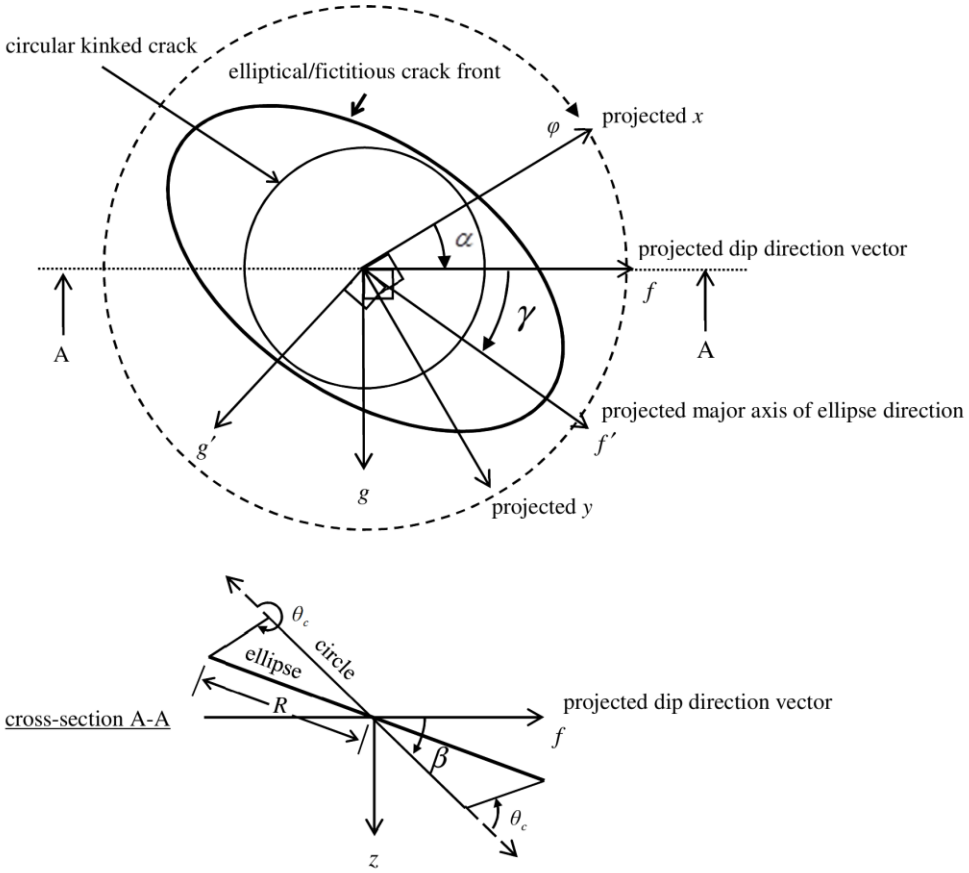

Fig. A.1 Geometric description of variables using circular to elliptical crack fronts

To generate a planar crack propagation front, a predefined constant increment value inc, is used at two particular points only, which is at $\varphi_{\max}$, corresponding to the maximum mode II stress intensity factor values. These two points are in the shear direction ω, and are 90° from the point φ_{zero}, where the stress intensity factor for mode II is zero, i.e.:

$$\varphi_{\max} = \varphi_{zero} \pm 90° \tag{A.1}$$

According to the maximum tangential stress criterion, at the φ_{zero} point, the crack propagation is in the same plane as the initial crack plane, since the mode II stress

intensity factor is equal to zero. For a circular crack, stress intensity factors for mode II are equal to zero when the crack front angle is at 90° from the shear angle ω, i.e.:

$$\varphi_{zero} = \omega \mp 90° \tag{A.2}$$

Subsequently, $\varphi_{\max}$ and $\theta_c(\varphi)$ can be calculated and hence a reference point on the propagated crack front can be determined (see Fig. A.2).

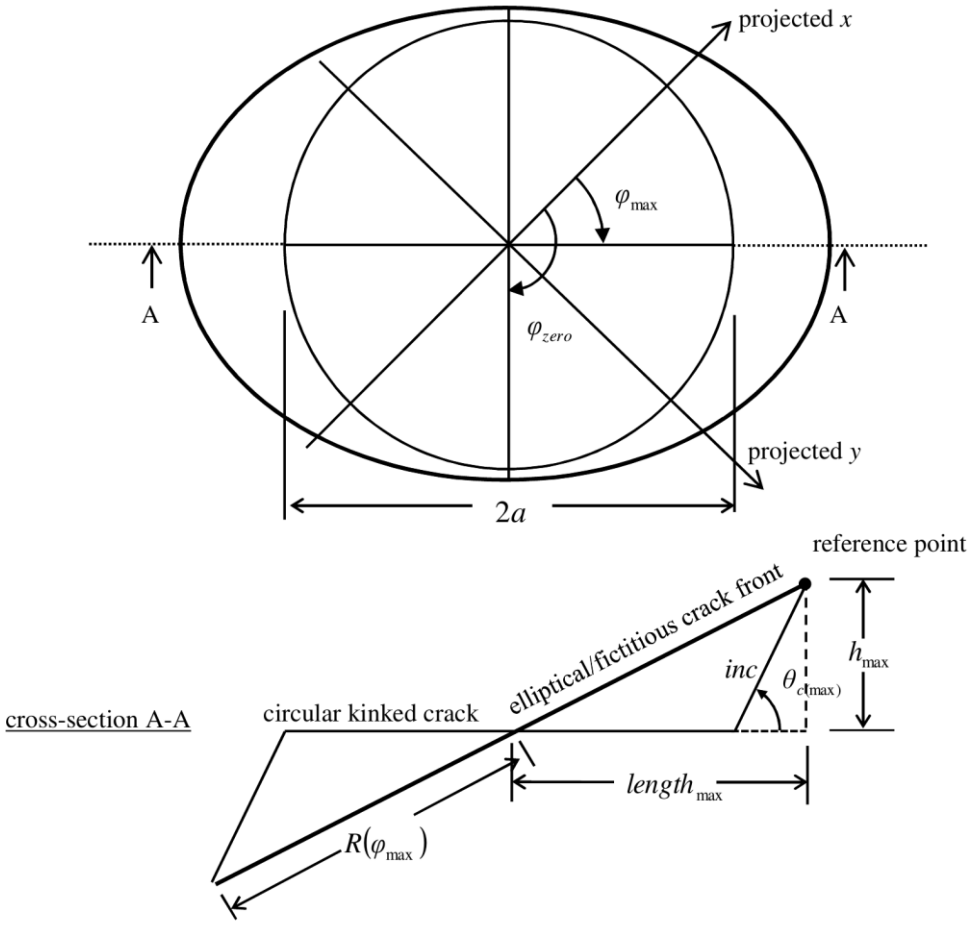

Fig. A.2 Circular to elliptical propagation step diagram

For the convenience of calculating the propagation profile, a local crack plane coordinate system is introduced, where f is in the dip direction of the original crack plane, g is perpendicular to f and on the plane of the circular crack, and h is perpendicular to the crack plane. Therefore, the slope of the crack plane after propagation is $h_{\max}/length_{\max}$ in the $\varphi_{\max}$ direction (see Fig. A.2), which can be calculated as:

$$\frac{h_{\max}}{length_{\max}} = \frac{(inc)\sin(\theta_{c(\max)})}{a + (inc)\cos(\theta_{c(\max)})} \tag{A.3}$$

The other orthogonal local coordinates h from the crack plane for different φ points are calculated as:

$$h(\varphi) = (inc)\sin(\theta_{c(\max)})\cos(\varphi - \varphi_{\max}) \tag{A.4}$$

Therefore, the radial coordinates of the crack front after crack propagation can be calculated from the following expression:

$$length(\varphi) = a + \frac{h(\varphi)}{\tan(\theta_c(\varphi))} \quad \text{if } \theta_c(\varphi) \neq 0° \tag{A.5}$$

When the crack propagation angle is zero, i.e. $\theta_c(\varphi) = 0°$ the crack growth is planar but Eq. A.5 does not evaluate and therefore an approximation is used by averaging the radial coordinates of neighbourhood points.

The radial lengths from the origin to the subsequent propagation front can then be calculated from the following expression:

$$R(\varphi) = \sqrt{length^2(\varphi) + h^2(\varphi)} \tag{A.6}$$

The local vectors of the subsequent crack front after crack propagation can then be calculated as:

$$\begin{bmatrix} f(\varphi) \\ g(\varphi) \\ h(\varphi) \end{bmatrix} = \begin{bmatrix} length(\varphi)\cos(\varphi) \\ length(\varphi)\sin(\varphi) \\ h(\varphi) \end{bmatrix} \tag{A.7}$$

These coordinates can be transformed to the coordinates in the global system using the following expressions:

$$\begin{bmatrix} x(\varphi) \\ y(\varphi) \\ z(\varphi) \end{bmatrix} = \begin{bmatrix} f(\varphi)\cos(\beta)\cos(\alpha) - g(\varphi)\sin(\alpha) - h(\varphi)\cos(\alpha)\sin(\beta) \\ f(\varphi)\cos(\beta)\sin(\alpha) + g(\varphi)\cos(\alpha) - h(\varphi)\sin(\alpha)\sin(\beta) \\ f(\varphi)\sin(\beta) + h(\varphi)\cos(\beta) \end{bmatrix} \tag{A.8}$$

The normal vector $[x_{normal}, y_{normal}, z_{normal}]$, of the fictitious crack plane after crack propagation is calculated by the cross product of two vectors on the crack plane and then by converting them to the global coordinate system using Eq. A.8. Using this normal vector, the dip angle β, and dip direction α, for the subsequent fictitious crack plane after crack propagation can be calculated by Eq. A.9 and Eq. A.10, respectively:

$$\beta = \begin{cases} 0° & \text{if } \sqrt{x^2{}_{normal} + y^2{}_{normal}} = 0 \\ 90° - \left\| \arctan\left(\dfrac{z_{normal}}{\sqrt{x^2{}_{normal} + y^2{}_{normal}}} \right) \right\| & \text{if } \sqrt{x^2{}_{normal} + y^2{}_{normal}} \neq 0 \end{cases} \tag{A.9}$$

$$\alpha = \begin{cases} \arctan\left(y_{normal} / x_{normal}\right) + Q & \text{if } x_{normal} \neq 0 \\ 90° & \text{if } x_{normal} = 0 \text{ and } y_{normal} \geq 0 \\ 270° & \text{if } x_{normal} = 0 \text{ and } y_{normal} < 0 \end{cases} \tag{A.10}$$

where:

$$Q = \begin{cases} 0° & \text{if } x_{normal} \geq 0 \text{ and } y_{normal} \geq 0 \\ 180° & \text{if } x_{normal} < 0 \text{ and } y_{normal} \geq 0 \\ 180° & \text{if } x_{normal} < 0 \text{ and } y_{normal} < 0 \\ 360° & \text{if } x_{normal} \geq 0 \text{ and } y_{normal} < 0 \end{cases}$$

After the crack propagation, the propagation front on the fictitious crack plane can be approximated by an ellipse where the lengths of major and minor axis are calculated using the following expressions:

$$\begin{aligned} a &= \max\left[R(\varphi)\right] \\ b &= \min\left[R(\varphi)\right] \end{aligned} \tag{A.11}$$

The direction of the major axis of the ellipse, or ellipse angle γ, in relation to the crack front angle φ, is obtained from the location of the maximum radial length, i.e. the direction corresponding to the major axis a, in Eq. A.11.

B. Crack propagation path for subsequent steps when the fictitious planar crack is elliptical

When calculating the stress intensity factors for an elliptical fictitious planar crack, the angle φ, is defined as an apparent angle to the point of interest on the crack front from the major axis of the ellipse. The projection onto the actual ellipse, in the g' direction of the intersection of φ with the circumscribed circle provides the point of interest. The local coordinates of this point using this apparent angle are $\left[a\cos(\varphi), b\sin(\varphi), 0\right]$ (see Fig. B.1).

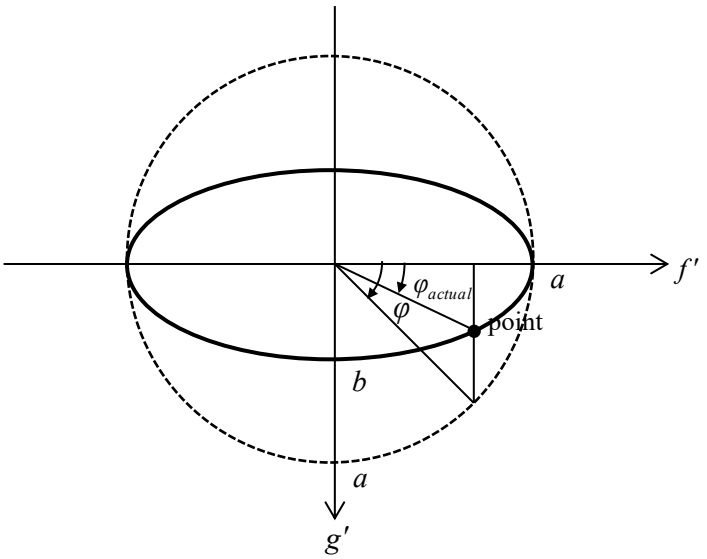

Fig. B.1 Definition of φ and φ_{actual}

Thus, the actual angle φ_{actual}, which is measured from the positive f' direction (the direction of the major axis of the ellipse) clockwise against the direction of the positive h' direction (the orthogonal component to f' and g'), can be determined from the following relationships (Eq. B.1):

$$\varphi_{actual} = \begin{cases} \arctan\left[b\sin(\varphi)/a\cos(\varphi)\right] + Q & \text{if } a\cos(\varphi) \neq 0 \\ 90° & \text{if } a\cos(\varphi) = 0 \text{ and } b\sin(\varphi) \geq 0 \\ 270° & \text{if } a\cos(\varphi) = 0 \text{ and } b\sin(\varphi) < 0 \end{cases} \tag{B.1}$$

where:

$$Q = \begin{cases} 0° & \text{if } a\cos(\varphi) \geq 0 \text{ and } b\sin(\varphi) \geq 0 \\ 180° & \text{if } a\cos(\varphi) < 0 \text{ and } b\sin(\varphi) \geq 0 \\ 180° & \text{if } a\cos(\varphi) < 0 \text{ and } b\sin(\varphi) < 0 \\ 360° & \text{if } a\cos(\varphi) \geq 0 \text{ and } b\sin(\varphi) < 0 \end{cases}$$

Similar to the discussions in Appendix A, two apparent angles exist where the stress intensity factors for mode II of an elliptical crack are equal to zero. These two angles are 180° apart and the corresponding points have planar crack growth, i.e. $\theta_c(\varphi_{zero}) = 0°$. One of these two angles φ_{zero} for an elliptical crack can be calculated by the following expression:

$$\varphi_{zero} = \begin{cases} \arctan\left[(-k'C)/B\tan(\omega)\right] + Q & \text{if } B\tan(\omega) \neq 0 \\ 90° & \text{if } B\tan(\omega) = 0 \text{ and } -k'C \geq 0 \\ 270° & \text{if } B\tan(\omega) = 0 \text{ and } -k'C < 0 \end{cases} \tag{B.2}$$

where:

$$Q = \begin{cases} 0° & \text{if } B\tan(\omega) \geq 0 \text{ and} -k'C \geq 0 \\ 180° & \text{if } B\tan(\omega) < 0 \text{ and } -k'C \geq 0 \\ 180° & \text{if } B\tan(\omega) < 0 \text{ and } -k'C < 0 \\ 360° & \text{if } B\tan(\omega) \geq 0 \text{ and } -k'C < 0 \end{cases}$$

Eq. B.2 is derived by determining the angle at which the stress intensity factor for mode II is equal to zero. Since φ_{zero} is an apparent angle, it corresponds to a point at the coordinates of $[f',g',h']=[a\cos(\varphi_{zero}),b\sin(\varphi_{zero}),0]$ in the current local crack plane coordinate system. The actual φ_{zero} angle $\varphi_{actual(zero)}$, can be calculated using the relationship presented in Eq. B.1. Hence, the reference point on the subsequent crack front can then be determined, where similar to the description given in Appendix A, $\varphi_{actual(\max)}$ is 90° from $\varphi_{actual(zero)}$.

Since the direction of the major axis of the ellipse may not be aligned with the dip direction of the crack plane, the general form of an ellipse must be used, i.e.:

$$\begin{bmatrix} f(\varphi) \\ g(\varphi) \\ h(\varphi) \end{bmatrix} = \begin{bmatrix} a\cos(\varphi)\cos(\gamma) - b\sin(\varphi)\sin(\gamma) \\ a\cos(\varphi)\sin(\gamma) + b\sin(\varphi)\cos(\gamma) \\ 0 \end{bmatrix} \tag{B.3}$$

where φ is defined, in this case, from the major axis of the ellipse direction.

Using the slope $h_{\max}/length_{\max}$ of the plane after propagation in the $\varphi_{actual(\max)}$ direction and projecting the orthogonal coordinates along an inclined plane results in the previous formulation (Eq. A.3). The radial coordinates (see Fig. A.2) can be calculated from the following expression:

$$length(\varphi) = \sqrt{\begin{matrix}[a\cos(\varphi)\cos(\gamma) - b\sin(\varphi)\sin(\gamma)]^2 \\ + [a\cos(\varphi)\sin(\gamma) + b\sin(\varphi)\cos(\gamma)]^2\end{matrix}} + \frac{h(\varphi)}{\tan(\theta_c(\varphi))} \quad \text{if } \theta_c(\varphi) \neq 0° \tag{B.4}$$

Similarly, when the crack angle is equal to zero, i.e. $\theta_c(\varphi)=0°,$ this expression above does not evaluate and therefore an approximation is used by averaging the radial coordinates of neighbourhood points.

The radial length from the origin (see Fig. A.2) for the subsequent crack front can be calculated from Eq. A.6. These subsequent local crack front vectors are calculated from the following formulae:

$$\begin{bmatrix} f(\varphi) \\ g(\varphi) \\ h(\varphi) \end{bmatrix} = \begin{bmatrix} length(\varphi)\cos(\varphi_{actual}) \\ length(\varphi)\sin(\varphi_{actual}) \\ h(\varphi) \end{bmatrix} \tag{B.5}$$

The cross product of two vectors on the subsequent fictitious crack plane after crack propagation is calculated then converted to the global system. This normal vector of the fictitious crack plane is subsequently used to calculate the dip angle and dip direction of this plane using Eq. A.9 and Eq. A.10, respectively.

Similar to the process discussed in Appendix A, the subsequent crack front after crack propagation can be approximated by an ellipse where the lengths of the major and minor axis are calculated from Eq. A.11. The ellipse angle γ, is then the angle φ, that makes the longest radial length.

References

[1] Warpinski N, Teufel L. Influence of geologic discontinuities on hydraulic fracture propagation (includes associated papers 17011 and 17074). J Pet Technol. 1987;39:209-20.

[2] Cherny S, Chirkov D, Lapin V, Muranov A, Bannikov D, Miller M, et al. Two-dimensional modeling of the near-wellbore fracture tortuosity effect. Int J Rock Mech Min Sci. 2009;46:992-1000.

[3] Rahman MK, Hossain MM, Rahman SS. An analytical method for mixed-mode propagation of pressurized fractures in remotely compressed rocks. Int J Fract. 2000;103:243-58.

[4] Huang K, Zhang Z, Ghassemi A. Modeling three-dimensional hydraulic fracture propagation using virtual multidimensional internal bonds. Int J Numer Anal Meth Geomech. 2012;37:2021-38.

[5] Zhang X, Jeffrey RG, Bunger AP, Thiercelin M. Initiation and growth of a hydraulic fracture from a circular wellbore. Int J Rock Mech Min Sci. 2011;48:984-95.

[6] Dong CY, de Pater CJ. Numerical implementation of displacement discontinuity method and its application in hydraulic fracturing. Comput Methods Appl Mech Eng. 2001;191:745-60.

[7] Hossain MM, Rahman MK. Numerical simulation of complex fracture growth during tight reservoir stimulation by hydraulic fracturing. J Pet Sci Eng. 2008;60:86-104.

[8] Kassir M, Sih G. Three-dimensional stress distribution around an elliptical crack under arbitrary loadings. J Appl Mech. 1966;33:601-11.

[9] Reyes O, Einstein H. Failure mechanisms of fractured rock-a fracture coalescence model. 7th International Society for Rock Mechanics Congress1991.

[10] Dyskin AV, Sahouryeh E, Jewell RJ, Joer H, Ustinov KB. Influence of shape and locations of initial 3-D cracks on their growth in uniaxial compression. Eng Fract Mech. 2003;70:2115-36.

[11] Yang S-Q, Jing H-W. Strength failure and crack coalescence behavior of brittle sandstone samples containing a single fissure under uniaxial compression. Int J Fract. 2011;168:227-50.

[12] Germanovich LN, Salganik RL, Dyskin AV, Lee KK. Mechanisms of brittle fracture of rock with pre-existing cracks in compression. Pure Appl Geophys. 1994;143:117-49.

[13] Erdogan F, Sih GC. On the crack extension in plates under plane loading and transverse Shear. J Basic Eng. 1963;85:519-25.

[14] Wawrzynek P, Carter B, Ingraffea A. Advances in simulation of arbitrary 3D crack growth using FRANC3D NG. 12th International Conference on Fracture. Ottawa2009.

[15] Rooke DP, Cartwright DJ. Compendium of stress intensity factors1976.

[16] Tada H, Paris P, Irwin G. The stress analysis of cracks handbook. 3 ed: New York: ASME Press; 2000.

[17] Young WC, Budynas RG. Roark's formulas for stress and strain. New York: McGraw-Hill; 2002.

[18] Sih GC, Liebowitz H. Mathematical theories of brittle fracture. In: Liebowitz H, editor. Fracture An Advanced Treatise: Academic Press, Inc.; 1968. p. 128-51.

[19] Wawrzynek P, Carter B, Banks-Sills L. The M-Integral for computing stress intensity factors in generally anisotropic materials: National Aeronautics and Space Administration, Marshall Space Flight Center; 2005.

[20] Tsuji, Iwase, Ando. An investigation into the location of crack initiation sites in alumina, polycarbonate and mild steel. Fatigue & Fracture of Engineering Materials & Structures. 1999;22:509-17.

Paper 2

Statement of Authorship

Title of Paper	Fracture mechanics approximation to predict the breakdown pressure of a rock material using the theory of critical distances
Publication Status	☐ Published ☑ Accepted for Publication ☐ Submitted for Publication ☐ Unpublished and Unsubmitted w ork w ritten in manuscript style
Publication Details	

Principal Author

Name of Principal Author (Candidate)	Adam Karl Schwartzkopff
Contribution to the Paper	Developed theory, conducted experiments, performed numerical analyses, wrote manuscript and acted as corresponding author.
Overall percentage (%)	90%
Certification:	This paper reports on original research I conducted during the period of my Higher Degree by Research candidature and is not subject to any obligations or contractual agreements with a third party that would constrain its inclusion in this thesis. I am the primary author of this paper.
Signature	Date Friday 19 August 2016

Co-Author Contributions

By signing the Statement of Authorship, each author certifies that:

i. the candidate's stated contribution to the publication is accurate (as detailed above);
ii. permission is granted for the candidate in include the publication in the thesis; and
iii. the sum of all co-author contributions is equal to 100% less the candidate's stated contribution.

Name of Co-Author	Nouné Sophie Melkoumian
Contribution to the Paper	Supervised development of work and reviewed manuscript.
Signature	Date Friday 19 August 2016

Name of Co-Author	Chaoshui Xu
Contribution to the Paper	Supervised development of work and reviewed manuscript.
Signature	Date Friday 19 August 2016

Fracture mechanics approximation to predict the breakdown pressure of a rock material using the theory of critical distances

Adam K. Schwartzkopff [a]
Nouné S. Melkoumian [a]
Chaoshui Xu [a]

[a] School of Civil, Environmental and Mining Engineering, Faculty of Engineering, Computer and Mathematical Sciences, The University of Adelaide, SA 5005 Australia

Abstract

The breakdown pressure is an important parameter that influences the hydraulic fracturing process of the rock. This paper presents a new approach for the prediction of the breakdown pressure in hydraulic fracturing based on the theory of critical distances. The proposed method of analysis assumes that a pressurised crack is formed at a critical distance into the material prior to the unstable propagation. The breakdown pressure is calculated using an analytical approximation of the mode I stress intensity factor for this pressurised crack. A series of hydraulic fracturing experiments were conducted and the test results were compared with those predicted from the proposed method of analysis. The approximation aligns with these test results as well as with published results from independent hydraulic fracturing experiments.

Keywords: hydraulic fracturing, breakdown pressure, critical distance, fracture mechanics

Nomenclature

σ_H	maximum horizontal principal stress (Pa)
σ_h	minimum horizontal principal stress (Pa)
σ_n	normal stress (Pa)
σ_t	tensile strength of the material (Pa)
σ_v	vertical principal stress (Pa)
a	crack radius (m)
a_{Ic}	critical distance (m)
A	poro-elastic constant
C_b	bulk compressibility (Pa)
C_r	matrix compressibility (Pa)
F	shape factor
K_I	mode I stress intensity factor (MPa$\sqrt{\text{m}}$)
K_{Ic}	mode I fracture toughness (MPa$\sqrt{\text{m}}$)
p_0	pore pressure (Pa)
P_f	breakdown pressure (Pa)
P_i	Initiation pressure (Pa)
R	radius of the borehole (m)
LEFM	linear elastic fracture mechanics

1 Introduction

Hydraulic fracturing is a mechanical process whereby pressurised fluid causes unstable fracture propagations into a rock mass. These generated fractures alter the properties of the rock mass, including its permeability, strength and anisotropy. Hydraulic fracturing can occur by natural processes. However, since the early 1950s this mechanical process has been utilised by the hydrocarbon extraction, geothermal, mining and other related industries to take advantage of these altered rock mass properties [1]. Specifically, enhanced geothermal systems and unconventional gas reservoirs rely on hydraulic fracturing to increase the permeability of the reservoir by producing new fractures and/or stimulating pre-existing discontinuities. In such systems, fractures act as main fluid/gas conduits and heat exchange surfaces.

In addition, hydraulic fracturing can be used for rock stress estimation. The apparatus needed for this in-situ stress estimation, in the field, requires; surface equipment, straddle packer, high-pressure tubing, drill pipe, or hose, pressure gages, pressure transducers and a flow meter, pressure generators and recording equipment. One item of note is the straddle packer, which seals the borehole test interval. The straddle packer is two inflatable rubber packers, spaced apart at a distance equal to at least six time the borehole diameter. These two packers are connected mechanically as well as hydraulically to create one unit (i.e. the straddle packer) [2]. This specified distance between the two inflatable rubber packers is used for rock stress estimation. However, this chosen length is arbitrary, for those hydraulic fracturing operations that do not choose to estimate the rock stress conditions. Therefore, there are two different predominate features of the hydraulic fracturing experiments performed in this study compared to hydraulic fracturing tests for rock stress estimation; this pressurisation length is small compared with the diameter of the borehole, and stainless steel tubing attached to the borehole wall via epoxy is used to mimic the straddle packer.

To locate effective hydraulic fracturing treatment zones and create an optimal operational fracture network within the rock mass, it is important to predict the maximum internal pressure that the material can withstand, i.e. the breakdown pressure. This breakdown pressure is an important initial parameter that affects the fracturing of the rock mass and hence the enhanced permeability of the system. However, the fracturing process is complex as it depends on various factors including the injection rate, fluid properties, borehole radius, in-situ stress condition, and the rock (mass) properties. Currently there are several theories developed for the prediction of breakdown pressures with varying degrees of success [3-5] but this remains an active research area in hydraulic fracturing.

The in-situ stress condition of the rock mass is one factor that influences the breakdown pressures of an intact material. Generally, one remote compressive principal stress direction is defined (and assumed) as vertical; therefore, the other two remote principal stresses are horizontal. The vertical and horizontal compressive principal stress magnitudes can be different, therefore, they are denoted the vertical principal stress σ_v, the minor horizontal principal stress σ_h, and the major horizontal principal stress σ_H. These remote compressive principal stresses in the rock mass are disturbed by the presence of the borehole and the pressurised fluid. This perturbed stress field near the borehole is usually utilised to estimate the breakdown pressure expected. It is suggested, this concept may be used for an undamaged rock; however, if the material forms any crack or cracks, the elastic spatial stress tensor for a pressurised borehole will not be valid. The elastic spatial stress tensor can be used to estimate the onset of crack initiation. However, once a crack forms, it is suggested that this damaging process must be considered when predicting the breakdown pressure. The damage process during hydraulic fracturing will cause a fracture to form perpendicular to the minor principal stress direction (or the lowest principal stress direction). Although the presence of cracks may cause the spatial stress field to be different compared with pressurised intact rock using fluid pressure in a section of a borehole; this concept of an intact (undamaged) rock is commonly used.

Therefore, one of the most frequently adapted theories, to estimate the breakdown pressure, uses this elastic spatial stress tensor for a pressurised borehole [6, 7]. This model calculates the breakdown pressure P_f, for a vertical borehole associated with producing a vertically orientated fracture in a normal faulting stress regime $(\sigma_v \geq \sigma_H \geq \sigma_h)$ by the following [5]:

$$P_f = \sigma_t + 3\sigma_h - \sigma_H \tag{1}$$

where σ_t is the tensile strength of the rock, σ_h and σ_H are the remote minor and major horizontal stresses. For this simplified case of borehole axis aligned vertically, the tangential stress on the wall of the borehole is not affected by the remote vertical principal stress σ_v, as is evident from Eq. (1). Therefore, only for these conditions and using this theory, the principal stress σ_v, is not considered to influence the breakdown pressure of a vertical borehole. When the in-situ pore pressure is considered, Eq. (1) becomes:

$$P_f = \sigma_t + 3\sigma_h - \sigma_H - p_0 \tag{2}$$

This conventional model predicts the failure of the rock to take place on the walls of the pressurised borehole. However, when the apparent tensile strength is back calculated using this expression, the value is found to be greater than that measured directly from tensile strength tests [8]. In addition, this theory cannot account for the reduction in breakdown pressure when the borehole diameter is increased [3].

Ito and Hayashi [3] and Ito [8] introduced a theory to predict the initiation of a fracture due to hydraulic pressure where they assumed the initiation occurs when the maximum effective tensile stress reaches the tensile strength of the rock at a critical distance into the rock. (See Fig. 1 for a graphical representation of the difference between initiation pressure and breakdown pressure).

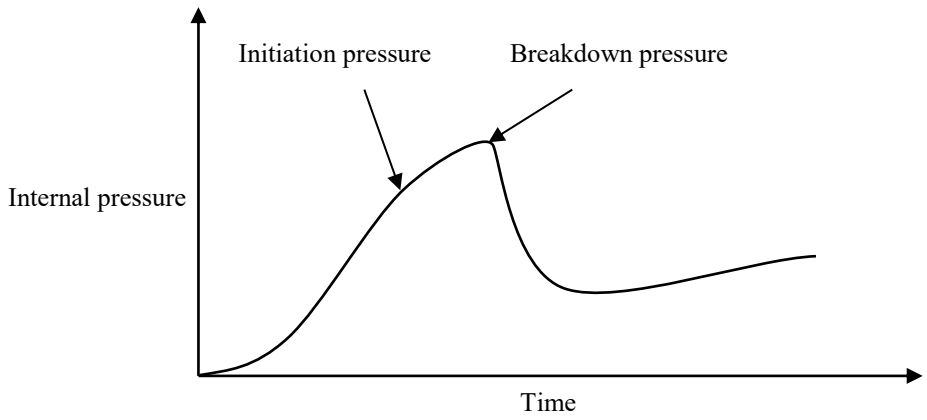

Fig. 1 Conceptual internal pressure versus time graph, indicating the difference between initiation pressure and breakdown pressure

Therefore, this initiation pressure is lower than the breakdown pressure. The degree of non-linear behaviour in the pressure versus time or cumulative volume near the peak stress determines the closeness of the initiation pressure with the breakdown pressure. If there is a substantial amount of non-linear behaviour, the initiation pressure may differ significantly to the breakdown pressure. Haimson and Fairhurst [4] derived an equation to convert between the initiation pressure and the breakdown pressure:

$$P_f = \left[2 - A\left(\frac{1-2\upsilon}{1-\upsilon}\right)\right] P_i \tag{3}$$

where A is the poro-elastic constant and υ is Poisson's ratio. This poro-elastic constant ranges between 0 and 1 and is calculated by the following expression [8]:

$$A = 1 - \frac{C_r}{C_b} \tag{4}$$

where C_r is the material matrix compressibility and C_b is the material bulk compressibility.

Ito [8] predicts lower and upper bound values for the initiation pressure. They express this upper limit as the following, corresponding to very high injection rate approaching ∞ MPa per second:

$$P_i = \left(1+\frac{a_{Ic}}{R}\right)^2 \left\{\sigma_t - \left[\frac{\sigma_H+\sigma_h}{2}\left(1+\frac{R^2}{(R+a_{Ic})^2}\right) - \frac{\sigma_H-\sigma_h}{2}\left(1+3\frac{R^4}{(R+a_{Ic})^4}\right)\right]\right\} \tag{5}$$

In addition, they define the lower limit as the subsequent expression, corresponding to a very slow injection rate approaching 0 MPa per second:

$$P_i = \frac{\sigma_t - \left[\frac{\sigma_H+\sigma_h}{2}\left(1+\frac{R^2}{(R+a_{Ic})^2}\right) - \frac{\sigma_H-\sigma_h}{2}\left(1+3\frac{R^4}{(R+a_{Ic})^4}\right)\right]}{\left(1-\frac{A}{2}\right)\left\{1+\frac{1}{(1+a_{Ic}/R)^2}\right\}} \tag{6}$$

where R is the borehole radius and a_{Ic} is the critical distance. A numerical approach is needed to derive the predicted initiation pressures between these ranges, based on the pressurisation rate of the experiment.

In this current study, the theory developed by Ito and Hayashi [3] and Ito [8] is extended to overcome the limitation that the previous theory predicts the initiation pressure but not the breakdown pressure directly. An analytical expression is derived using the method described in this paper, and the lower and upper bound analytical expressions from Ito [8] are used to compare the results. Hydraulic fracturing experiments were also performed and evaluated by the derived analytical expression. The close alignment of the derived expression to experimental results highlights its significance. Note, our experiments were conducted under constant flow rate, whereby the pressurisation rate is not constant (see Appendix B).

In addition, it has been hypothesized in other experimental studies that before the breakdown pressure is reached, a stable crack develops [9, 10]. For example, Morita *et al.* [10] provided evidence that borehole breakdown occurred when the initiated fracture became unstable after significant growth (with 7.6 mm to 76.2 mm in length). Therefore, this observation of a stable crack is used as a concept in this study. In addition, this assumed stable crack is formed perpendicular to the minor principal stress direction, which is consistent to the findings in an experimental study by Hubbert and Willis [11]. To support further the current analysis, Guo *et al.* [5] found through statistical analysis of their

experimental results that breakdown pressures have a stronger relationship with the magnitude of the associated minor principal stress compared with the tensile stress at the wall of the borehole. It has been shown that the theory of critical distances [12] can predict accurately the tensile failure (the maximum stress) of brittle material with notches of various sizes.

It is notable that for different rock types the critical distance values vary significantly from each other. For example, even for the same rock type (andesite) in the study by Ito and Hayashi [3], the critical distance ranges from 1.54 mm for Honkomatsu andesite to 3.39 mm for Kofu andesite. This means measurements of the fracture toughness and tensile strength are fundamental in determining the critical distance (see discussion in Section 4.1), and hence the breakdown pressure for each rock type. The difference in critical distance values or process zone magnitudes for rocks can be related, experimentally, to material properties, such as the grain size and the texture of the rock material. Therefore, the size of these inelastic regions in rock under load can be quantified by the critical distance values. The size of the process zone, immediately prior to the maximum stress the material can withhold, is not a constant. However, this size is often of the same order of magnitude as the function $\left(K_{Ic}/\sigma_t\right)^2$ [13, 14], whereby the fracture toughness value is K_{Ic}, and σ_t is the tensile strength value obtained from experimental results. Therefore, this function can be used as a scaling parameter for defining the extent of the process zone. In addition, this expression is proportional to the critical distance value used in this study. The process zone is an area of high stresses near the crack tip, whereby inelastic material deformation occurs [12]. Hence, the concept of a critical distance value, which is used in this study, attempts to quantify this mechanism of inelastic behaviour. Since the grain size and texture of the rock varies with each sample and rock type, this process zone or critical distance value in this study, must be measured from experiments and used as a parameter in the theory, as discussed in this investigation.

Therefore, in the current study of breakdown pressure prediction for a pressurised borehole, a new theory is proposed based on the assumption that an approximately circular stable pressurised crack perpendicular to the minor principal stress direction is produced during hydraulic fracturing stimulations. Hence, the failure of this crack can be determined using linear elastic fracture mechanics (LEFM) if the critical distance, which is a material constant, and the borehole radius are known. The description of the theory and its experimental validation are given below.

2 Problem formulation

This work considers a section of a pressurised borehole with length h, which is close to zero thickness, therefore small compared with its overall length in the direction of a principal stress. This section of borehole is pressurised by the fluid pressure P. The three principal stresses: σ_H, σ_h and σ_v are orientated along the x, y and z axes, respectively (Fig. 2).

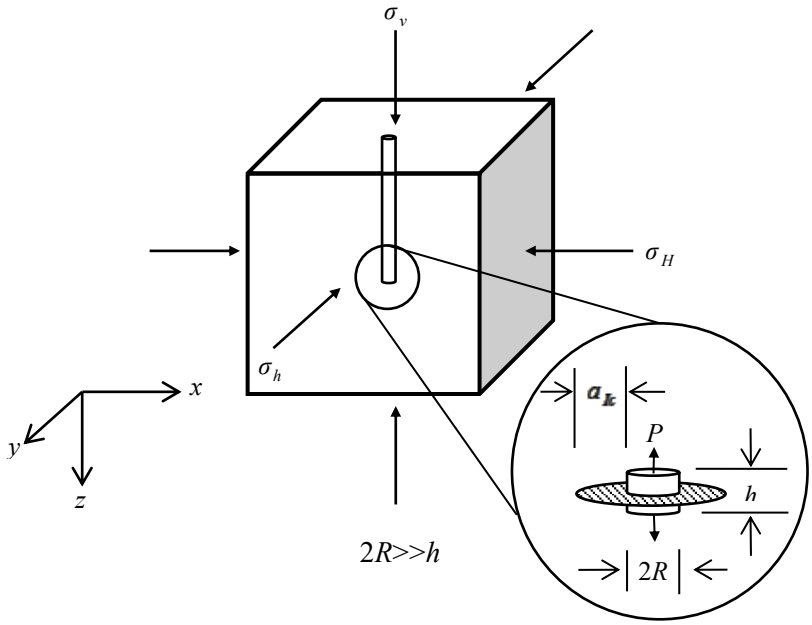

Fig. 2 Problem formulation

3 Material and methods

This study used experiments to investigate the breakdown pressure values of this configuration (see Fig. 2), which are detailed and presented in this section. Both the properties and methods related to the material tested and procedure undertaken for the hydraulic fracturing experiments are described below.

3.1 Material

The artificial rock material used in this study was chosen such that it would be homogeneous, isotropic, and brittle with mechanical properties reproducible and comparable to the type of rocks to be studied. The rocks subjected to hydraulic fracturing in general have low permeability [15-18]. For example, engineered geothermal systems are generally located in granite basements with overlain sediments [15, 19], whereas unconventional gas reservoirs are in general located in shales or mudstones [20]. In this study, high strength concrete with mechanical properties similar to granite was used.

3.1.1 Mechanical properties of granite

The ranges of the mechanical properties of granite are listed in Table 1 from the literature [21-32]. These values were used as a guide to design the mechanical properties of the artificial rock, i.e. the concrete used in this study. In construction of Table 1, the minimum number of values corresponds to the summation of the following:

- if only the mean value is reported in the referred publication, then this is counted as one value
- if both the mean and the standard deviation are reported then this is counted as three values (corresponding to the mean minus the standard deviation, the mean, and the mean plus the standard deviation)
- finally, if all the experimental data are given then all values are used

There is some variability in material properties, since all granites have different geological compositions.

Table 1 Range of granite mechanical properties

Material characteristic	**Minimum reported value**	**Maximum reported value**	**Minimum number of values**	**References**
Elastic modulus (GPa)	18	109	17	Alejano *et al.* [21], Arzúa and Alejano [22], Backers *et al.* [23], Bell [24], and Stimpson [25]
Poisson's ratio	0.16	0.19	4	Arzúa and Alejano [22] and Backers *et al.* [23]
Uniaxial compressive strength (MPa)	64	321	124	Arzúa and Alejano [22], Bell [24], and Yesiloglu-Gultekin *et al.* [26]
Density (kg/m^3)	2580	2670	8	Arzúa and Alejano [22], Sano *et al.* [27], and Sundberg *et al.* [28]
Tensile strength (MPa)	5.13	16.40	78	Arzúa and Alejano [22], and Yesiloglu-Gultekin *et al.* [26]
Cohesion (MPa)	12.42	19.39	3	Arzúa and Alejano [22]
Internal angle of friction (°)	54.9	59.5	3	Arzúa and Alejano [22]
Mode I fracture toughness (MPa$\sqrt{\text{m}}$)	0.71	2.20	74	Nasseri and Mohanty [29], and Xu [30]
Mode II fracture toughness (MPa$\sqrt{\text{m}}$)*	2.2	2.2	1	Backers *et al.* [23]
Porosity (%)	0.1	1.0	5	Nur and Byerlee [32]
Friction coefficient	0.49	0.85	5	Alejano *et al.* [21], Arzúa and Alejano [22], and Byerlee [33]
Permeability (m^2)	3.36×10^{-21}	1.73×10^{-19}	33	Brace *et al.* [31]

*At zero confining pressure

3.1.2 Methods to produce the artificial rock

Two solid concrete blocks were created from two separate mixtures using the mass ratios of the base materials (see Table 2) for testing the mechanical properties. The purpose for

two separate mixtures was to test the consistency of the mechanical properties. The dimensions of the blocks were 450 mm × 450 mm × 200 mm.

Table 2 Materials and mass values for the artificial rock mixture

Materials	Mass ratios
Sulphate resisting cement	1
Sand 60G	0.5
Sand 30/60	0.5
Silica fume	0.266
Water	0.165
Super plasticizer (ViscoCrete®10)	0.06
Total	2.491

The following procedures (adapted from Guo *et al.* [34]), in order of completion, were used to ensure the production of high strength concrete:

1. Line the inside walls of the wooden formwork with oil
2. Fix the formwork on a vibrating table
3. Mix the sulphate resisting cement, Sand 60G, Sand 30/60 and silica fume for an average of 15 minutes to achieve homogeneous distribution of material
4. While the sand and gypsum are being mixed, dissolve the super-plasticizer in water at room temperature
5. Add the super-plasticizer solution to the sand and gypsum mixture and mix for a further 50 minutes until the mixture is consistent
6. Fill the wooden formwork with the mixture
7. Compact the mixture by vibration
8. Systematically poke a sharp steel rod into the mixture to remove air pockets
9. Remove the specimen from the vibrating table after completely filling the wooden formwork and leave it to set for 12 hours
10. While in the formwork, cover the specimen with wet hessian for an average of 2 days
11. Remove the material from the mould and let the specimen cure at 46±2 degrees Celsius at 30% relative humidity for 28 days
12. Once cured remove the material from the fog room and store it at room temperature for 28 days
13. Cut and grind the material blocks into the desired shape (7 days)
14. Dry specimens in oven at 100 degrees Celsius for 12 hours

The reason for storing the material outside the fog room at room temperature for a further 28 days was to ensure there was minimal change in the strength and the mechanical characteristics, during the period of testing, which lasted 5 days.

3.1.3 Material properties of the artificial rock

To test the material properties of the artificial rock, 76 sets of specimens were created. All the specimens were prepared and tested in accordance with the International Society of Rock Mechanics (ISRM) specifications for each method or a suitable published method in the absence of an ISRM suggested method (see Table 3). The material characteristics of the artificial rock are summarized in Table 4.

Table 3 Methods used to measure the material properties of the concrete

Parameter	Reference
Elastic modulus (GPa)	Bieniawski and Bernede [35]
Poisson's ratio	
Uniaxial compressive strength (MPa)	
Density (kg/m^3)	Described in the manuscript
Tensile strength (MPa)	[36]
Cohesion (MPa)	Kovari *et al.* [37]
Internal angle of friction (°)	
Mode I fracture toughness (MPa$\sqrt{m}$)	Fowell [38]
Mode II fracture toughness (MPa$\sqrt{m}$)	Backers and Stephansson [39]
Friction coefficient	Alejano *et al.* [21]
Porosity (%)	Described in the manuscript
Permeability (m^2)	Described in the manuscript

Twelve cylindrical specimens were used to determine the deformability parameters such as Poisson's ratio and elastic modulus, and six of those specimens were taken to the ultimate load to determine the uniaxial compressive strength of the material.

The average elastic modulus is calculated and is divided by the slope of diametric curve to calculate the Poisson's ratio. The average diameter was 63.3$\pm$0.04 mm and the average height was 175.0$\pm$0.09 mm, therefore the height to diameter ratio was 2.76, which was between the suggested ratio of 2.5 to 3.0. Strain gauges were used for the six specimens taken to their ultimate load, and for the other six specimens extensometers were used (see Fig. 3). One specimen from each block i.e., two specimens were used to determine the relative error between the measurement methods. The average error between these two methods was 0.0014% strain, which was considered negligible.

Fig. 3 Cylindrical specimen before deformability testing commenced with strain gauges and extensometers

The tensile strength was determined from 24 Brazilian disc specimens with an average diameter of 106.5±0.03 mm and a thickness of 35.0±0.1 mm. These specimens were taken to failure (see Fig. 4 for test setup).

Fig. 4 Brazilian disc specimen before indirect tensile testing commenced

The density was determined using the un-notched specimens (Brazilian discs, cylinders for the deformability tests and triaxial strength specimens). To obtain the average density, the total weight of all these specimens was divided by their total volume.

Mode I fracture toughness was obtained from 14 cracked chevron notched Brazilian disc specimens of similar dimensions to the Brazilian disc test specimens (see Fig. 5 for the loading configuration).

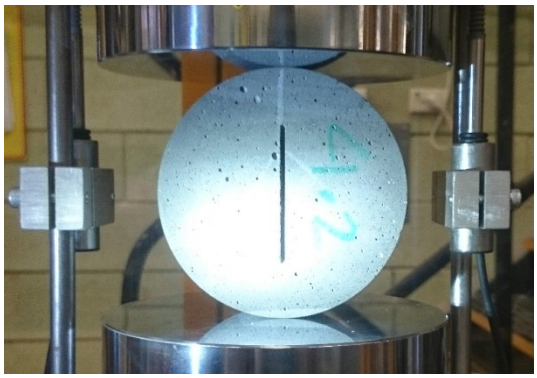

Fig. 5 Cracked chevron notched Brazilian disc specimen before mode I fracture toughness test commenced

The disks averaged a thickness of 35.0±0.04 mm and an average diameter of 106.4±0.10 mm. The half-length of the maximum part of the slot (a_1) was 29.5±0.07 mm and the minimum half-length of the slot (a_0) was 12.07±0.08 mm (see Fig. 6).

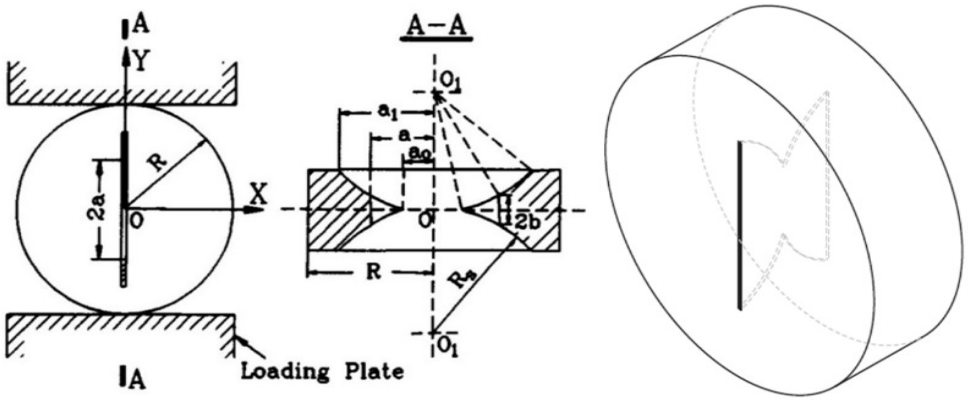

Fig. 6 The cracked chevron Brazilian disc specimen geometry with recommended test fixture (from Fowell [34])

Mode II fracture toughness was obtained by performing 12 punch-through shear tests using notched cylindrical specimens (see Fig. 7 for the specimen setup).

Fig. 7 Specimen setup before a punch through shear test was commenced

The punch through shear test specimens were taken to their ultimate loads (see Fig. 8 for the specimen geometry).

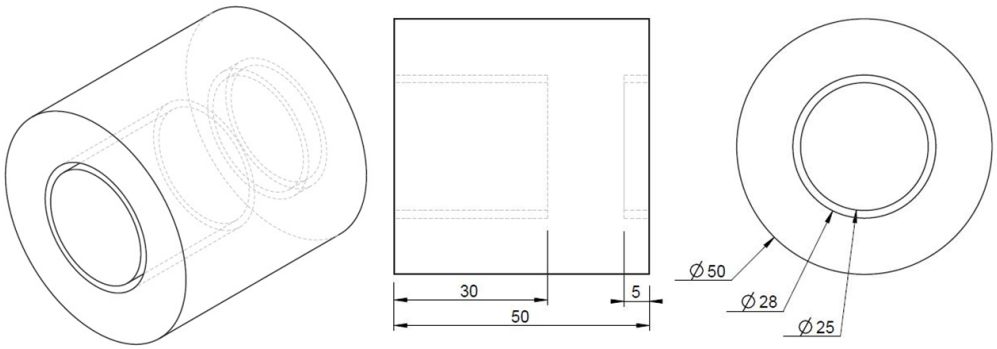

Fig. 8 Specimen geometry and dimensions of the punch-through shear experiment (adapted from Backers and Stephansson [39])

Four rectangular specimens (100 mm × 100 mm × 40 mm) were created to determine the friction coefficient. The static friction coefficient was determined from the critical angle at which the specimens slid over each other (see Fig. 9). The inclined angle was increased incrementally from about 20°. The tangent of these angles determined the static friction coefficient.

Fig. 9 Tilt testing table

Triaxial strength tests were performed on eight cylindrical specimens (126.9±0.1 mm in length and 63.3±0.03 mm in diameter), and were tested under confining pressure (5, 10, 15 and 20 MPa) using a Hoek cell (see Fig. 10). The Mohr-Coulomb parameters, cohesion, and internal angle of friction were thus obtained.

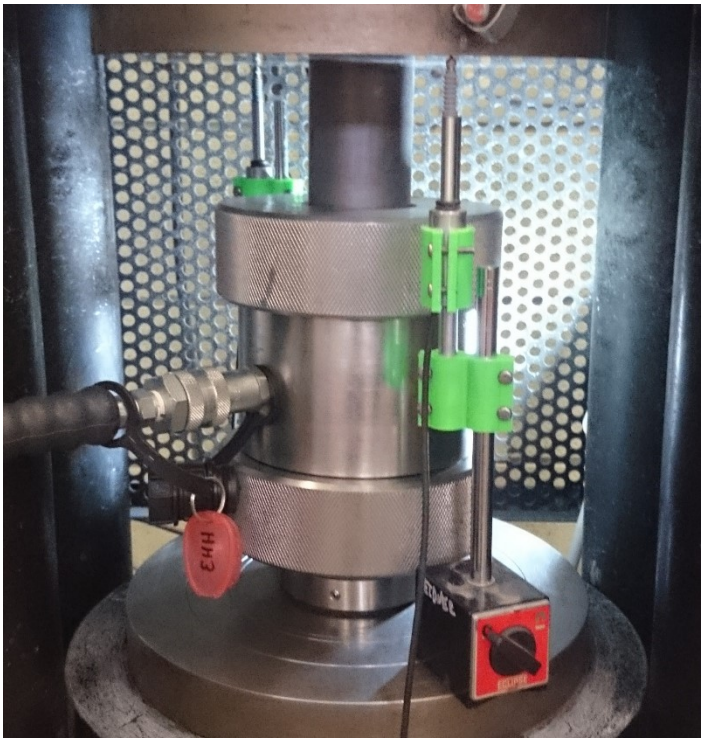

Fig. 10 Triaxial strength test setup

Permeability tests were performed on four machined specimens. Sample 1 from block 1 was placed under 6.585 MPa of differential water pressure and produced no recordable flow. It is concluded that the material is impermeable to fluid. One sample was exposed to a differential pressure of 1.243 MPa of Helium gas; and produced no recordable flow of gas (see Fig. 11). Similarly, it was concluded that the material is impermeable to gas.

The lowest permeability value that can be measured using this equipment is 9.9×10^{-19} m^2; hence, the actual permeability of the material would be below this value. When this material is hydraulically fractured, it can be assumed that the water will not permeate, or only a negligible quantity will permeate into the material matrix. In addition, the porosity was measured using a helium porosimeter on three samples. The measured porosity was only about 1% higher than granite.

Fig. 11 Helium gas permeability test

As shown in Table 4, key material characteristics are closely aligned with those of granite:

Table 4 Summary of the material characteristics

Material characteristic	Value	Standard error value	Standard error percentage	Number of values	Minimum reported value for granite	Maximum reported value for granite
Elastic modulus (GPa)	46.32	1.48	3.2%	12	18	109
Poisson's ratio	0.217	0.017	7.8%	12	0.16	0.19
Uniaxial compressive strength (MPa)	183.6	3.9	2.1%	6	64	321
Density (kg/m^3)	2313	24	1.0%	44	2580	2670

Material characteristic	Value	Standard error value	Standard error percentage	Number of values	Minimum reported value for granite	Maximum reported value for granite
Tensile strength (MPa)	6.31	0.69	10.9%	24	5.13	16.40
Cohesion (MPa)	44.28	3.53	8.0%	8	12.42	19.39
Internal angle of friction (°)	41.3	3.7	8.9%	8	54.91	59.52
Mode I fracture toughness ($MPa\sqrt{m}$)	1.18	0.05	3.9%	14	0.71	2.20
Mode II fracture toughness ($MPa\sqrt{m}$)	2.35	0.17	7.2%	12	2.2	2.2
Porosity (%)	2.07	0.53	25.9%	3	0.1	1.0
Friction coefficient	0.572	0.049	8.5%	20	0.49	0.85
Permeability (m^2)	$<9.9\times10^{-19}$	NA	NA	4	3.36×10^{-21}	1.73×10^{-19}

Such a comprehensive measurement of the material properties will provide a baseline of comparison for future research if an artificial rock, such as this, needs to be used. For this study, tensile strength and mode I fracture toughness are the two most important properties used in the proposed theory.

There were some differences however, in material properties between the high strength concrete used and granite. This artificial rock had cohesion values that were about 2.3 to 3.6 times greater than granite, and had a relatively low friction coefficient when compared to granitic rock. Since, both the cohesion and friction coefficient are important when considering the material under shearing conditions, it is suggested that these parameters did not have a significant impact on the applicability of the hydraulic fracturing results, because hydraulic fracturing breaks the rock in tension. The artificial rock had relatively low density compared to granite. The density would have limited influence on the results, since the hydraulic fracturing process can be considered quasi-static because the fluid pressure increase is incremental. The density would have more influence if the process was dynamic i.e. the fluid pressure was instantly increased to the breakdown pressure. Even if this were the case, the density would only slightly affect the volume of injected fluid. Since the same process governs the hydraulic fracturing development, it is expected that the density value would not have a significant effect on the breakdown pressure value. The porosity of the artificial rock was approximately 2.1 to 20.7 times greater than recorded values of granitic rock. This parameter could have an

impact on the applicability of the hydraulic fracturing results to granite. Since, during the hydraulic fracturing process the breaking of the material could be assisted by the higher porosity values. If a crack or cracks are generated before the breakdown of the material this higher porosity would link pores in the material easier than material with lower porosity. Hence, this could create a larger fracture process zone when considering an increase porosity value. This fracture process zone could however, be captured by the critical distance value (where the critical distance is an analogue to the fracture process zone). In other words, the influence of porosity on breakdown pressure may be captured by using this critical distance value, since it is expected that an increase in porosity may increase the critical distance parameter. In context with hydraulic fracturing, the differences in properties between these two materials (granite and the artificial rock) can be considered small. Therefore, this concrete is comparable to granite under hydraulic fracturing conditions.

3.2 Hydraulic fracturing experimental method

To manufacture specimens with the required geometry, a series of components were produced from acrylonitrile butadiene styrene (ABS) using a three dimensional printer (see Fig. 12). These components consisted of a base and a cylindrical extrusion. A plastic cylinder was positioned around the base of these components, which created a void in the mortar mixture. The mixture mass ratios and procedure were as described in Section 3.1.2. The only difference was that these specimens were placed in an acetone bath for four weeks to dissolve the excess cylindrical extrusion, instead of leaving in a dry location at room temperature for 28 days. To place the bottom of the borehole void in approximately the middle of the specimen and to have both specimen ends flat and square, the specimen required extra material on each end. Therefore, 2 mm was added to the length of the cylindrical specimen, with 1 mm at each end. With this extra material and the cylindrical extrusion length being 64.5 mm for the borehole, this meant the borehole left in the material would be approximately 63.5 mm after 1 mm was taken off the ends via the grinding process. Prior to placing these specimens in the acetone bath, the cylindrical extrusion was drilled out using a 6.30 mm diameter drill bit.

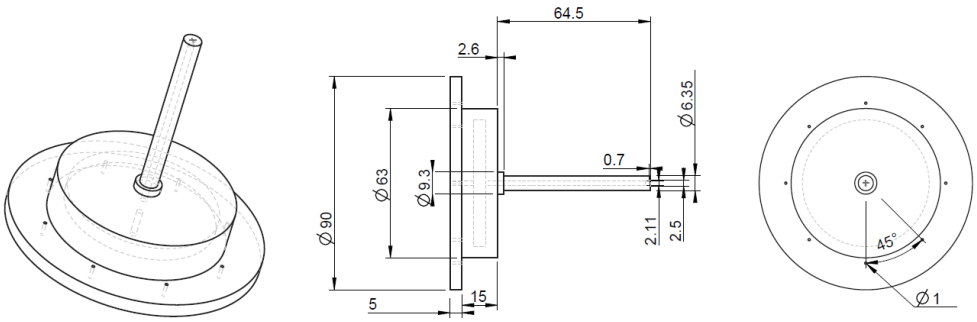

Fig. 12 Mould design

The designed specimen geometry is shown in Fig. 13. The indent was designed as a well for the epoxy (Sika Anchorfix®-3+).

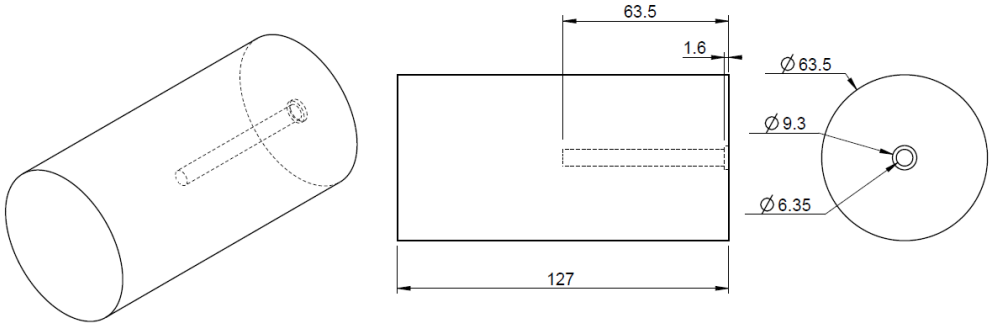

Fig. 13 Hydraulic fracturing specimen

A platen with an internal conduit and threaded system was used to transfer hydraulic pressure into the specimen (see Fig. 14).

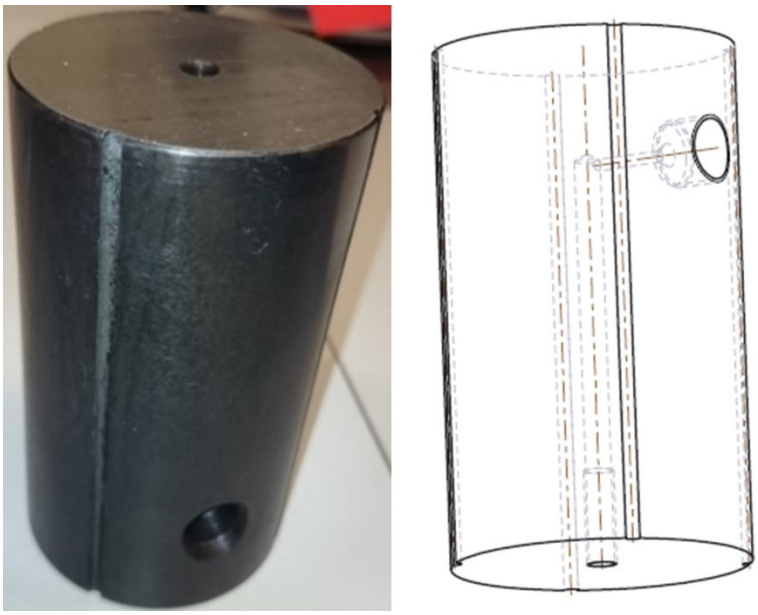

Fig. 14 Axial platen with internal conduit to transfer fluid pressure into the specimen

An injection tube (see Fig. 15 for its dimensions) was coated in the epoxy and then placed into specimen boreholes. This was done approximately 14 hours prior to testing to allow the epoxy to cure.

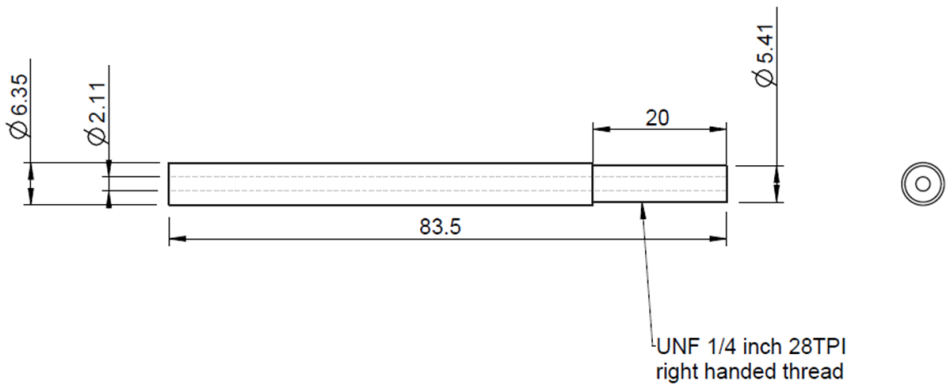

Fig. 15 Injection tube

Once the injection tube had cured in position, the 20 mm of exposed thread was wrapped in high-density polytetrafluoroethylene (PTFE) thread tape designed to hold pressures of up to 68.9 MPa. Dental paste was applied to the top surface with the injection tube. The axial platen was then hand screwed onto this injection tube until the faces met, before the dental paste hardened (see Fig. 16). The dental paste sealed the platen and specimen interface and filled any small pores in the surface of the specimen to ensure uniform load transfer.

Fig. 16 Axial platen and specimen mated

The fluid used for these experiments was coloured distilled water, where 40 mL of black food colouring was added to 4 litres of distilled water (a volumetric ratio of 1 to 100). The black food colouring was used to make the fluid more noticeable if there was a leak and to trace the hydraulic fractures.

The testing procedure was as follows:

1. Using a syringe, the internal cavity inside the platen and the specimen was filled with fluid (coloured distilled water) prior to connecting the load platen to a Teledyne Isco 65HP High Pressure syringe pump.
2. When connecting the syringe pump line to the load platen, the pump was set at a constant flow rate of 1 mL per minute and then hand tightened to reduce the amount of air trapped during the connection process. Once the connection was tightened with a spanner the syringe pump was stopped immediately.
3. A spherical seat was aligned on the top surface of the load platen prior to axial loading.
4. The data acquisition server was set to record when the axial load and confining pressures were applied (see Fig. 17). The axial load was then increased to approximately 1.0 kN. The Hoek cell was hand pumped to 0.5 MPa and then the pressure maintainer was enabled. The loading rate was 0.03 MPa per second to reach the desired stress level within 5 to 10 minutes. The axial load and confining pressure were increased until the desired lower value was reached, this stress was then maintained, and the other was increased until its desired value was reached. If the axial stress was larger than the confining pressure, then the Hoek cell pressure maintainer tracked the axial stress until the maximum confining pressure target value was reached, where the axial stress was determined by the load divided by the average cross-section. If the confining pressure target was larger than the axial stress target, then approximately 1.0 kN before the maximum load was reached the pressure maintainer was changed to the pre-set rate of 0.03 MPa per second.
5. Once the Hoek cell and the axial stress reached their target values, the distilled water was pumped into the specimen at a constant flow rate of 5 mL per minute. This was chosen to produce an average pressurisation rate of approximately 1 MPa per second. The cumulative volume and pressure from the syringe pump were recorded during each test, in addition to the external stress conditions.

Fig. 17 Hydraulic fracturing setup

Since reverse faulting stress conditions, where the vertical stress is the minor principal stress component, are prominent in Australia [40], this stress regime is the focus of this study. There were 26 tests performed under different external stress configurations (see Table 5). These configurations follow a grid design to remove bias when determining the influence of the external stresses on the breakdown pressure. There are at least two experiments per stress configuration conducted to improve the reliability of measurements.

Table 5 Experimental design

Number of tests per configuration		**Confining pressure (MPa)**		
		5	**10**	**15**
Axial pressure (MPa)	**0**	3	3	3
	5	3	3	3
	10	2	2	4

4 Theory

The aim of this research is to study the internal pressure required to cause unstable hydraulic fracturing of a pressurised borehole section. It is assumed that there are no time dependent effects, i.e. the failure stress is independent from the rate of loading. In our experiments, a constant flow rate of 5 mL per minute was applied which is supported by

a previous study showing the breakdown pressure is independent of the loading rate if the flow rate in constant [9].

4.1 Fracture mechanics approach using the theory of critical distances

Ito and Hayashi [3] showed that during the hydraulic fracturing process of two types of andesite (rock), a stable fracture, with length equal to a critical distance, is initiated from the borehole wall. For this study, it is further hypothesized that a stable pressurised circular crack perpendicular to the minor principal stress direction will form around the borehole before the breakdown pressure is reached. This stable pressurised crack is proposed to form into the rock material. In this case, the section length $h,$ is close to zero, and therefore is small with respect to the diameter of the borehole (Fig 2). This section of pressurised borehole acts as a notch and the crack initiates from this void. In this case, the radius of the borehole provides the maximum dimension of the cavity. The stable pressurised crack is proposed to propagate from this maximum dimension initiation front to a distance in the rock material. This critical distance into the material a_{Ic} is defined by the following [12]:

$$a_{Ic} = \frac{1}{2\pi}\left(\frac{K_{Ic}}{\sigma_t}\right)^2 \tag{7}$$

where K_{Ic} and σ_t are the mode I fracture toughness and tensile strength of the material.

Using a stable pressurised crack to predict the breakdown pressure of an initially intact rock, that utilises fluid pressurisation inside a section of a cylindrical borehole, provides a physical hydraulic fracturing process explanation. In addition, using the theory described below, provides accurate predictions of breakdown pressures under different remote stress conditions. This stable pressurised crack is not a pre-existing notch (used in directional hydraulic fracturing), rather it is a method of calculating the breakdown pressure values occurring during hydraulic fracturing of a pressurised intact borehole section.

The hydraulic fracturing fluid is assumed incompressible and with a low value of viscosity; i.e., water at room temperature (1×10^{-3} Pa.s). In addition, the assumed rock properties are homogenous, and the rock can be either strong or weak.

The proposed stable crack is perpendicular to the minor principal stress. If the minor principal stress is in the vertical direction, i.e. a reverse faulting stress regime, the proposed stable crack is horizontal. Otherwise, if the minor principal stress is in the horizontal direction, this proposed stable crack is vertical. Therefore, depending on the

borehole axis direction and the stress regime, the proposed stable crack can be aligned with the axis of the borehole or be perpendicular to it. For example, if the borehole is vertical and the pressurised section is in a reverse faulting stress regime, then the proposed crack would be horizontal and perpendicular to the borehole.

It is further proposed that the mechanism to form the equivalent stable pressurised (with water at room temperature) crack is different for rocks with different permeability values. It is suggested that this pressurised fluid (i.e., water at room temperature), used in hydraulic fracturing, will only intrude into impermeable rock when a stable crack is produced, whereas with permeable rocks it will penetrate the material matrix to a depth approximately equal to the critical distance.

When hydraulically fracturing impermeable rock (such as granite and marble, with permeability values typically less than 10^{-18} m^2 [13]) a thin pressurised zone inside the rock with respect to the critical distance value, could only occur if the material was damaged by the fluid pressure, since there is not enough time during pressurisation for the fluid to penetrate to the critical distance or close to this value, with typical pressurisation rates ranging from 0.3 MPa per second to 1 MPa per second [41]. Therefore, it is proposed that the tensile strength must be overcome in an impermeable rock to form a stable pressurised crack. Experimental results presented in this paper support this statement (see Fig. 19 and Fig. 21 and discussions in Section 5). Therefore, to predict the breakdown pressure in hydraulic fracturing, using water at room temperature as the pressurisation fluid, the tensile strength of the rock must be added to the formulation for impermeable rock (with permeability values typically less than 10^{-18} m^2). This consideration is further supported by published experimental results that show permeable rocks have lower breakdown pressures than the impermeable rocks [3], when similar mechanical properties are measured. In addition, if the borehole is lined with an impermeable barrier prior to pressurising the rock the breakdown pressure is higher than if this barrier is not installed [3]. This impermeable barrier illustrates that a lack of fluid infiltration increases the breakdown pressure values recorded and vice versa.

In contrast, for permeable rocks, such as sandstone, where the permeability is greater than 10^{-16} m^2 [42], the fluid (i.e., water at room temperature) will infiltrate a significant distance into the material matrix [10]. It is assumed this permeation distance is approximately equal to the critical distance at breakdown. Therefore, this high pore pressure near the borehole is assumed to result in a thin pressurised zone with respect to the minor principal stress direction. The influence of this high pore pressure zone is therefore assumed equivalent to a stable circular crack. Therefore, for these rocks the tensile strength does not need to be added to the formulation presented below. This

statement assumes there is enough time during a typical pressurisation period for the pressurised fluid to penetrate the matrix of the material. However, note the tensile strength is still an important parameter that governs the breakdown pressure values for permeable rocks, using the proposed theory. This can be illustrated by inspection of Eq. (7); the higher the tensile strength the smaller the critical distance value is, and therefore, the higher the breakdown pressure is, according to the proposed theory. In addition, for a reduction in tensile strength, the larger the critical distance value, and therefore, the lower the predicted breakdown pressure is. Hence, the tensile strength influence is utilised and accounted for using the theory of critical distances, i.e. using the critical distance value presented in Eq. (7).

The mode I stress intensity factor of the proposed stable circular crack discussed above can be approximated by the following expression (see Appendix A for numerical results that indicate for the experiments performed for validation, the borehole has little influence on the stress intensity factors):

$$K_I = 2\sqrt{\frac{a}{\pi}}\left(P - \sigma_n\right) \tag{8}$$

The radius of the initiation crack a in this case, is the sum of the radius of the borehole $R,$ and the critical distance $a_{Ic}.$ The normal stress $\sigma_n,$ is equal to the minor principal stress value.

In this paper, the concept of net pressure is used to derive the mode I stress intensity factors around the crack front of a circular crack. The net pressure is defined as the internal pressure, caused in hydraulic fracturing by fluid pressure, minus the normal compressive stress on the plane of the crack, caused by the in-situ stresses. This therefore considers the summation of normal tensile stress on the surface (or plane) of the crack. The net pressure can be used for calculating the stress intensity factors because the internal pressure has more influence on the stress conditions around the crack front the closer the point of consideration is to that edge. This concept of net pressure equates to mode I stress intensity factors, because this value is the tangential stress value multiplied by $\sqrt{2\pi r}$, as the point of consideration along the plane of the crack front approaches the edge of the crack. See Fig. 18 for the definition of the stresses on an element near the crack front and Eq. (9) for the definition of mode I stress intensity factors.

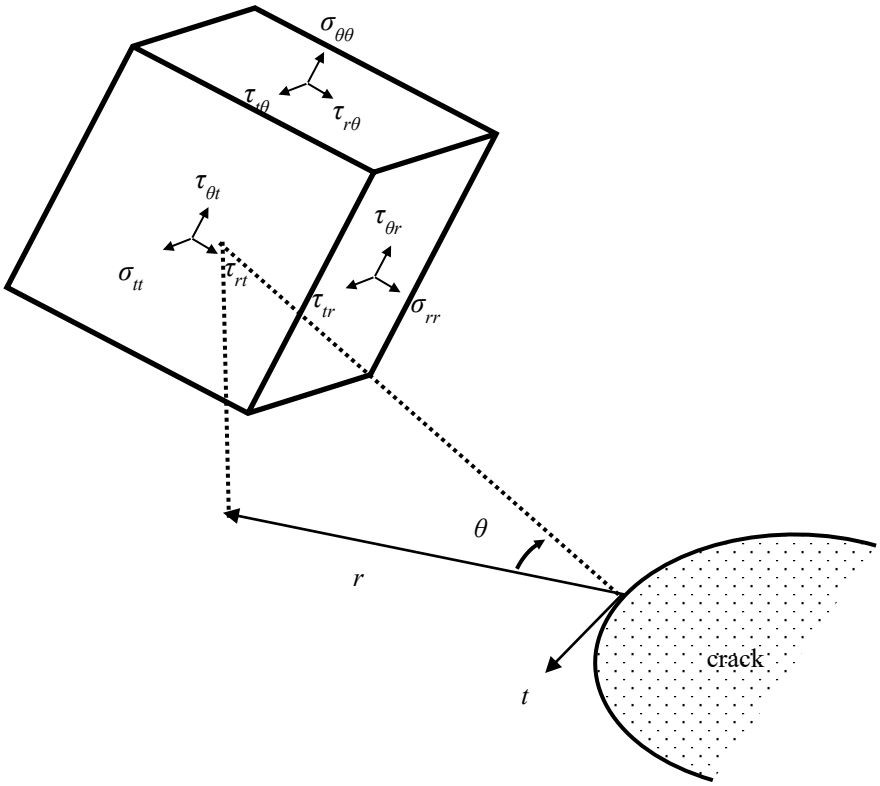

Fig. 18 Stress on an element near the crack front

The internal pressure has the greatest influence on this tangential stress, inside the crack and inside the material, just in front of the crack edge. Therefore, the net pressure is considered to accurately approximate the stress intensity factors for mode I for a pressurised crack with external compressive stresses. Note, the only stress that will significantly influence the net pressure is the minor principal stress magnitude, since the intermediate and major principal stresses will be directed along the plane of the crack and will not meaningfully affect this net pressure along the normal direction of the crack plane.

$$K_I = \lim_{r \to 0} \sigma_{\theta\theta}(r, t, \theta = 0)\sqrt{2\pi r} \tag{9}$$

As discussed in Section 1, for the experiments presented in this study, the borehole casing (or tubing) is glued onto the borehole wall and only a small section of the borehole wall is exposed to be pressurised. The attachment of the casing is considered equivalent to the use of packers in the field however, not equivalent to the rock stress determination method [2], since the length of the pressurised section of borehole is small relative to the recommended length of six times the borehole diameter. The fluid pressure will be transferred onto the surrounding material through only the exposed section.

The pressurised section of the wellbore will fracture unstably when the stress intensity factor K_I reaches the fracture toughness of the material K_{Ic}. Therefore, by setting Eq. (8) to the fracture toughness, using Eq. (7) and rearranging the equation, the following expression for the breakdown pressure P_f, can be obtained:

$$P_f = \sigma_n + \frac{K_{Ic}}{2}\sqrt{\frac{\pi}{R + a_{Ic}}} \tag{10}$$

The above Eq. (10) assumes the fracture is pressurised, since the fluid can infiltrate the crack once it is formed. The normal stress, or minor principal stress, closes the fracture therefore, the minor principal stress must be overcome before the fluid pressure will have any net tensile effect on the crack. Eq. (10) is simply derived from the net pressure role, as discussed above, which has been shown to estimate the stress intensity factor accurately for the experiments performed in this study (see Appendix A for details).

Hence, it is proposed that the breakdown pressure for the problem described above can be predicted by the following expressions:

$$P_f = \begin{cases} \sigma_n + \dfrac{K_{Ic}}{2}\sqrt{\dfrac{\pi}{R + a_{Ic}}} & \text{for permeable rocks} \\ \sigma_n + \sigma_t + \dfrac{K_{Ic}}{2}\sqrt{\dfrac{\pi}{R + a_{Ic}}} & \text{for impermeable rocks} \end{cases} \tag{11}$$

The equation for impermeable rocks was used in this study to predict the breakdown pressures for the experiments conducted in this work under non-hydrostatic stress conditions. The terms of impermeable and permeable rocks in this context are relative and threshold distinguishing between the two lie in between the permeability values for hard igneous rocks such as granite and marble and sedimentary rocks comparable to sandstone. In general, these permeability values range from 10^{-18} m^2 for hard igneous rocks and 10^{-16} m^2 for sedimentary rock [42], i.e., with a difference factor of about 100. Therefore, in the context of the above discussion, sedimentary and hard igneous rocks are loosely classified as permeable and impermeable rocks, respectively.

For hydrostatic external stress conditions, it is suggested that a spherical fractured zone is considered, since the direction of the hydraulic fracture is not known prior to testing. The shape factor, F, of $2/\pi$ is used to increase the stable crack equivalent dimension where the radius of the initiation crack is multiplied by $(R + a_{Ic})$, as discussed by Taylor [12] when dealing with spherical pores in ceramics under purely tensile external force. Therefore, under hydrostatic remote stress conditions the breakdown pressure can be predicted by the following expressions:

$$P_f = \begin{cases} \sigma_n + \dfrac{K_{Ic}}{2}\sqrt{\dfrac{4}{\pi\left(R + a_{Ic}\right)}} & \text{for permeable rocks} \\ \sigma_n + \sigma_t + \dfrac{K_{Ic}}{2}\sqrt{\dfrac{4}{\pi\left(R + a_{Ic}\right)}} & \text{for impermeable rocks} \end{cases} \tag{12}$$

In this study, the pressure values predicted by Eq. (11) and Eq. (12) were compared to our experimental measurements. It should be noted that in theory there should be a gradual change of the predicted breakdown pressure as the stress state transitions from hydrostatic to non-hydrostatic states, however this transitional change cannot be captured by Eq. (11) and Eq. (12) as they are essentially two different sets of calculations, differing by the inclusion of a constant shape factor. Therefore, Section 5 deals with the two cases separately. Further investigation is required to model this transition. For example, a variable shape factor could be constructed depending on the degree of departure of the stress condition from the hydrostatic state.

5 Results and discussions

This section presents comparison studies between prediction and measurement of breakdown pressure for non-hydrostatic and hydrostatic stress conditions. The outcomes are also compared with published results available in the literature.

For the experiments conducted in this study (see Table 6 and Table 7), the critical distance for the artificial rock is 5.51±0.79 mm, the mode I fracture toughness is 1.175±0.046 MPa$\sqrt{\text{m}}$ and the tensile strength is 6.315±0.689 MPa.

5.1 Breakdown pressure for non-hydrostatic stress conditions

Using the expression for impermeable rock given in Eq. (11) and the material constants, the difference between the average breakdown pressure and the minor principal stress was predicted to be 17.452±1.621 MPa. The standard deviation of the breakdown pressure was calculated by using tensile strength and mode I fracture toughness values one standard deviation from the mean results. This prediction used the average measured borehole diameter of approximately 6.42±0.12 mm. This measurement was taken from the borehole extrusion on the ABS mold (see Section 3.2). Note that in Table 6 the axial and confining stresses are taken at the instant when the internal pressure reaches its maximum value (or breakdown pressure), since there are slight fluctuations in these external stresses during internal pressurisation. The values in the table have been ordered from the least to the greatest minor principal stress value. The plots of the internal pressure versus cumulative volume for each experimental configuration are shown in

Appendix B (Fig. B.1 to Fig. B.9). Note that the cumulative volume is relative and in these figures, all values have been adjusted for ease of comparison, so that at 1.0 MPa of internal pressure the cumulative volume is equal to 2 mL.

Table 6 Experimental measurements with external stresses not equal

Specimen number	Specimen diameter (mm)	Specimen length (mm)	Borehole diameter (mm)	Borehole depth (mm)	Axial stress (MPa)	Confining pressure (MPa)	Breakdown pressure (MPa)
5	63.64	128.02	6.35	64.24	0.230	15.047	14.878
2	63.32	125.22	6.44	61.40	0.282	10.047	15.124
1	63.15	128.07	6.28	64.20	0.302	5.000	17.425
6	63.33	126.15	6.60	62.02	0.312	5.000	17.340
7	63.24	126.10	6.37	62.87	0.324	4.988	18.528
8	63.35	125.97	6.54	64.00	0.326	10.042	18.953
16	63.45	123.92	6.38	62.93	0.326	15.032	18.892
10	63.19	126.10	6.40	62.42	0.327	15.028	17.541
9	63.32	125.94	6.52	62.74	0.333	9.995	17.231
22	63.36	127.21	6.45	63.86	10.000	4.998	19.940
17	63.46	124.04	6.35	63.17	4.999	10.017	22.332
18	63.43	124.04	6.35	63.39	5.002	10.009	21.889
19	63.51	124.00	6.39	63.27	5.006	15.016	21.909
15	63.32	127.06	6.58	63.45	5.008	10.037	20.797
20	63.30	123.93	6.53	61.52	5.017	15.052	28.214
21	63.22	126.96	6.52	63.80	5.041	15.018	22.824
23	63.47	125.88	6.08	63.04	9.998	5.065	17.884
29	62.98	129.71	6.39	60.26	10.002	15.016	29.942
26	63.25	131.76	6.48	63.48	10.006	15.030	27.497
27	63.56	131.25	6.50	63.11	10.007	15.040	27.569
28	62.90	128.74	6.42	60.14	10.040	15.019	26.115

The predicted and measured breakdown pressures versus the minor principal stress are given in Fig. 19. The predicted breakdown pressures are aligned very closely to their measured values. The regression line of the measured values has a coefficient of determination (R^2) at 0.7718. The broken line in Fig. 19 is the line of best fit to the measured values.

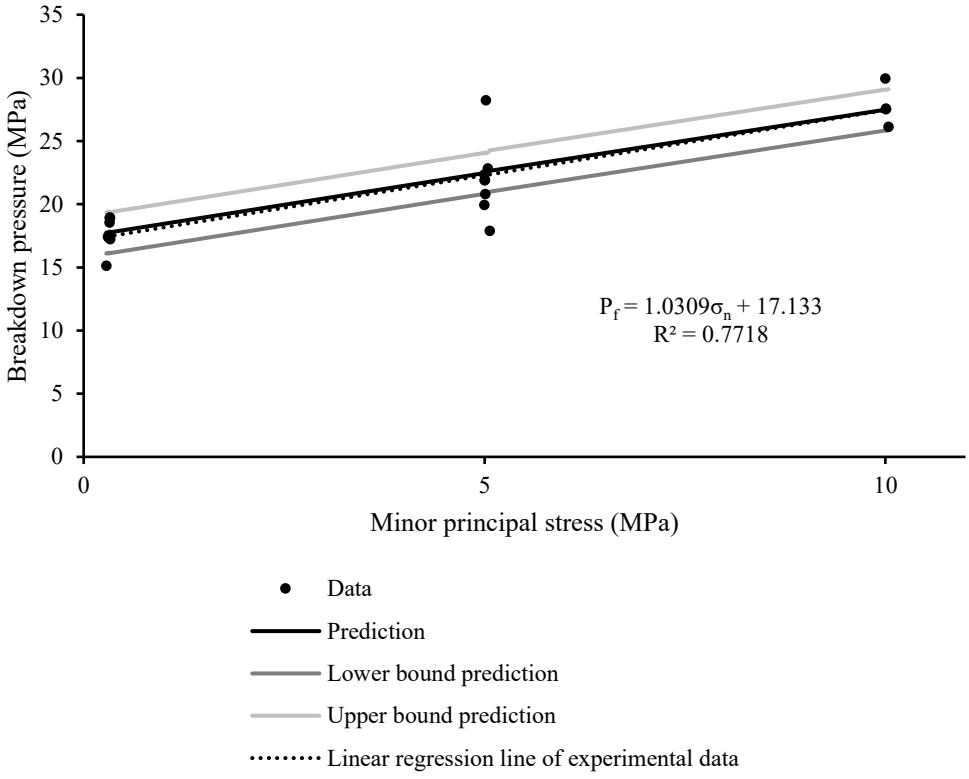

Fig. 19 Breakdown pressure versus minor principal stress for non-hydrostatic external stresses

Although the breakdown pressure is predicted very well using Eq. (11), there are significant variations in measured values at each minor principal stress. The most reasonable assumption is that these variations are caused by variations in material properties between samples. This assumption is verified by a Monte Carlo simulation study. Assuming normal distribution for these properties, random values for them can then be generated using Monte Carlo sampling. The corresponding theoretical breakdown pressure can then be calculated using Eq. (11) for each set of values produced. Using one million random samples, the distribution of predicted breakdown pressure is given in Fig. 20, where the distribution of actual measured breakdown pressures is also shown. The closeness of the two distributions suggests strongly that the variations in measured breakdown pressures are most likely caused by variations in material properties and Eq. (11) can approximate the uncertainty. As discussed in Section 3.1.3, the properties that influence the breakdown pressure, using the fracture mechanics approach used in this paper, are the tensile strength σ_t and mode I fracture toughness K_{Ic}. The variations from the average values of the tensile strength and mode I fracture toughness, follow approximately normal distributions. Hence, these variations are measured by the standard deviations of these two material properties. The additional parameters measured, according to the theory presented in this study, are taken into

consideration either by these two parameters or do not influence the breakdown pressures (see Section 3.1.3 for more discussion regarding these additional parameters).

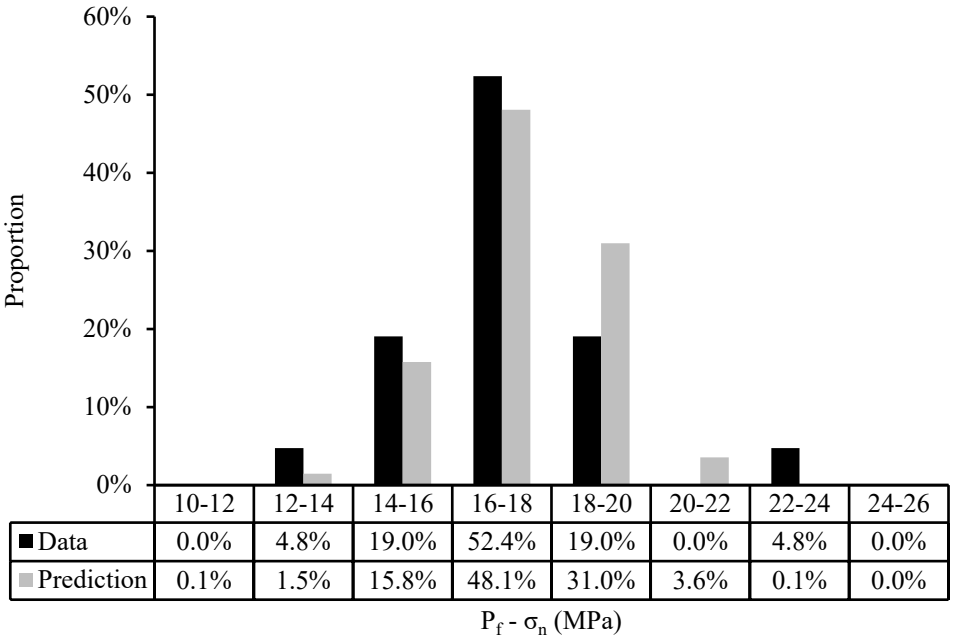

Fig. 20 Predicted and actual distributions for the artificial rock breakdown pressures minus the minor principal stress for the non-hydrostatic external stress experimental set (present study)

5.2 Breakdown pressures for hydrostatic stress conditions

Eq. (12) can be used to predict the breakdown pressure when the remote stresses are approximately equal. For the samples, using the expression for impermeable materials, the difference between the breakdown pressure and the minor principal stress was predicted to be 13.416±1.283 MPa. Similar to the non-hydrostatic stress calculation the standard deviation was predicted using the tensile strength and mode I fracture toughness values that are one standard deviation above or below. This prediction used the average measured borehole diameter of 6.41±0.05 mm. From the experiments, the difference between the actual average breakdown pressure and the minor principal stress was 12.624±0.977 MPa, which was 0.792 MPa (or 6.3%) less than the predicted value on average. Table 7 lists the experimental measurements ordered from the least to the greatest minor principal stress. Note due to the study concentrating on the reverse faulting stress regime and using a grid experimental design, only two hydrostatic stress conditions are tested in this work.

Table 7 Experimental measurements with external stresses approximately equal

Specimen number	Specimen diameter (mm)	Specimen length (mm)	Borehole diameter (mm)	Borehole depth (mm)	Axial stress (MPa)	Confining pressure (MPa)	Breakdown pressure (MPa)
14	63.00	126.58	6.46	65.81	5.001	4.950	16.272
12	62.93	129.39	6.39	62.85	5.000	4.981	17.424
13	63.17	127.20	6.47	63.83	5.003	4.987	17.204
24	63.22	127.30	6.41	62.68	10.001	10.043	23.303
25	63.35	125.64	6.34	63.45	10.003	10.026	23.837

The variation of four breakdown pressure values for two different minor principal stresses is shown in Fig. 21. One direct observation is that the predicted values are aligned very closely with the measured ones, suggesting a good applicability of Eq. (12) in this case. For the regression line of measured values, the coefficient of determination (R^2) was 0.9958 though this value must be treated with caution as only two cases of minor principal stresses are used for the regression, which will in general result in high value for R^2. The trend of points is obviously questionable for only two different minor principal stress values however, Fig. 21 is provided since it shows the interpolated values are bounded by the theory (plus or minus one standard deviation). Currently there is not enough evidence for a linear assumption, and therefore, more experiments are needed to confirm or deny this assumption in Eq. (12).

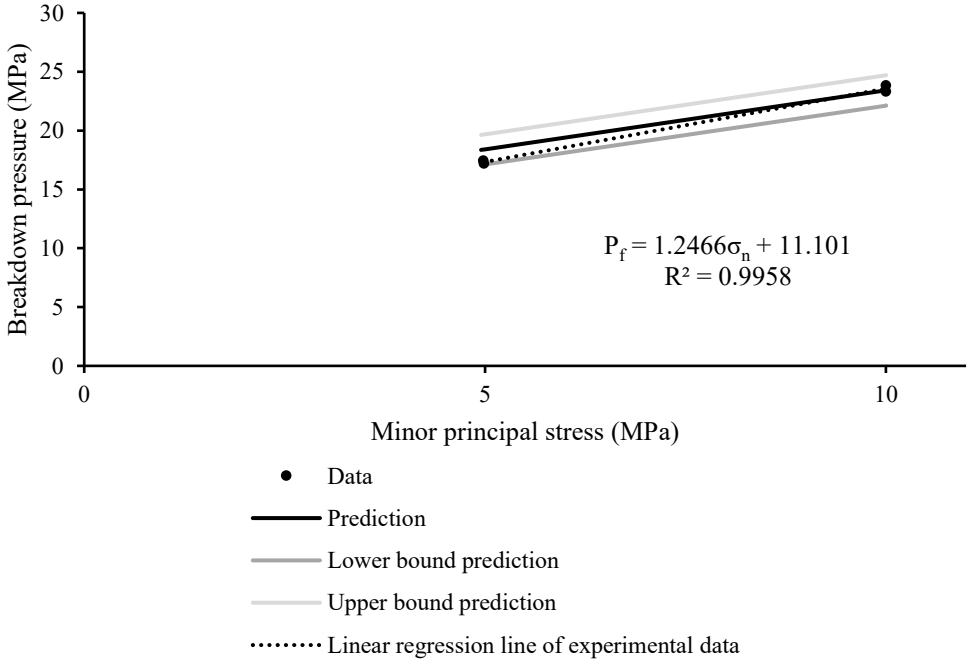

Fig. 21 Breakdown pressure versus minor principal stress for hydrostatic stress conditions

Similarly, Monte Carlo simulation is used to assess the variation in breakdown pressure minus the minor principal stress, considering uncertainties in material properties (see Fig. 22). Based on the simulation results, it seems Eq. (12) tends to over-predict the true

breakdown pressure, though the average values of both distributions are similar, as previously discussed.

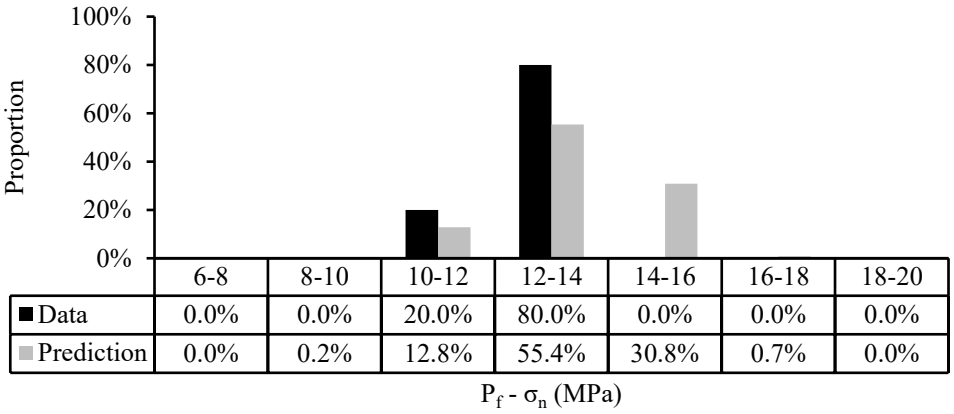

Fig. 22 Predicted and actual distributions for the artificial rock breakdown pressures minus minor principal stress for the hydrostatic external stress experimental set (present study)

As discussed in Section 4.1 for these conditions, the initial stable crack formation direction is not known. From these experiments on the artificial rock (described in Section 3.1, i.e. strong brittle concrete), subjected to these hydrostatic conditions, using specimens with a central borehole (see Fig. 13) with a small section of this borehole being pressurised at the centre of these samples, can produce multiple fractures with different orientations. The hydrostatic stress condition was created by using a Hoek cell to create equal horizontal stresses, and the vertical stress was kept the same value as this confining stress. The vertical stress used the measured cross-sectional area and the required calculated load to generate the same confining stress magnitude. The average borehole diameter was approximately 6.42±0.12 mm for all specimens. The average external diameter of all specimens was approximately 63.28±0.19 mm. Usually, the hydraulic fracture must be perpendicular to the minor principal stress, but because these specimens are under hydrostatic conditions, the fracture can propagate along weaknesses in the artificial rock, since there is no preferred orientation for the hydraulic fracture to grow. Fig. 23 shows evidence of sub-horizontal and sub-vertical fractures on the surface of specimen number 24, which was under approximately 10 MPa hydrostatic remote stress conditions. The fluid bleeding on the surface of the specimen clearly demonstrates the formations of multiple fractures. This indirectly confirms the reason to include a shape factor, as discussed in Section 4.1.

Fig. 23 Specimen number 24 with sub-horizontal and sub-vertical surface fractures under approximately 10 MPa hydrostatic remote stress conditions

5.3 Comparison study with published experimental results

The proposed theory was used to predict and compare breakdown pressures with some published experimental studies. Four types of rocks with their material properties included in their publications in the literature were selected for this comparison study. The predicted values from the proposed theory align well with the measured breakdown pressures for these experimental studies (Table 8).

Table 8 Summary of comparisons between other experimental studies and the presented theory

Rock type	**Reference Study**	**Average measured breakdown pressure (MPa)**	**Tensile strength (MPa)**	**Fracture toughness (MPa$\sqrt{m}$)**	**Predicted breakdown pressure (MPa)**	**Predicted initiation pressure range (MPa)** [1]
Honkomatsu andesite	Ito and Hayashi [1]	9.567±0.85 × 1.3*	12.10±1.2	1.19±0.12	13.043 ±1.041	10.015 to 30.933
Kofu andesite	Ito and Hayashi [1]	14.133±4.000 × 1.3*	11.10±1.1	1.62±0.16	15.674 ±1.176	9.280 to 17.006
Ruhr sandstone	Zoback *et al.* [9]	22.120±2.834	13.20±2.3[37]	1.40±0.11[38]	21.630 ±2.653	11.563 to 62.286
Westerly granite	Solberg *et al.* [46]	116.015±10.199	10.77±5.64	1.46±0.75	131.942 ±16.669	110.101 to 2,478.933

*Factor corresponding to the approximate pressure difference between initiation and breakdown pressures

Note that Honkomatsu andesite, Kofu andesite and Westerly granite use the impermeable version of Eq. (11), whereas Ruhr sandstone uses the permeable version of Eq. (11), to

generate the predicted breakdown pressures shown in Table 8. Hence, tensile strength must be used in both formulations. For Ruhr sandstone, the tensile strength is only used to calculate the critical distance value that determines the size of the assumed stable crack. Whereas, for andesite and granite the tensile strength is both used to determine the size of the assumed stable crack and added to the formulation to capture the assumed mechanism of pressurisation i.e., fluid pressure using water at room temperature breaking the rock before the rock can be pressurised.

The initiation pressure range is based on Eq. (5) and Eq. (6). The poro-elastic constant was assumed 0.85 for Ruhr sandstone [43], and to give the largest range of initiation pressure for Westerly granite the constant was assumed zero. The measured poro-elastic constants were used for Honkomatsu andesite (0.648) and Kofu andesite (0.381) [3].

As previously discussed, Ito and Hayashi [3] reported the pressure to initiate fracturing rather than the maximum pressure that the rock could withstand so the predicted breakdown pressures using the proposed theory is expected to be higher than the initiation pressure reported, as can be seen in Table 8. The comparison for this case is further complicated since they used a constant pressurisation rate rather than a constant flow rate. Note that using a constant flow rate is the recommended method by the International Society of Rock Mechanics (ISRM) for rock stress determination using the hydraulic fracturing technique [2].

To make the reported values comparable to the breakdown pressure discussed in this paper, the initiation pressure values were multiplied by 1.3, which corresponds to the approximate pressure difference between an initiation pressure and a breakdown pressure presented graphically by Ito and Hayashi [3]. Monte Carlo simulations were performed for both Kofu and Honkomatsu andesite assuming that these rocks were permeable to fluid prior to unstable fracturing. In addition, the fracture toughness and tensile strength values were assumed to follow normal distributions with a 10% standard deviation from their base (reported) values. The actual and simulated breakdown pressures were grouped into 2 MPa and 5 MPa increments for Honkomatsu and Kofu andesite, as shown in their distributions in Fig. 24 (a) and (b).

The range of breakdown pressure for Ruhr sandstone reported in Zoback *et al.* [9] based on flow rate controlled experiments was between 19.6 MPa and 29.1 MPa. However, the tensile strength and fracture toughness value of the rock were not reported for Ruhr sandstone in this study. To apply the proposed theory, the fracture toughness value of the rock was sourced from the Single Edge Notched Beam in Bending (SENBB) for Ruhr sandstone reported by Ouchterlony [44] and the tensile strength was sourced from the

Brazilian disc tests for Ruhr sandstone by Molenda *et al.* [45]. Based on these values, the predicted breakdown pressure, using the permeable rock expression in Eq. (11), for Ruhr sandstone with a 1.5 mm borehole radius was between 18.924 MPa and 24.230 MPa with one standard deviation, which is similar to the actual breakdown pressure range reported in Zoback *et al.* [9] (see Table 8). Note, the tensile strength value is only used for calculating the critical distance value to predict the breakdown pressures (as discussed in Section 4.1 for permeable material). A Monte Carlo simulation was also performed to predict the distribution of breakdown pressure when uncertainties in fracture toughness and tensile strength were considered and the results are shown in Fig. 24 (c). In these predictions, the Ruhr sandstone was considered permeable and rock properties are assumed to distribute normally.

Solberg *et al.* [46] recorded an average breakdown pressure, under room temperature conditions, of 116.015 MPa, with a range of variation between 101 MPa and 127 MPa for Westerly granite. Using the range of values listed in Table 1 to approximate the mechanical properties of Westerly granite, the predicted range of breakdown pressure was between 110 MPa and 131 MPa with the minor principal stress set at 100 MPa, the value used in the experiments [46]. Four out of the five reported breakdown pressures are within this predicted range. For Monte Carlo simulations, the average of the range listed in Table 1 was taken to be the mean value and half the range was the standard deviation of the mechanical properties, which are assumed to follow normal distributions. The rock is assumed impermeable. The simulation results are shown in Fig. 24 (d).

(a)

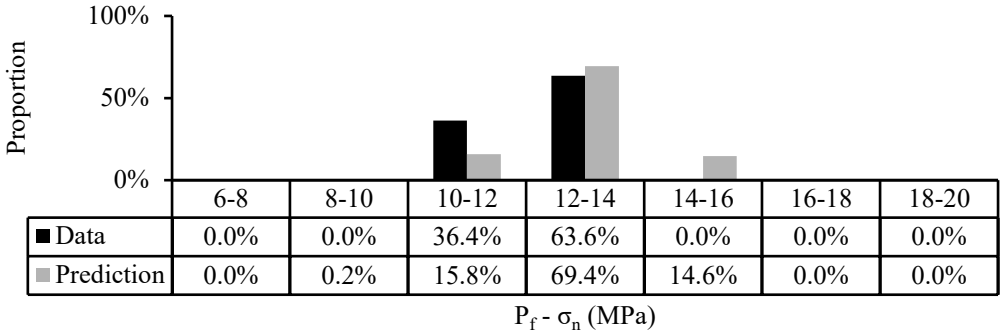

	6-8	8-10	10-12	12-14	14-16	16-18	18-20
Data	0.0%	0.0%	36.4%	63.6%	0.0%	0.0%	0.0%
Prediction	0.0%	0.2%	15.8%	69.4%	14.6%	0.0%	0.0%

P_f - σ_n (MPa)

(b)

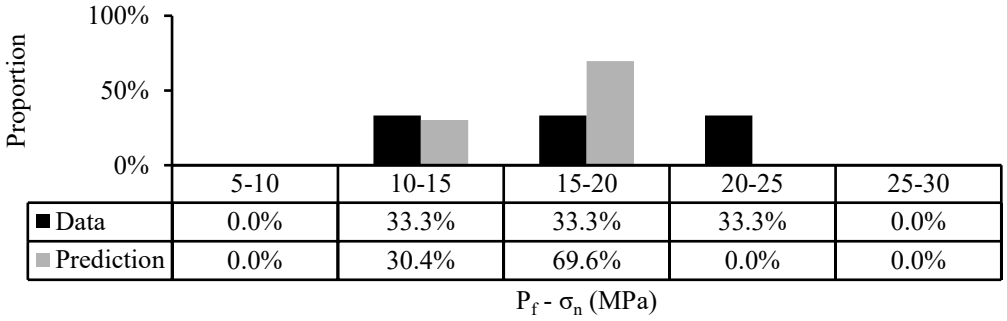

	5-10	10-15	15-20	20-25	25-30
Data	0.0%	33.3%	33.3%	33.3%	0.0%
Prediction	0.0%	30.4%	69.6%	0.0%	0.0%

P_f - σ_n (MPa)

(c)

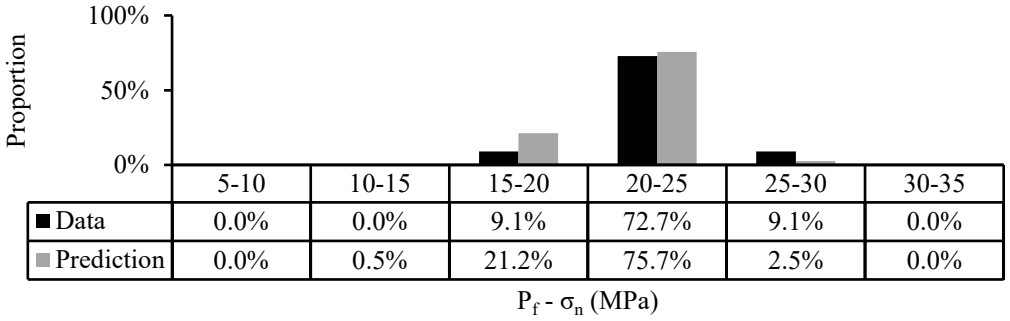

	5-10	10-15	15-20	20-25	25-30	30-35
Data	0.0%	0.0%	9.1%	72.7%	9.1%	0.0%
Prediction	0.0%	0.5%	21.2%	75.7%	2.5%	0.0%

P_f - σ_n (MPa)

(d)

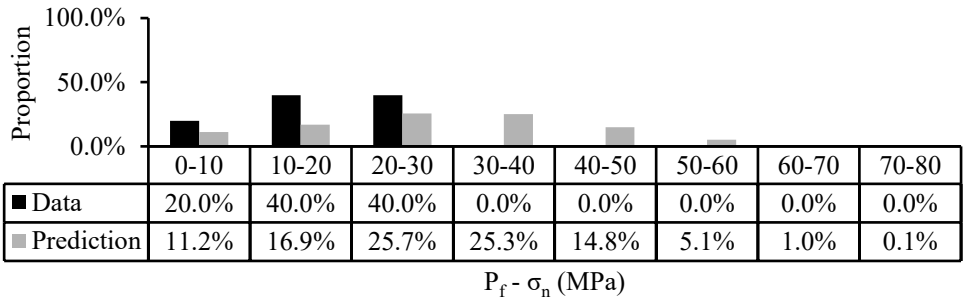

	0-10	10-20	20-30	30-40	40-50	50-60	60-70	70-80
Data	20.0%	40.0%	40.0%	0.0%	0.0%	0.0%	0.0%	0.0%
Prediction	11.2%	16.9%	25.7%	25.3%	14.8%	5.1%	1.0%	0.1%

P_f - σ_n (MPa)

Fig. 24 Predicted and actual distributions of breakdown pressures for (a) Honkomatsu andesite, (b) Kofu andesite, (c) Ruhr sandstone, and (d) Westerly granite

6 Conclusions

A new theory has been proposed to predict the breakdown pressure in hydraulic fracturing operations. To validate the theory, hydraulic fracturing experiments were conducted on cylindrical specimens under conventional triaxial compression conditions. In addition, published experimental results of breakdown pressure for several different types of rocks from previous hydraulic fracturing studies were also included in the validation analysis to further support the proposed theory. The theory is derived based on the widely-accepted assumption that a stable crack is formed perpendicular to the minor principal stress prior to failure of the rock. A circular crack is assumed with a radius equal to the sum of the pressurised borehole and the distance where the stable crack develops i.e., the critical distance. This distance between the wall of the borehole and the front of the crack is a material constant and can be calculated from the mode I fracture toughness and tensile strength of the material. With the proposed theory, the breakdown pressures during hydraulic fracturing are dependent on the borehole radius, whereby the predicted breakdown pressure decreases with increasing the borehole radius, unlike conventional prediction methods where the predicted breakdown pressure is independent of the borehole radius. This inverse relationship is supported by former studies.

The measured breakdown pressures from our experiments align very well with their predicted values based on the proposed theory. It is encouraging to see that predicted values also follow published experimental results closely. One topic that needs to be considered in future research is the gradual transition of breakdown pressures from hydrostatic to non-hydrostatic stress conditions, which cannot be predicted using the proposed theory at this stage.

Acknowledgements

The authors would like to thank Adam Ryntjes and Simon Golding for their assistance with the laboratory setup and experiments.

Appendix

A. Numerical simulations

A series of numerical simulations were performed to confirm the analytical stress intensity factors. The software used to insert the crack into the finite element mesh and analyse the stress intensity factors using the M-integral [47] was FRANC3D [48]. This software links with the commercial software ABAQUS, which solves the finite element model.

A cuboid is assumed equivalent to the cylindrical specimens. This cuboid is chosen so that the approximate cylindrical dimensions inscribe the surfaces of the rectangular prism. Explicitly, the approximate specimen diameter and the X and Y dimensions of the model are both 63.5 mm (see Table A.1 for the other geometric properties).

Table A.1 Geometric properties of the models

Geometric properties	Value
Model X dimension (mm)	63.5
Model Y dimension (mm)	63.5
Model Z dimension (mm)	127.0
Crack shape	Circular
Crack radius	$R + a_{Ic}$
Crack inclination	Perpendicular to the minor principal stress

The analysed crack shape is assumed circular so that it corresponds to the analytical expression in Eq. (11). For every experimental set (see Section 3.2 – Table 5), the values that are used in the simulations are averaged. For instance, the axial stress and confining pressures at failure (or breakdown) for each set are averaged. The internal traction modelled on the crack face is the average breakdown pressure for each set minus the measured tensile strength σ_t. The crack radii are the summation of the measured borehole radii and the critical distance for the material under consideration (5.51 mm).

The borehole was included in the model where possible. This borehole is assumed to form a complete bond with material and extend 63.5 mm into the material. The injection tubes are stainless steel so the elastic modulus was 200 GPa and the Poisson's ratio was 0.305 in this section. The injection tube internal dimeter of 2.11 mm (see Fig. 15) was not included, since this conduit conducts the internal fluid pressure. This internal fluid pressure would act on the assumed stable crack at this opening. In addition, the opening is small compared with the approximate outer diameter of the injection tube of 6.35 mm. For these reasons, this borehole section was assumed solid stainless steel. The borehole could not be modelled when the crack was vertical i.e., in a normal faulting stress regime. The vertical crack cannot intersect the stainless-steel material region. This is a limitation with FRANC3D. Therefore, to produce the model the specimen was

considered as a single material i.e., it only used the linear elastic properties of the concrete, previously reported in Section 3.1.3. Otherwise, if the crack was horizontal it was placed 0.05 mm away from the borehole region (in the Z direction) in the concrete material section.

The boundary conditions of these models were that the end with the stainless-steel region was pinned in the Z direction and the corners of the X and Y directions on one side were pinned in the X and Y directions, respectively. These boundary conditions were selected so the finite element model would not rotate nor deform away or into the platen (see Fig. 14).

The numerical and analytical stress intensity factors align well with an average absolute relative difference of 2.28% (see Table A.2). The analytical stress intensity factors for the hydrostatic stress regimes could not be compared with numerical results, since a spherical ellipsoid void could not be inserted into these models due to limitations with FRANC3D.

Table A.2 Stress intensity factors from analytical and numerical analyses

Borehole modelled	**Axial stress (MPa)**	**Confining pressure (MPa)**	**P_f - σ_t (MPa)**	**Crack radius (mm)**	**K_I Analytical ($MPa\sqrt{m}$)**	**K_I Numerical ($MPa\sqrt{m}$)**	**Relative change**
Yes	0.294	15.036	10.789	8.70	1.105	1.127	1.99%
Yes	0.313	4.996	11.450	8.72	1.174	1.169	0.38%
Yes	0.314	10.475	10.788	8.76	1.106	1.115	0.80%
-	5.002	4.973	9.974	8.73	0.828	-	-
Yes	5.003	10.021	15.358	8.72	1.091	1.056	3.36%
Yes	5.021	15.029	18.001	8.75	1.370	1.347	1.72%
No	9.999	5.031	12.597	8.64	0.794	0.810	1.97%
-	10.002	10.034	20.036	8.70	1.659	-	-
Yes	10.014	15.027	21.466	8.74	1.208	1.142	5.78%
				Average	**1.148**	**1.109**	**2.28%**

The stress intensity factors from the analytical expression and numerical results were plotted against the minor principal stress values. This illustrates the independence with the minor principal stress. The mean fracture toughness value of the artificial rock is plotted as a reference to the stress intensity factors at failure of this material. These stress intensity factors align with the measured fracture toughness (see Fig. A.1).

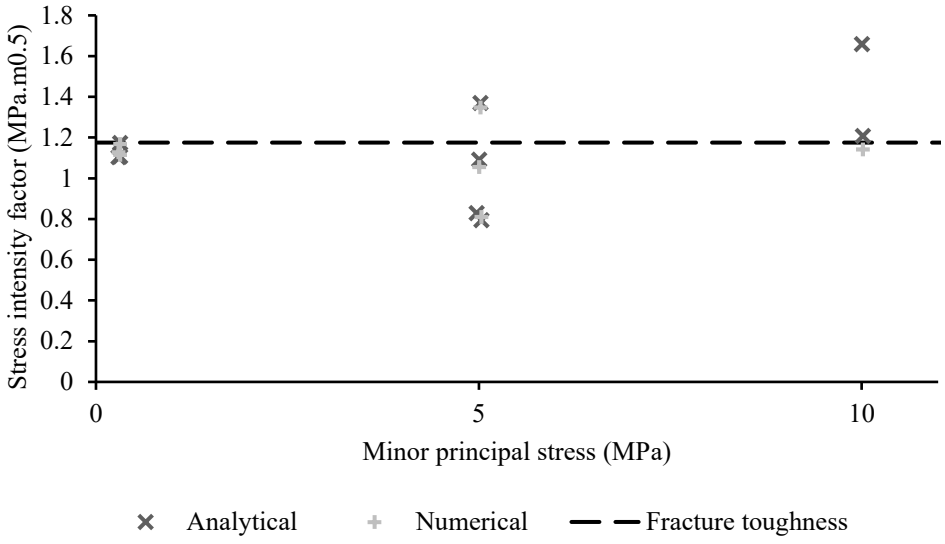

Fig. A.1 Stress intensity factors versus minor principal stress

For an example of how the major principal stress distribution changes around the borehole see Fig. A.2.

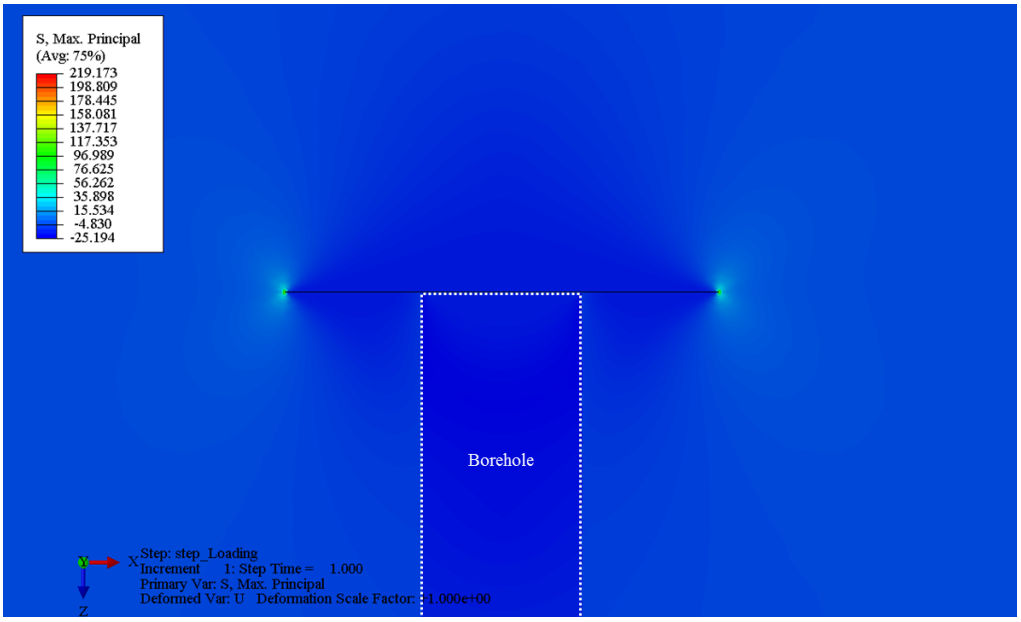

Fig. A.2 Major principal stress distribution around a horizontal crack with a stainless-steel borehole region – axial stress of 5.021 MPa and confining pressure of 15.029 MPa, and internal pressure of 15.358 MPa (Note: negative stress values are compressive and positive stress values are tensile)

B. Experimental results

The following graphs (Fig. B.1 to Fig. B.9) show the pressure versus cumulative volume of fracturing fluid injected for each experiment. The reason for presenting these graphs is to illustrate the variability in each experimental set and to provide data for modelling purposes.

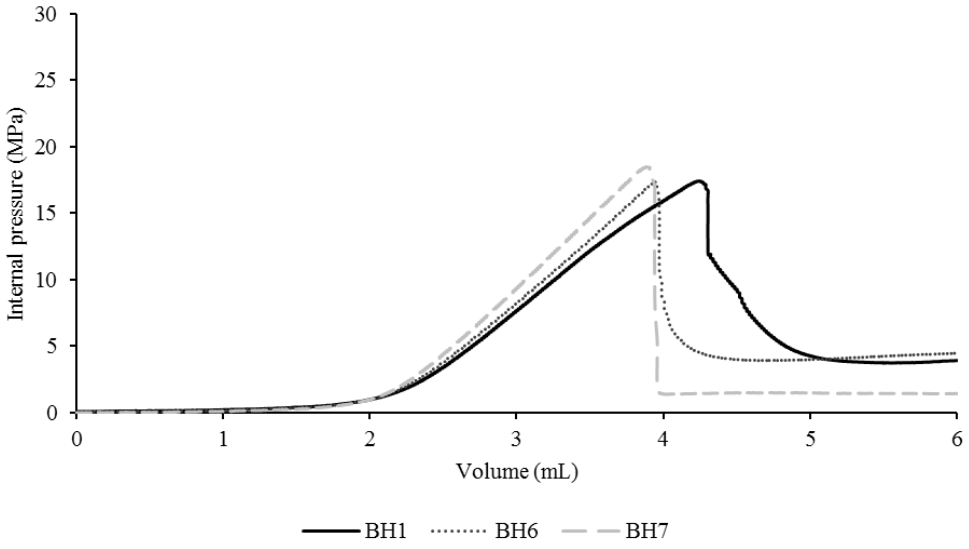

Fig. B.1 Pressure versus cumulative volume for target external stresses of 5 MPa confining pressure and 0 MPa axial stress

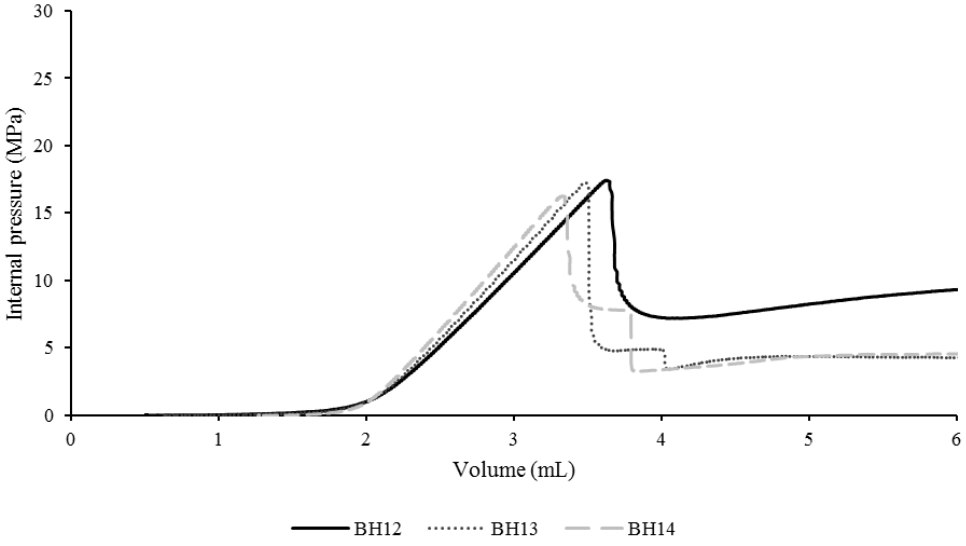

Fig. B.2 Pressure versus cumulative volume for target external stresses of 5 MPa confining pressure and 5 MPa axial stress

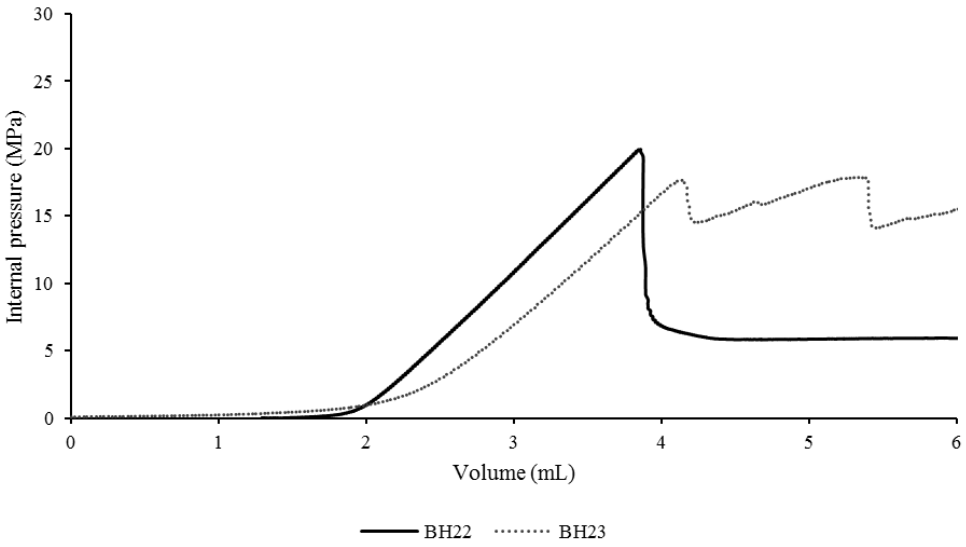

Fig. B.3 Pressure versus cumulative volume for target external stresses of 5 MPa confining pressure and 10 MPa axial stress

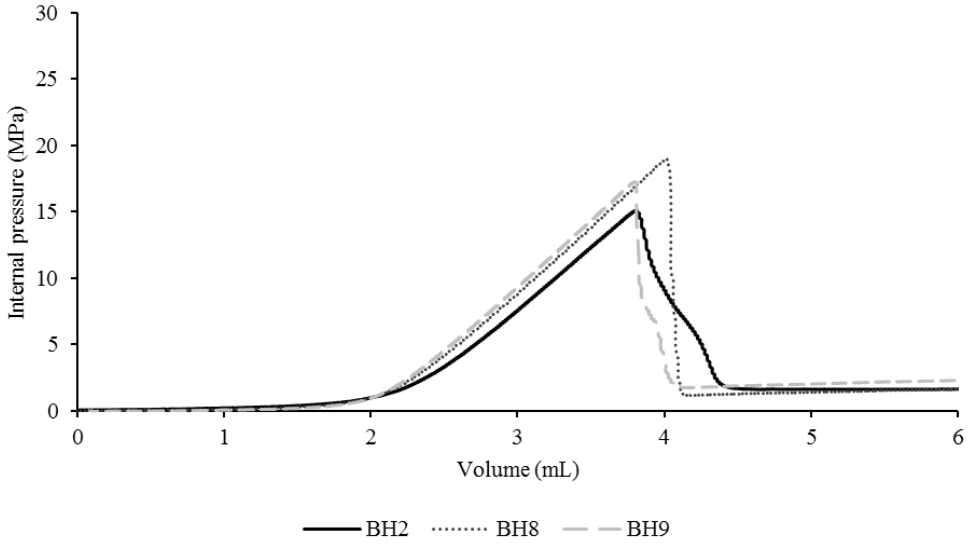

Fig. B.4 Pressure versus cumulative volume for target external stresses of 10 MPa confining pressure and 0 MPa axial stress

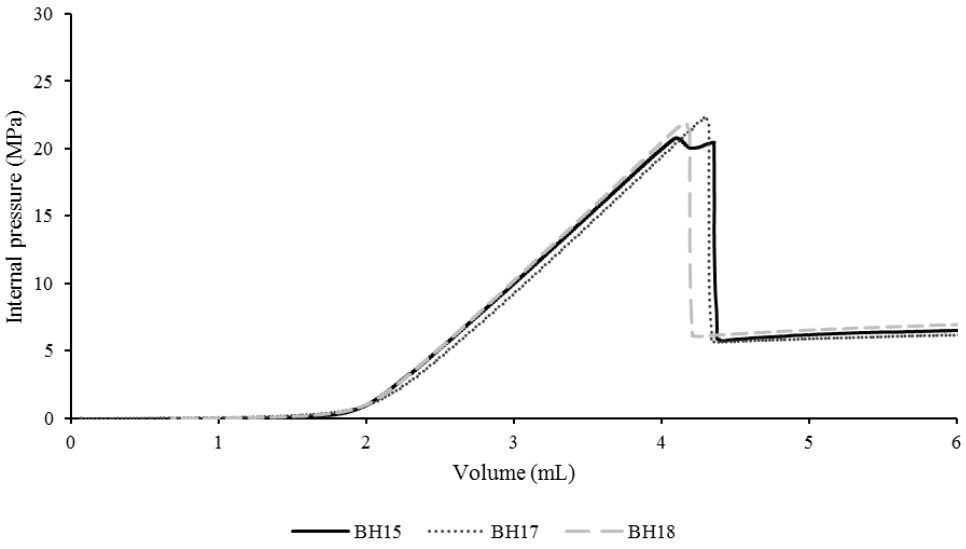

Fig. B.5 Pressure versus cumulative volume for target external stresses of 10 MPa confining pressure and 5 MPa axial stress

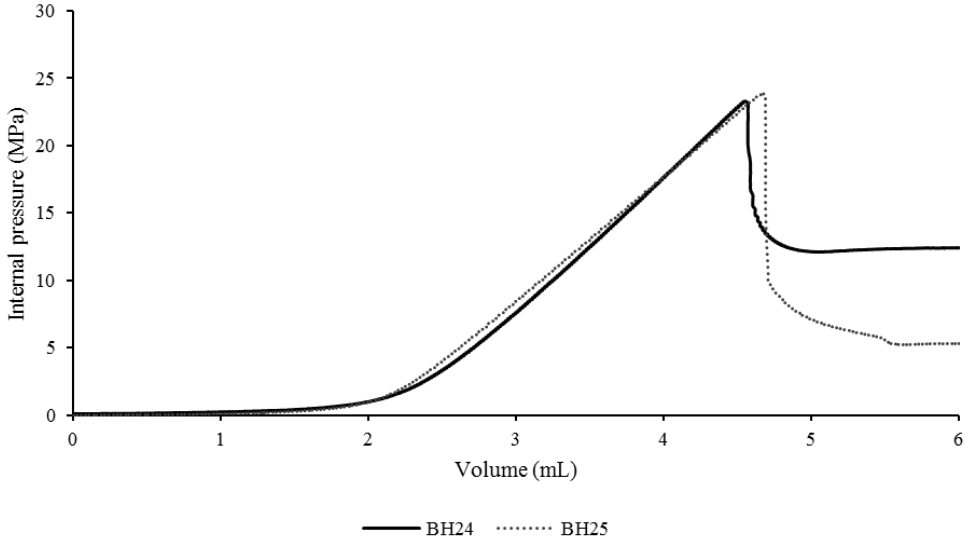

Fig. B.6 Pressure versus cumulative volume for target external stresses of 10 MPa confining pressure and 10 MPa axial stress

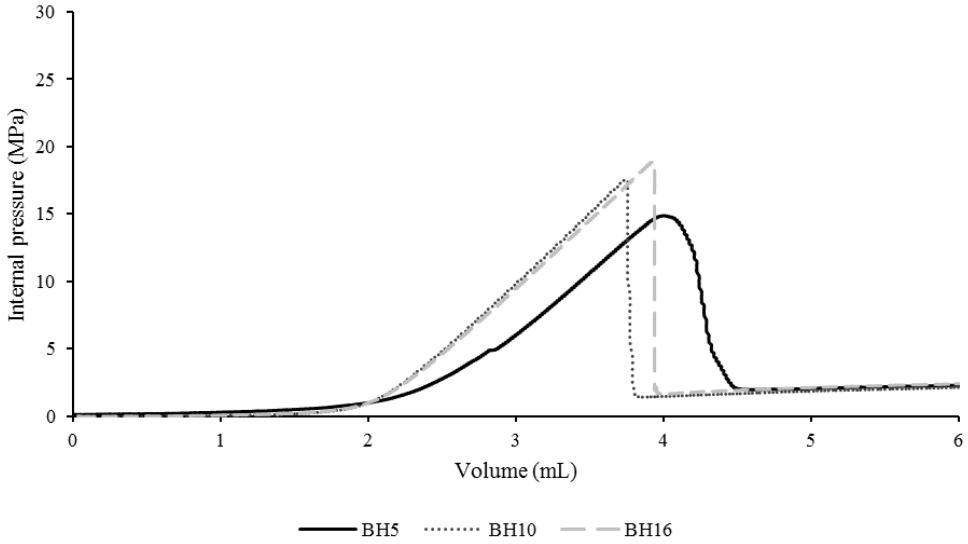

Fig. B.7 Pressure versus cumulative volume for target external stresses of 15 MPa confining pressure and 0 MPa axial stress

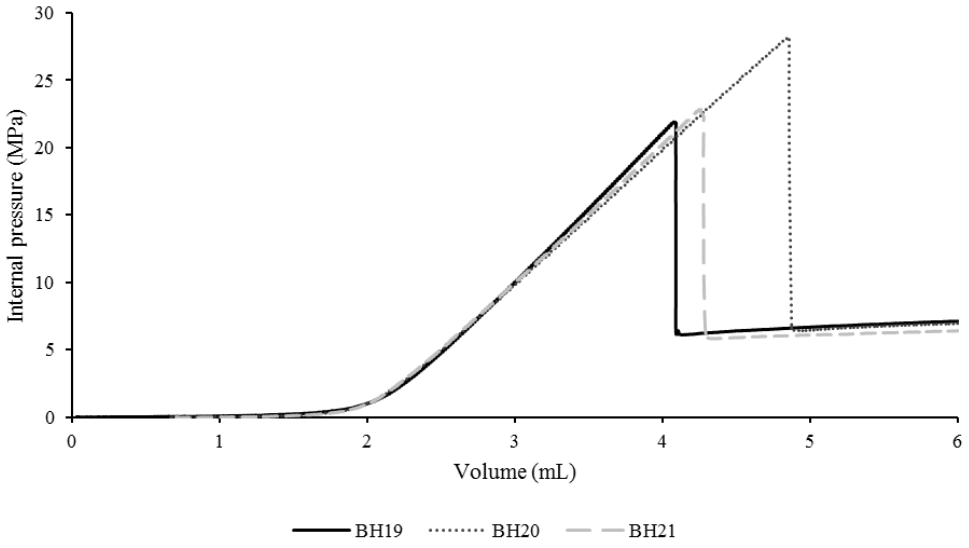

Fig. B.8 Pressure versus cumulative volume for target external stresses of 15 MPa confining pressure and 5 MPa axial stress

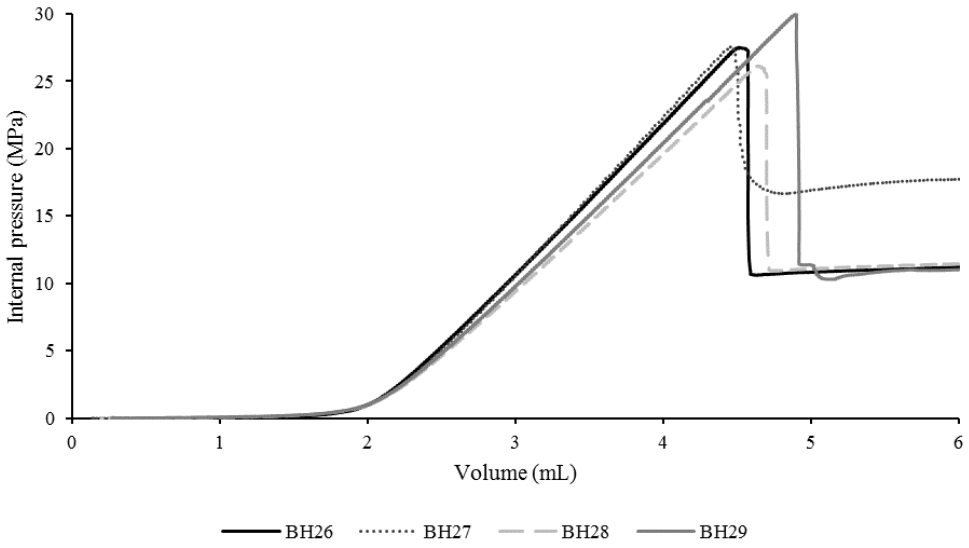

Fig. B.9 Pressure versus cumulative volume for target external stresses of 15 MPa confining pressure and 10 MPa axial stress

References

1. Fjær E, Holt RM, Horsrud P, Raaen AM, Risnes R. Chapter 11 Mechanics of hydraulic fracturing. In: E. Fjær RMHPHAMR, Risnes R, eds. *Developments in Petroleum Science.* Vol Volume 53. Elsevier; 2008:369-390.

2. Haimson B, Cornet F. ISRM suggested methods for rock stress estimation—part 3: hydraulic fracturing (HF) and/or hydraulic testing of pre-existing fractures (HTPF). *Int J Rock Mech Min Sci.* 2003;40(7): 1011-1020.

3. Ito T, Hayashi K. Physical background to the breakdown pressure in hydraulic fracturing tectonic stress measurements. *International Journal of Rock Mechanics and Mining Sciences & Geomechanics Abstracts.* 1991;28(4): 285-293.

4. Haimson BC, Fairhurst C. Hydraulic fracturing in porous-permeable materials. *J Pet Technol.* 1969;21(07): 811-817.

5. Guo F, Morgenstern NR, Scott JD. Interpretation of hydraulic fracturing breakdown pressure. *International Journal of Rock Mechanics and Mining Sciences & Geomechanics Abstracts.* 30. Elsevier; 1993:617-626.

6. Kirsch G. Theory of elasticity and application in strength of materials. *Zeitchrift Vevein Deutscher Ingenieure.* 1898;42(29): 797-807.

7. Bradley WB. Failure of Inclined Boreholes. *Journal of Energy Resources Technology.* 1979;101(4): 232-239.

8. Ito T. Effect of pore pressure gradient on fracture initiation in fluid saturated porous media: Rock. *Eng Fract Mech.* 2008;75(7): 1753-1762.

9. Zoback MD, Rummel F, Jung R, Raleigh CB. Laboratory hydraulic fracturing experiments in intact and pre-fractured rock. *Int J Rock Mech Min Sci.* 1977;14(2): 49-58.

10. Morita N, Black A, Fuh G-F. Borehole breakdown pressure with drilling fluids—I. Empirical results. *International Journal of Rock Mechanics and Mining Sciences.* 33. Elsevier; 1996:39-51.

11. Hubbert MK, Willis DG. Mechanics of hydraulic fracturing. *J Am Assoc Pet Geol.* 1957;18(12).

12. Taylor D. *The theory of critical distances: a new perspective in fracture mechanics*: Elsevier; 2010.

13. Khan K, Al-Shayea NA. Effect of Specimen Geometry and Testing Method on Mixed Mode I–II Fracture Toughness of a Limestone Rock from Saudi Arabia. *Rock Mech Rock Eng.* 2000;33(3): 179-206.

14. Nara Y, Takada M, Mori D, Owada H, Yoneda T, Kaneko K. Subcritical crack growth and long-term strength in rock and cementitious material. *Int J Fract.* 2010;164(1): 57-71.

15. Majer EL, Baria R, Stark M, et al. Induced seismicity associated with Enhanced Geothermal Systems. *Geothermics.* 2007;36(3): 185-222.

16. Zimmermann G, Reinicke A. Hydraulic stimulation of a deep sandstone reservoir to develop an Enhanced Geothermal System: Laboratory and field experiments. *Geothermics.* 2010;39(1): 70-77.

17. Fridleifsson IB, Freeston DH. Geothermal energy research and development. *Geothermics.* 1994;23(2): 175-214.

18. Caineng Z, Guangya Z, Shizhen T, et al. Geological features, major discoveries and unconventional petroleum geology in the global petroleum exploration. *Petroleum Exploration and Development.* 2010;37(2): 129-145.

19. Häring MO, Schanz U, Ladner F, Dyer BC. Characterisation of the Basel 1 enhanced geothermal system. *Geothermics.* 2008;37(5): 469-495.

20. Rogner H-H. An assessment of world hydrocarbon resources. *Annu Rev Energy Environ.* 1997;22: 217-262.

21. Alejano LR, González J, Muralha J. Comparison of different techniques of tilt testing and basic friction angle variability assessment. *Rock Mech Rock Eng.* 2012;45(6): 1023-1035.

22. Arzúa J, Alejano LR. Dilation in granite during servo-controlled triaxial strength tests. *Int J Rock Mech Min Sci.* 2013;61(0): 43-56.

23. Backers T, Stephansson O, Rybacki E. Rock fracture toughness testing in Mode II—punch-through shear test. *Int J Rock Mech Min Sci.* 2002;39(6): 755-769.

24. Bell FG. *Engineering properties of soils and rocks*: Elsevier; 2013.

25. Stimpson B. Modelling materials for engineering rock mechanics. *International Journal of Rock Mechanics and Mining Sciences & Geomechanics Abstracts.* 1970;7(1): 77-121.

26. Yesiloglu-Gultekin N, Gokceoglu C, Sezer EA. Prediction of uniaxial compressive strength of granitic rocks by various nonlinear tools and comparison of their performances. *Int J Rock Mech Min Sci.* 2013;62(0): 113-122.

27. Sano O, Kudo Y, Mizuta Y. Experimental determination of elastic constants of Oshima granite, Barre granite, and Chelmsford granite. *Journal of Geophysical Research: Solid Earth.* 1992;97(B3): 3367-3379.

28. Sundberg J, Back P-E, Ericsson LO, Wrafter J. Estimation of thermal conductivity and its spatial variability in igneous rocks from in situ density logging. *Int J Rock Mech Min Sci.* 2009;46(6): 1023-1028.

29. Nasseri MHB, Mohanty B. Fracture toughness anisotropy in granitic rocks. *Int J Rock Mech Min Sci.* 2008;45(2): 167-193.

30. Xu C. *Cracked Brazilian disc for rock fracture toughness testing: theoretical background, numerical calibration and experimental validation*: Verlag Dr. Muller; 2010.

31. Brace WF, Walsh JB, Frangos WT. Permeability of granite under high pressure. *J Geophys Res.* 1968;73(6): 2225-2236.

32. Nur A, Byerlee JD. An exact effective stress law for elastic deformation of rock with fluids. *J Geophys Res.* 1971;76(26): 6414-6419.

33. Byerlee J. Friction of rocks. *Pure Appl Geophys.* 1978;116(4-5): 615-626.

34. Guo F, Morgenstern NR, Scott JD. An experimental investigation into hydraulic fracture propagation—Part 1. Experimental facilities. *Int J Rock Mech Min Sci.* 1993;30(3): 177-188.

35. Bieniawski Z, Bernede M. Suggested methods for determining the uniaxial compressive strength and deformability of rock materials. *International Journal of Rock Mechanics and Mining Sciences & Geomechanics Abstracts.* 16. Elsevier; 1979:138-140.

36. Suggested methods for determining tensile strength of rock materials. *International Journal of Rock Mechanics and Mining Sciences & Geomechanics Abstracts.* 1978;15(3): 99-103.

37. Kovari K, Tisa A, Einstein H, Franklin J. Suggested methods for determining the strength of rock materials in triaxial compression: revised version. *Int J Rock Mech Min Sci.* 1983;20(6): 283-290.

38. Fowell RJ. Suggested method for determining mode I fracture toughness using cracked chevron notched Brazilian disc (CCNBD) specimens. *International Journal of Rock Mechanics and Mining Sciences & Geomechanics Abstracts.* 32. Pergamon; 1995:57-64.

39. Backers T, Stephansson O. ISRM suggested method for the determination of mode II fracture toughness. *Rock Mech Rock Eng.* 2012: 1-12.

40. Hillis RR, Meyer JJ, Reynolds SD. The Australian stress map. *Explor Geophys.* 1998;29(3/4): 420-427.

41. Haimson BC, Zhao Z. Effect of borehole size and pressurization rate on hydraulic fracturing breakdown pressure. American Rock Mechanics Association; 1991.

42. Rice JR, Cleary MP. Some basic stress diffusion solutions for fluid-saturated elastic porous media with compressible constituents. *Rev Geophys.* 1976;14(2): 227-241.

43. Knutson C, Bohor B. Reservoir rock behavior under moderate confining pressure. *Proceedings of the Fifth US Symposium on Rock Mechanics.* 1963:627-659.

44. Ouchterlony F. *Review of fracture toughness testing of rock*: SveDeFo, Stiftelsen Svensk Detonikforskning; 1980.

45. Molenda M, Stöckert F, Brenne S, Alber M. Comparison of Hydraulic and Conventional Tensile Strength Tests. *ISRM International Conference for Effective and Sustainable Hydraulic Fracturing.* International Society for Rock Mechanics; 2013.

46. Solberg P, Lockner D, Byerlee JD. Hydraulic fracturing in granite under geothermal conditions. *Int J Rock Mech Min Sci.* 1980;17(1): 25-33.

47. Wawrzynek P, Carter B, Banks-Sills L. *The M-Integral for computing stress intensity factors in generally anisotropic materials*: National Aeronautics and Space Administration, Marshall Space Flight Center; 2005.

48. Wawrzynek P, Carter B, Ingraffea A. Advances in simulation of arbitrary 3D crack growth using FRANC3D NG. *12th International Conference on Fracture.* Ottawa; 2009.

Paper 3

Statement of Authorship

Title of Paper	Breakdown pressure and propagation surface of a hydraulically pressurized circular notch within a rock material
Publication Status	☐ Published ☐ Accepted for Publication ☐ Submitted for Publication ☑ Unpublished and Unsubmitted w ork w ritten in manuscript style
Publication Details	

Principal Author

Name of Principal Author (Candidate)	Adam Karl Schwartzkopff
Contribution to the Paper	Conducted experiments, performed numerical analyses, wrote manuscript and acted as corresponding author.
Overall percentage (%)	90%
Certification:	This paper reports on original research I conducted during the period of my Higher Degree by Research candidature and is not subject to any obligations or contractual agreements with a third party that would constrain its inclusion in this thesis. I am the primary author of this paper.
Signature	Date Friday 19 August 2016

Co-Author Contributions

By signing the Statement of Authorship, each author certifies that:

i. the candidate's stated contribution to the publication is accurate (as detailed above);
ii. permission is granted for the candidate in include the publication in the thesis; and
iii. the sum of all co-author contributions is equal to 100% less the candidate's stated contribution.

Name of Co-Author	Nouné Sophie Melkoumian
Contribution to the Paper	Supervised development of work and reviewed manuscript.
Signature	Date Friday 19 August 2016

Name of Co-Author	Chaoshui Xu
Contribution to the Paper	Supervised development of work and reviewed manuscript.
Signature	Date Friday 19 August 2016

Breakdown pressure and propagation surface of a hydraulically pressurized circular notch within a rock material

Adam K. Schwartzkopff [a]
Nouné S. Melkoumian [a]
Chaoshui Xu [a]

[a] School of Civil, Environmental and Mining Engineering, Faculty of Engineering, Computer and Mathematical Sciences, The University of Adelaide, SA 5005 Australia

Abstract

Rock masses have pre-existing cracks that weaken the rock. Generally, these cracks are not considered when predicting the maximum injection pressure, i.e. the breakdown pressure, in hydraulic fracture stimulations. In addition, a pre-existing crack intersecting a hydraulically pressurized section of a borehole may produce a non-planar fracture propagation surface. To gain a better understanding of this problem, a series of hydraulic fracturing experiments were conducted to investigate the breakdown pressures and fracture propagation surfaces of a pressurized circular thin notch to represent a crack, subjected to external triaxial stress conditions. These are the first experimental attempt to quantify the role of circular notches in hydraulic fracturing. The results show that the breakdown pressures can be estimated using only the resultant normal stress on the plane of the notch, under the shear stress conditions studied. The propagation surfaces from experiments are mapped and compared to numerical predictions based on the maximum tangential stress criterion and these were found to align closely with each other. In addition, this study provides evidence that via the hydraulic fracturing process, the propagation of arbitrarily orientated notches will eventually realign to be perpendicular to the minor principal stress direction.

Keywords: hydraulic fracturing, fracture mechanics, fracture propagation, breakdown pressure

Nomenclature

a	radius or major axis of the elliptical crack (m)
a_{median}	median crack increment input for FRANC3D (m)
b	minor axis of the elliptical crack (m)
inc	predefined incremental length for the proposed analytical method (m)
$inc_{FRANC3D}(\varphi)$	incremental length used in FRANC3D (m)
$K_{I(median)}$	median stress intensity factor for mode I along the crack front (Pa$\sqrt{\text{m}}$)
$K_I(\varphi)$	stress intensity factor for mode I (Pa$\sqrt{\text{m}}$)
$K_{II}(\varphi)$	stress intensity factor for mode II (Pa$\sqrt{\text{m}}$)
$K_{III}(\varphi)$	stress intensity factor for mode III (Pa$\sqrt{\text{m}}$)
K_{Ic}	fracture toughness for mode I (Pa$\sqrt{\text{m}}$)
n	power input for calculating the incremental length in FRANC3D
α	dip direction (°)
β	dip angle (°)
γ	ellipse angle – the direction from the projected dip direction on the crack plane to the major axis of the ellipse (°)
θ	crack front angle – from the normal to the crack front towards the positive z axis direction (°)
$\theta_c(\varphi)$	critical crack front angle (°)
υ	Poisson's ratio
$\sigma_{n(eff)}$	effective normal stress on the surface of the crack (Pa)
$\sigma_{n(external)}$	normal stress on the surface of the crack (Pa)
τ	shear stress along the surface of the crack (Pa)
τ_{eff}	effective shear stress along the surface of the crack (Pa)
φ	crack front angle – from the x axis direction clockwise around the normal vector in the positive z axis direction (°)
ω	shear angle – clockwise around the normal vector in the positive z axis direction (°)
LEFM	linear elastic fracture mechanics

1 Introduction

It is important to be able to predict the fracture propagation surfaces resulting from hydraulic fracturing, since these fractures provide the primary permeable pathways for hydrocarbon extraction in oil and gas engineering and the heat exchange areas for geothermal energy exploitation. The pre-existing and induced fracture surfaces from hydraulic fracturing influence the permeable pathways by connecting cracks and voids in the rock. The in-situ stress conditions of a rock mass and the internal pressure of cracks control the propagation surface resulting from hydraulic fracturing. For intact rock and rock masses (discontinuous rock), the hydraulic fracturing process produces fracture propagation surfaces that are perpendicular to the minor principal stress direction. The presence of discontinuities in the rock mass however, increases the complexity of fracture propagation.

The first occurrence of pre-existing cracks on the fracture propagation surface in hydraulic fracturing is when the pressurised borehole section is intersected by discontinuities. Note that pre-existing discontinuities not intersecting the borehole can affect the shape and orientation of the hydraulic fracture propagation into the rock mass, however, this aspect has not been addressed in this study. Hence, this study considers the influence of a pre-existing pressurized circular notch, to represent a crack, intersecting a pressurised borehole section on the fracture propagation surface produced via hydraulic fracturing. This paper demonstrates that the fracture propagation surfaces can be approximately modelled and the associated breakdown pressure can be estimated using the theory of linear elastic fracture mechanics (LEFM). This predictive approach is not capable of predicting in-situ stresses, since the orientation and size of the intersecting crack and two of the compressive principal stress magnitudes and directions must be known, in order to calculate the third compressive principal stress magnitude. However, the aim of this paper is not to predict the in-situ stress conditions, but to calculate the influence of a circular crack intersecting a pressurised section of borehole on the breakdown pressure and resultant fracture propagation surface.

Hydraulic fracturing experiments using intact rock have shown that the fracture propagation surface produced is perpendicular to the minor principal stress direction (e.g. Hubbert and Willis [1]). The same process is assumed to govern the hydraulic fracture propagation in a discontinuous rock mass, whereby the propagation surface will eventually realign to be perpendicular to the minor principal stress direction, but through a complex tortuous propagation process.

There has been little experimental work into this reorientation process in hydraulic fracturing. Zoback *et al.* [2] produced one of the first investigations into the influence of pre-existing fractures on hydraulic fracturing, where the pre-existing fracture was perpendicular to the only applied stress, i.e. major external principal stress (there was no other external stresses applied to these specimens). Using this pre-existing fracture orientation, they were not able to study the reorientation process, since a new fracture was produced parallel to the direction of the major external principal stress. Zhang and Chen [3] studied the role of the perforation orientation on the resultant fracture propagation surface by controlling the initial crack orientation in intact rock. The perforation orientation was controlled by directing the fluid pressure through an orifice. In their specimens, they did not actually introduce a pre-existing crack. Nonetheless, the fluid injection point (or perforation orientation) generated an initial fracture orientation that was not perpendicular to the minor principal stress. The external horizontal stress difference was reported to be 4 MPa, using a true triaxial cell. The angle between the perforation orientation and the maximum horizontal applied stress direction was 55°. In this reported experiment, the induced fracture eventually reoriented to be approximately perpendicular to the minor principal stress direction. Yan *et al.* [4] assessed the influence of pre-existing weaknesses on hydraulic fracturing by placing an A4 piece of paper into four concrete specimens. Two of these specimens had the A4 piece of paper intersecting the borehole. They did not report digitised propagation surfaces. Although, they did conclude that the fracture propagated in the direction of the pre-existing weakness and gradually reoriented to be perpendicular to the minor principal stress direction. For the two specimens with a pre-existing weakness intersecting the borehole the applied compressive external stress conditions were 10 MPa in the vertical direction, and 6 MPa and 4 MPa in the horizontal directions. They provided a photograph of the resultant fracture propagation surface with the specimen that had a weakness perpendicular to the central injection tube. From inspection, the hydraulic fracture propagated a short distance (approximately 0.1 m) until reorientation to perpendicular to the minor principal stress direction. These three studies illustrate the need for a detailed investigation into the breakdown pressures and propagation surfaces from inclined pre-existing notches in rock-like material.

In this research, the experimental study conducted provides digitised propagation surfaces of the reorientation process from inclined circular notches (which replicate cracks). These digitised propagation surfaces could be used in future studies for validating three dimensional hydraulic fracturing models. In addition, the breakdown pressures are reported for each experiment.

The existing three dimensional hydraulic fracturing numerical methods [5-8] require benchmarking cases for non-planar fracture growth. Therefore, numerical simulations using FRANC3D [9] were conducted in this research to determine if the hydraulic fracture propagation surfaces from the experiments could be predicted. These numerical simulations assumed that the fracturing process could be modelled by LEFM and therefore FRANC3D calculated the stress intensity factors for each quasi-static step to generate the fracture propagation surface. The maximum tangential stress criterion was used to determine this reorientation process. Other assumptions in the numerical modelling include that the internal hydraulic pressure from the previous time step is maintained, i.e. the breakdown pressure is used as an internal pressure at all steps, and that the pore pressure change around the fracture was negligible. It has been demonstrated that for most cases presented, the fracture propagation surface could be predicted using this technique.

2 Methods

The detailed experimental method is presented in this section. The properties of the material used in the hydraulic fracturing experiments are reported, and the procedure for the hydraulic fracturing experiments is described below.

2.1 Material and specimen preparation

The material used in this study was chosen so that it would be homogeneous, isotropic, and brittle. In this study, a high strength concrete with properties similar to granite was used. The rocks subjected to hydraulic fracturing treatments in general are of low permeability [10-13]. However, the rock types that are present in geothermal or unconventional gas systems are different. Engineered geothermal systems are generally located in granite basements with overlain sediments [10, 14], whereas unconventional gas reservoirs are in general located in shales or mudstones [15].

The ranges of reported properties of granite are obtained from the literature [16-22], and are listed in Table 1. These values were used as the basis to compare the mechanical properties of the artificial rock (concrete) as obtained from experiments, and are listed in Table 3. Since there is variability due to different geological materials in granitic rocks, Table 1 should only be used as a guide.

Table 1 Range of granite mechanical properties

Material characteristic	Minimum reported value	Maximum reported value	Minimum number of values	References
Elastic modulus (GPa)	18	109	17	Arzúa and Alejano [16], Backers *et al.* [17], Bell [18] and Stimpson [19]
Poisson's ratio	0.16	0.19	4	Arzúa and Alejano [16] and Backers *et al.* [17]
Uniaxial compressive strength (MPa)	64	321	124	Arzúa and Alejano [16], Bell [18] and Yesiloglu-Gultekin *et al.* [20]
Mode I fracture toughness (MPa$\sqrt{m}$)	0.71	2.20	74	Nasseri and Mohanty [21] and Xu [22]

A prototype specimen was created by using the material mass ratios reported in Table 2. Part of the mould was created from acrylonitrile butadiene styrene (ABS) using a three dimensional printer. A plastic cylinder was placed around the component created in the three dimensional printer to create a central cavity into which the high strength concrete mixture was poured (see Fig. 1).

Fig. 1 Prototype mould of the 75° pre-existing circular notch

The same procedure was followed for all samples, as stated below. Once the specimen was cured (after 28 days in the fog room), the centre plastic cylinder was drilled out, using a 6.30 mm diameter drill bit, to create a borehole in the specimen. The plastic disc inside the body was then removed by submerging the cured material in a vessel filled with acetone for approximately 4 weeks (28 days). All plastics were removed successfully using this process to create the desired borehole and circular notch, to represent a crack, at the bottom of the borehole, as shown in Fig. 2.

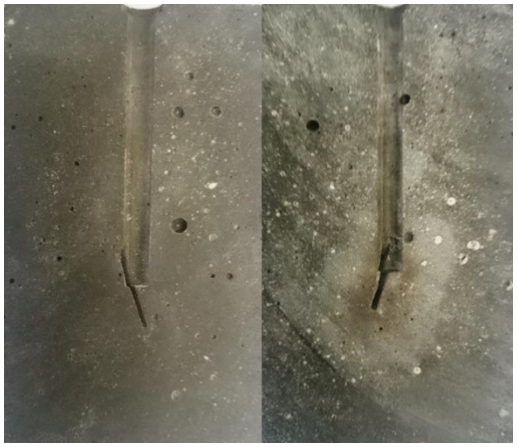

Fig. 2 Prototype specimen cut in half along the axis of the borehole, showing a 75° pre-existing circular notch at the bottom of the borehole section (on both halves)

The designed specimen geometry is shown in Fig. 3. The indent was designed as a well for the epoxy (Sika Anchorfix®-3+).

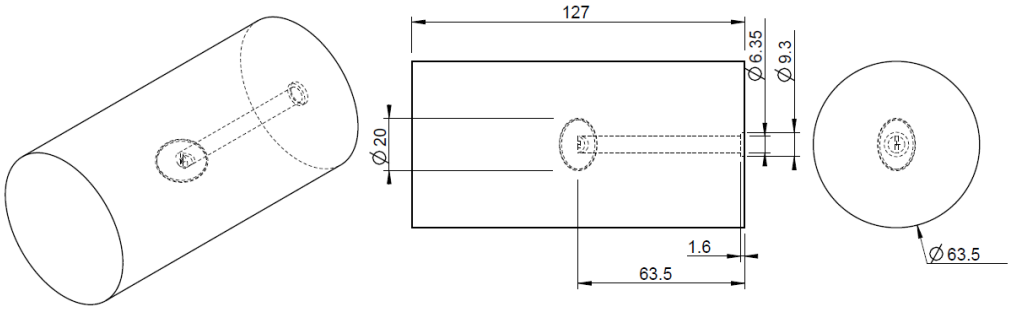

Fig. 3 Hydraulic fracturing specimen dimensions with 45° inclined circular crack

For measuring the mechanical properties of created artificial rocks two solid high strength concrete (i.e. artificial rock) blocks were created from two separate mixtures using the same masses of the base materials (see Table 2). The purpose for two separate mixtures was to test the consistency of the mechanical properties. The dimensions of the blocks were 450 mm × 450 mm × 200 mm.

Table 2 Materials and mass values for the artificial rock mixture

Materials	**Mass ratios**
Sulphate resisting cement	1
Sand 60G	0.5
Sand 30/60	0.5
Silica fume	0.266
Water	0.165
Super plasticizer (ViscoCrete®10)	0.06
Total	**2.491**

The following procedures (adapted from Guo *et al.* [23]) in order of completion were used to ensure the production of high strength concrete as required:

1. Line the inside walls of the wooden formwork with oil
2. Fix the formwork on a vibrating table
3. Mix the sulphate resisting cement, Sand 60G, Sand 30/60 and silica fume for an average of 15 minutes to achieve homogeneous distribution of material
4. While the sand and gypsum are being mixed, dissolve the super-plasticizer in water (at room temperature)
5. Add the super-plasticizer solution to the sand and gypsum mixture and mix for a further 50 minutes until the mixture was consistent
6. Fill the wooden formwork with the mixture
7. Compact the mixture by vibration
8. Systematically poke a sharp steel rod into the mixture to remove air pockets
9. Remove the specimen from the vibrating table after completely filling the wooden formwork and leave it to set for 12 hours
10. While in the formwork, cover with wet hessian for an average of 2 days
11. Remove the material from the mould and let the specimen cure at 46±2°C at 30% relative humidity for 28 days
12. Once cured remove the material from the fog room and store it at room temperature for 28 days
13. Cut and grind the material blocks into the desired shape (7 days)
14. Dry specimens in oven at 100°C for 12 hours

The reason for storing the material outside the fog room at room temperature for a further 28 days was to ensure there was minimal change in the strength and mechanical characteristics during the period of testing, which lasted 5 days.

To model the material, the deformability parameters were obtained by using the International Society of Rock Mechanics suggested method [24]. There were 12 cylindrical samples prepared to obtain the deformability parameters of Poisson's ratio and elastic modulus and six of those specimens were taken to the ultimate load.

All 12 cylindrical samples were measured and the average diameter was 63.3±0.04 mm and the average height was 175.0±0.09 mm, therefore the height to diameter ratio was 2.76, which was between the suggested ratios of 2.5 to 3.0. Strain gauges were used for the six specimens taken to their ultimate load, and for the other six specimens extensometers were used (see Fig. 4). For one specimen from each block, both strain measurement methods were used to determine the relative error of these two methods. The average error between these two methods was 0.0014% strain and therefore was

considered negligible. The average deformability parameters are used in the modelling of the material (see Table 3).

Fig. 4 Cylindrical specimen before deformability testing commenced with strain gauges and extensometers

Mode I fracture toughness was obtained from tests on 14 cracked chevron notched Brazilian disc specimens [25]. The average thickness of these disks was 35.0±0.04 mm and the average diameter was 106.4±0.10 mm. The half-length of the maximum part of the slot (a_1) was 29.5±0.07 mm and the minimum half-length of the slot (a_0) was 12.07±0.08 mm (see Fig. 5).

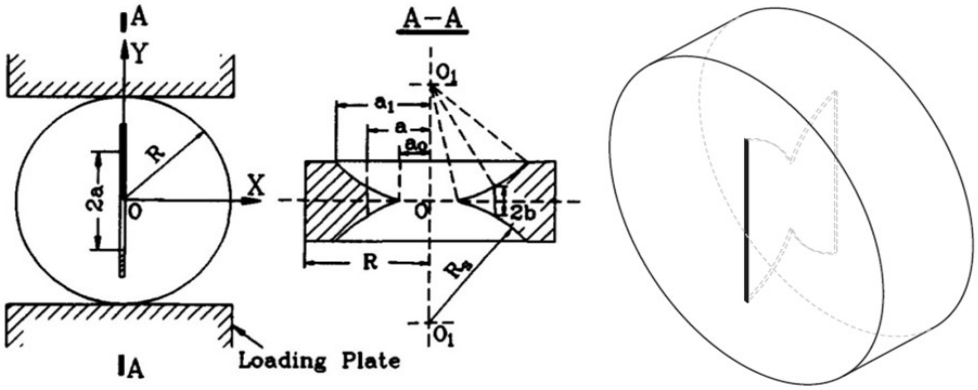

Fig. 5 The cracked chevron Brazilian disc specimen geometry with recommended test fixture (from Fowell [23])

As shown in Table 3 the material properties of the high strength concrete are similar to that of granite.

Table 3 Summary of the material properties

Material characteristic	Value	Standard error value	Standard error percentage	Number of values	Minimum reported value for granite	Maximum reported value for granite
Elastic modulus (GPa)	46.32	1.48	3.2%	12	18	109
Poisson's ratio	0.217	0.017	7.8%	12	0.16	0.19
Uniaxial compressive strength (MPa)	183.6	3.9	2.1%	6	64	321
Mode I fracture toughness ($MPa\sqrt{m}$)	1.18	0.05	3.9%	14	0.71	2.20

2.2 Hydraulic fracturing experiments

To investigate the breakdown pressures and the resultant hydraulic fracture propagation surfaces, 40 specimens with pre-existing notches were tested. These notches were to replicate pre-existing fractures as close as practically possible. These specimens consisted of eight groups with five specimens per group (see Table 4):

Table 4 Specimen group definitions

Group	Orientation	Compressive normal stress (MPa)	Shear stress (MPa)
1	Horizontal	0.00	0.00
2	Inclined*	0.00	0.00
3	Vertical	0.00	0.00
4	Inclined*	10.00	0.50
5	Inclined*	10.00	1.00
6	Inclined*	10.00	1.50
7	Inclined*	10.00	2.00
8	Inclined*	10.00	2.50

*Inclined crack plane dip angles (from horizontal) vary from 15° to 75° in 15° increments

Groups 1 to 3 were hydraulically fractured with no external stresses. The purpose of these tests was to provide a reference (baseline) point for the measurements breakdown pressures and the resultant fracture propagation surfaces when external stresses are applied.

Groups 4 to 8, with inclined pre-existing notches, to act as pre-existing cracks, were tested under different confining and axial stresses. The confining and axial stresses varied for these experiments to produce a consistent 10 MPa of compressive normal stress on the pre-existing fracture with different shear stresses ranging from 0.5 MPa to 2.5 MPa, in 0.5 MPa increments. The key purpose of this experimental setup was to investigate the influences of the magnitude of shear stresses on the breakdown pressure and the resultant fracture propagation surfaces. Detailed experimental setups are listed in Table 5.

Table 5 Experiment design

Dip angle (°)	Confining stress (MPa)	Axial stress (MPa)	Normal stress (MPa)	Shear stress (MPa)
0	0.00	0.00	0.00	0.00
0	0.00	0.00	0.00	0.00
0	0.00	0.00	0.00	0.00
0	0.00	0.00	0.00	0.00
0	0.00	0.00	0.00	0.00
15	0.00	0.00	0.00	0.00
30	0.00	0.00	0.00	0.00
45	0.00	0.00	0.00	0.00
60	0.00	0.00	0.00	0.00
75	0.00	0.00	0.00	0.00
90	0.00	0.00	0.00	0.00
90	0.00	0.00	0.00	0.00
90	0.00	0.00	0.00	0.00
90	0.00	0.00	0.00	0.00
90	0.00	0.00	0.00	0.00
15	8.13	10.13	10.00	0.50
30	10.87	9.71	10.00	0.50
45	10.50	9.50	10.00	0.50
60	9.71	10.87	10.00	0.50
75	10.13	8.13	10.00	0.50
15	13.73	9.73	10.00	1.00
30	11.73	9.42	10.00	1.00
45	11.00	9.00	10.00	1.00
60	9.42	11.73	10.00	1.00
75	9.73	13.73	10.00	1.00
15	15.60	9.60	10.00	1.50
30	12.60	9.13	10.00	1.50
45	8.50	11.50	10.00	1.50
60	9.13	12.60	10.00	1.50
75	10.40	4.40	10.00	1.50
15	2.54	10.54	10.00	2.00
30	6.54	11.15	10.00	2.00
45	12.00	8.00	10.00	2.00
60	11.15	6.54	10.00	2.00
75	10.54	2.54	10.00	2.00
15	19.33	9.33	10.00	2.50
30	14.33	8.56	10.00	2.50
45	12.50	7.50	10.00	2.50
60	8.56	14.33	10.00	2.50
75	9.33	19.33	10.00	2.50

An axial platen with an internal conduit and threaded system was designed and manufactured to transfer hydraulic pressure into the specimen (see Fig. 6).

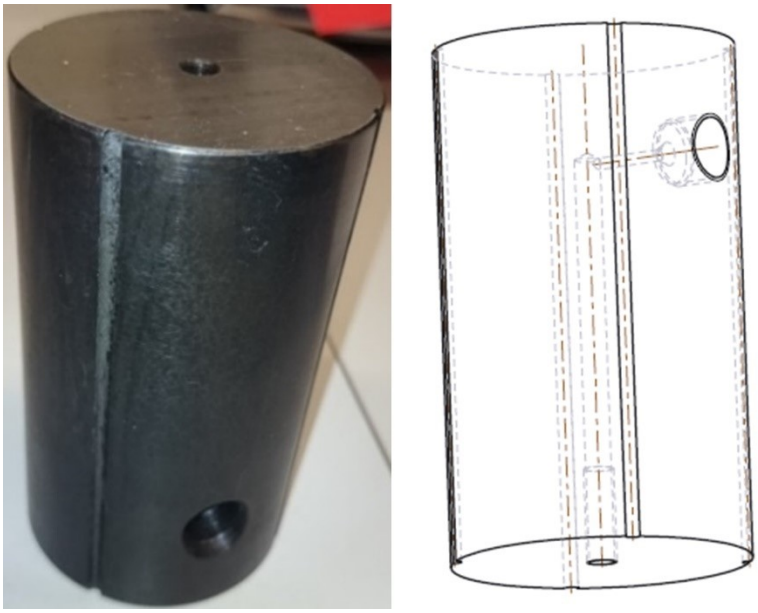

Fig. 6 Axial platen with internal conduit to transfer pressure into the specimen

An injection tube (see Fig. 7 for its dimensions) was coated in epoxy and then placed into the borehole of the specimen. This was done approximately 14 hours prior to testing to allow the epoxy to cure.

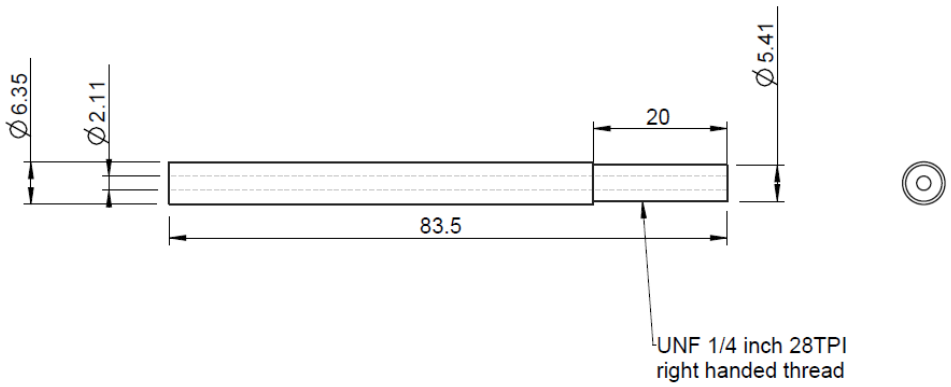

Fig. 7 Injection tube design

Once the injection tube was in position, the 20 mm of thread was wrapped in high-density polytetrafluoroethylene (PTFE) thread tape, designed to hold pressures of up to 68.9 MPa. Dental paste was applied to the top surface of the specimen with the injection tube. The axial platen was then hand screwed onto this injection tube until the faces met, before the dental paste hardened (see Fig. 8). The dental paste sealed the platen and specimen interface and filled any small pores in the surface of the specimen to ensure uniform load transfer.

Fig. 8 Axial platen and specimen connected

The fluid used for these experiments was distilled water, where 40 mL of black food colouring was added to 4 litres of distilled water (at a volumetric ratio of 1 to 100). The black food colouring was used to make the fluid more noticeable if there was a leak and to trace the hydraulic fractures.

The testing procedure was as follows:

1. Using a syringe, the internal cavity inside the platen and the specimen was filled with the coloured distilled water prior to connecting the load platen to the syringe pump (Teledyne Isco 65HP High Pressure Syringe Pump).
2. When connecting the syringe pump line to the load platen, the pump was set at a constant flow rate of 1 mL per minute and then hand tightened to reduce the amount of air trapped during the connection process. Once the connection was tightened with a spanner the syringe pump was stopped immediately.
3. A spherical seat was aligned on the top surface of the axial platen prior to axial loading.
4. The data acquisition server was set to record before the axial load and confining pressures were applied (see Fig. 9). The axial load was then increased to approximately 1.0 kN. The Hoek cell was hand pumped to 0.5 MPa and then the pressure maintainer was enabled. The loading rate was 0.03 MPa per second in order to reach the desired stress level within 5 to 10 minutes. The axial stress and

confining pressure were increased at the same rate until the desired lower value was reached. If the axial stress was larger than the confining pressure, then the Hoek cell pressure maintainer tracked the axial stress until the maximum confining pressure target value was reached, where the axial stress was determined by the load dividing by the average cross-section. If the confining pressure target was larger than the axial stress target, then approximately 1.0 kN before the maximum load was reached the pressure maintainer was changed to the preset rate of 0.03 MPa per second.

5. Once the Hoek cell and the axial stress reached their target values, the distilled water was pumped into the specimen at a constant flow rate of 5 mL per minute. This was chosen to produce an average pressurization rate of approximately 1 MPa per second. The pressure and cumulative volume from the syringe pump were recorded during each test, in addition to the external stress conditions.

Fig. 9 Hydraulic fracturing setup

Under reverse faulting stress conditions (where the confining stress is greater than the axial stress), the fluid pressure causes the specimen with a pre-existing notch to split into two pieces, fracturing approximately horizontally. The specimen did not split into two pieces under normal faulting stress conditions (where the axial stress is greater than the confining stress), since the platens provided enough frictional resistance to inhibit this process from occurring. In this case, the fracture propagated approximately vertically (see Fig. 10 for an example).

Fig. 10 Fracturing of specimen number 14 with dip angle of 60°, under normal faulting conditions (initial normal stress of approximately 10 MPa, and initial shear stress of approximately 1.5 MPa)

Since the specimens tested under reverse faulting stress conditions fractured into two halves, the half without the injection tube attached was used to map the fracture propagation surfaces. These surfaces were digitized using the Autodesk Memento software. The digitization process requires a maximum of 250 photos taken at different vantage points around the specimen.

In theory, each quadrant of the fracture propagation surface should be the mirror image of each other, i.e., there are two perpendicular vertical symmetry planes. One plane is along the apex of the circular crack and the axis of the borehole, and the other is perpendicular to this plane. Once the fracture propagation surfaces were digitized, the four surfaces corresponding to the four quadrants were averaged. The mean surface thus derived is then used for comparison with the numerical analyses.

3 Theory and calculations

In the following sections, the analytical procedure to calculate the initial fracture propagation steps from the circular crack and the numerical method to model the subsequent fracture propagation surfaces are discussed. The analysis also provides a method to assess the breakdown pressures for hydraulic fracturing.

3.1 Problem setup

Consider a circular crack with a radius of a and orientated with a normal vector $\bar{v}_n$ in a rock block subjected to three compressive remote principal stresses. The crack is internally pressured by fluid pressure P. The three principal effective stresses: σ'_x, σ'_y and σ'_z are orientated along the *x*, *y* and *z* axes, respectively (Fig. 11). Note that in the case of using a Hoek cell to apply the lateral stress to the cylindrical specimen σ'_x, and σ'_y are equal. The influence of the borehole was not considered, since its radius of approximately 3.175 mm was small compared with the radius of the circular crack, approximately of 10 mm.

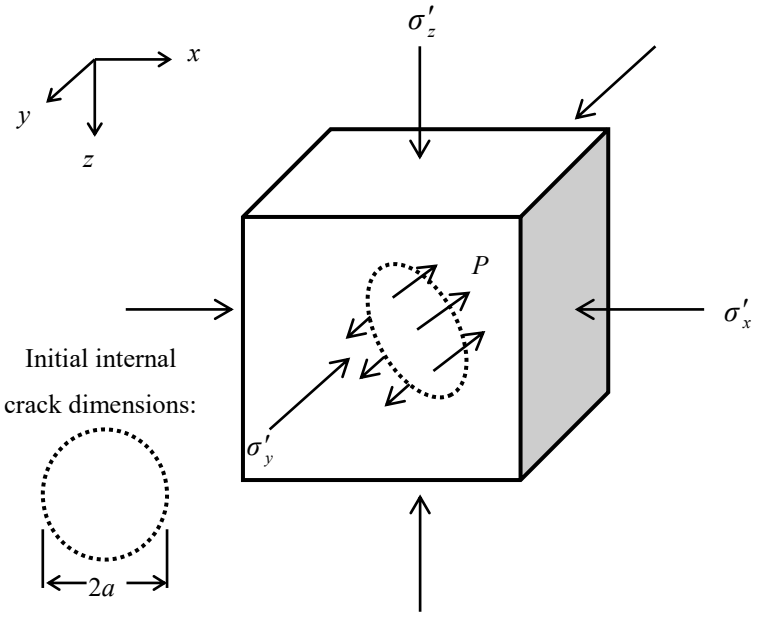

Fig. 11 Problem formulation

3.2 Analytical analysis

The following theory provides the details to analyse the stress intensity factors of a circular crack (which was a close representation to the notch in the experiments) and the corresponding stress distribution around the crack front. It is assumed that there are no time dependent effects, i.e. the breakdown pressure is independent from the rate of loading. This assumption was based on the work of Zoback *et al.* [2], which indicted that under constant flow rate experiments, there are no time dependent effects on breakdown pressure of intact rock.

The pre-existing crack affects the local stress distribution. The stress distribution can be obtained once the stress intensity factors are known. The stress intensity factors can be

determined by the net pressure on the crack face and the shear stress from the external (compressive) stresses. Under the assumption of LEFM, the stress intensity factors can be used as a means to determine the internal pressure when the crack will propagate unstably, and the direction of the fracture propagation.

It is important to be able to predict the breakdown pressures of pre-existing cracks with different shear stresses since this will also determine the initial propagation fracture geometry. In general, pre-existing in-situ cracks are subjected to the action of shear stresses due to the unequal lateral and vertical stresses.

3.2.1 Stress intensity factors for a circular internally pressurized crack

The stress intensity factors for the considered configuration (see Fig. 11 and Fig. 12) can be evaluated using the formulations outlined by Tada *et al.* [26].

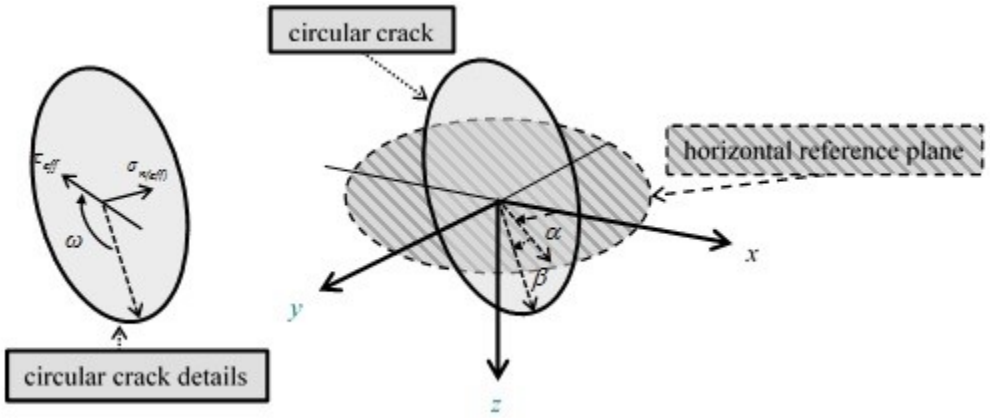

Fig. 12 Net pressure $\sigma_{n(eff)}$, shear stress τ_{eff}, shear angle ω, dip direction α, and dip angle β definitions

Note, in this paper the shear angle ω is defined on the crack plane, clockwise around the normal vector in the positive *z* axis direction, following the system used in FRANC3D [9]. Since Tada *et al.* [26] defined the shear angle ω clockwise around the negative *z* direction, these $K_{II}(\varphi)$ and $K_{III}(\varphi)$ values must be modified accordingly (by multiplying by negative one) to obtain the stress intensity factors consistent to the definitions used in FRANC3D. Using the notations from Rahman *et al.* [27], the stress intensity factors can be expressed in the following general forms:

$$K_I(\varphi) = 2\sqrt{\frac{a}{\pi}}\sigma_{n(eff)} \tag{1}$$

$$K_{II}(\varphi) = -\frac{4\cos(\varphi-\omega)}{(2-\upsilon)}\sqrt{\frac{a}{\pi}}\tau_{eff}$$

$$K_{III}(\varphi) = \frac{4(1-\upsilon)\sin(\varphi-\omega)}{(2-\upsilon)}\sqrt{\frac{a}{\pi}}\tau_{eff}$$

The normal unit vector $\bar{v}_n$ of the crack can be calculated from the dip direction α, and dip angle β, of the crack plane (see Fig. 12), as shown in Eq. (2). The dip direction here is defined as the clockwise rotation angle around *z* (facing downwards) from the positive *x* axis.

$$\bar{v}_n = \begin{bmatrix} l \\ m \\ n \end{bmatrix} = \begin{bmatrix} \cos(90°-\beta)\cos(\alpha) \\ \cos(90°-\beta)\sin(\alpha) \\ \sin(\beta-90°) \end{bmatrix} \tag{2}$$

Young and Budynas [28] published expressions to calculate the normal and shear stresses on a plane using the normal vector (l,m,n) for a given external three dimensional stress configuration. Since it is assumed that σ'_x, σ'_y and σ'_z are the effective principal stresses, then τ_{xy}, τ_{yz} and τ_{xz} are equal to zero. Therefore, for our system, their expressions for normal and shear stresses on a plane can be simplified:

$$\begin{aligned} \sigma_{n(external)} &= \sigma'_x l^2 + \sigma'_y m^2 + \sigma'_z n^2 \\ \tau &= \sqrt{(\sigma'_x l)^2 + (\sigma'_y m)^2 + (\sigma'_z n)^2 - \sigma_{n(external)}{}^2} \end{aligned} \tag{3}$$

where the directional cosines of the shear vector are reduced to the following:

$$\begin{bmatrix} l_\tau \\ m_\tau \\ n_\tau \end{bmatrix} = \frac{1}{\tau}\begin{bmatrix} (\sigma'_x - \sigma_{n(external)})l \\ (\sigma'_y - \sigma_{n(external)})m \\ (\sigma'_z - \sigma_{n(external)})n \end{bmatrix} \tag{4}$$

The shear angle ω is the angle between the shear direction, Eq. (4), and the vector obtained by projecting the dip direction on the crack plane, Eq. (5):

$$\begin{bmatrix} l_o \\ m_o \\ n_o \end{bmatrix} = \begin{bmatrix} \cos(\beta)\cos(\alpha) \\ \cos(\beta)\sin(\alpha) \\ \sin(\beta) \end{bmatrix} \tag{5}$$

and can be calculated as:

$$\omega = \arccos\left(\frac{l_\tau l_o + m_\tau m_o + n_\tau n_o}{\sqrt{l_\tau{}^2 + m_\tau{}^2 + n_\tau{}^2}\sqrt{l_o{}^2 + m_o{}^2 + n_o{}^2}}\right) \tag{6}$$

The internal fluid pressure P, affects the effective net pressure $\sigma_{n(eff)}$, and can be calculated as:

$$\sigma_{n(eff)} = P - \sigma_{n(external)} = P - \left(\sigma'_x l^2 + \sigma'_y m^2 + \sigma'_z n^2\right) \tag{7}$$

The reason the effective net pressure can be used for the mode I stress intensity factors is because the internal pressure has more influence on the stress conditions around the crack front the closer the point of consideration is to that edge. This concept of net pressure equates to mode I and II stress intensity factors, because, by definition, this value is the tangential stress value multiplied by $\sqrt{2\pi r}$ as the point of consideration along the plane of the crack front approaches the edge of the crack. See Fig. 13 for the definition of the stresses on an element near the crack front and Eq. (8) for the definition of mode I, II and III stress intensity factors.

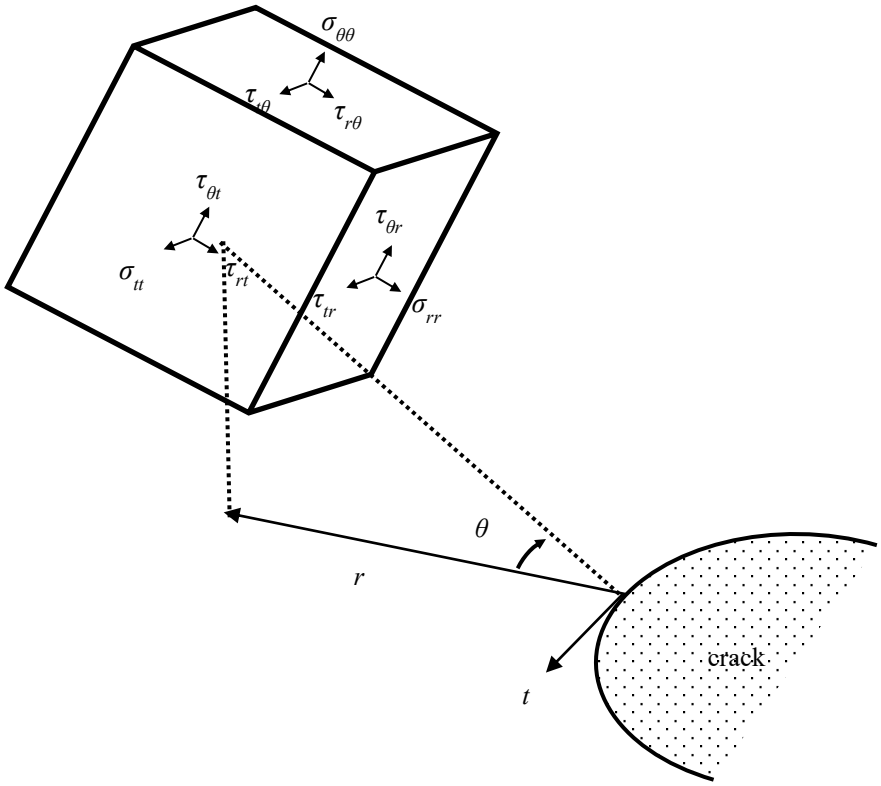

Fig. 13 Stress on an element near the crack front

The internal pressure has the greatest influence on this tangential stress, inside the crack and inside the material, just in front of the crack edge. Therefore, the net pressure is considered to approximate the stress intensity factors for mode I for a pressurised crack with external compressive stresses.

$$K_I = \lim_{r\to 0} \sigma_{\theta\theta}(r,t,\theta=0)\sqrt{2\pi r}$$
$$K_{II} = \lim_{r\to 0} \tau_{r\theta}(r,t,\theta=0)\sqrt{2\pi r} \quad (27)$$
$$K_{III} = \lim_{r\to 0} \tau_{t\theta}(r,t,\theta=0)\sqrt{2\pi r}$$

Since the shear resistance τ_r, for the case of a crack opened by the fluid pressure is very small compared to the shear stress (as crack surfaces are not in contact and there is only small frictional resistance due to fluid viscosity), it can be neglected and therefore the effective shear stress becomes:

$$\tau_{eff} = \tau - \tau_r = \sqrt{(\sigma'_x l)^2 + (\sigma'_y m)^2 + (\sigma'_z n)^2 - \sigma_{n(external)}{}^2} \quad (9)$$

The reasoning is the same for the mode II and III stress intensity factors, since the effective shear stress has the most influence on the radial shear component $\tau_{r\theta}$, and tangential shear component $\tau_{t\theta}$, around the crack front the closer the point of consideration is to that edge. This concept of effective shear stress equates to mode II and III stress intensity factors because, by definition, these values are the radial shear and tangential shear components, respectively, multiplied by $\sqrt{2\pi r}$ as the point of consideration along the plane of the crack front approaches the edge of the crack. The effective shear stress has the greatest influence on these stresses, inside the crack and inside the material, just in front of the crack edge. Note, the opposing shear or tearing stress components are negligible compared with the stresses used in this work. This concept could also be applied to mode II and III with scenarios using high viscosity fluid, where the shear strength of the fluid is not negligible, and/or having low compressive in-situ stress values.

The purpose for presenting the normal and shear stresses and shear angle using the normal vector of the arbitrarily orientated plane is to provide direct expressions for the stress intensity factors, and to assist producing the first quasi-static propagation step.

3.2.2 Stress distribution in the vicinity of an internally pressurized circular crack

The formulation of Sih and Liebowitz [29] on the stress distribution near a circular crack is used to generate the first quasi-static propagation step (see Fig. 14). These stress definitions are normalized by $\sqrt{\pi}$ to be consistent with the common definition of the stress intensity factor where higher order terms are omitted because of their negligible influence:

$$
\begin{aligned}
\sigma_n &= \frac{K_I(\varphi)}{4\sqrt{2\pi r}}\left[3\cos\left(\frac{\theta}{2}\right)+\cos\left(\frac{5\theta}{2}\right)\right]-\frac{K_{II}(\varphi)}{4\sqrt{2\pi r}}\left[7\sin\left(\frac{\theta}{2}\right)+\sin\left(\frac{5\theta}{2}\right)\right]\\
\sigma_t &= \frac{K_I(\varphi)}{\sqrt{2\pi r}}2\upsilon\cos\left(\frac{\theta}{2}\right)-\frac{K_{II}(\varphi)}{\sqrt{2\pi r}}2\upsilon\sin\left(\frac{\theta}{2}\right)\\
\sigma_z &= \frac{K_I(\varphi)}{4\sqrt{2\pi r}}\left[5\cos\left(\frac{\theta}{2}\right)-\cos\left(\frac{5\theta}{2}\right)\right]-\frac{K_{II}(\varphi)}{4\sqrt{2\pi r}}\left[\sin\left(\frac{\theta}{2}\right)-\sin\left(\frac{5\theta}{2}\right)\right]\\
\tau_{tz} &= \frac{K_{III}(\varphi)}{\sqrt{2\pi r}}\cos\left(\frac{\theta}{2}\right)\\
\tau_{zn} &= -\frac{K_I(\varphi)}{4\sqrt{2\pi r}}\left[\sin\left(\frac{\theta}{2}\right)-\sin\left(\frac{5\theta}{2}\right)\right]+\frac{K_{II}(\varphi)}{4\sqrt{2\pi r}}\left[3\cos\left(\frac{\theta}{2}\right)+\cos\left(\frac{5\theta}{2}\right)\right]\\
\tau_{nt} &= -\frac{K_{III}(\varphi)}{\sqrt{2\pi r}}\sin\left(\frac{\theta}{2}\right)
\end{aligned}
\tag{10}
$$

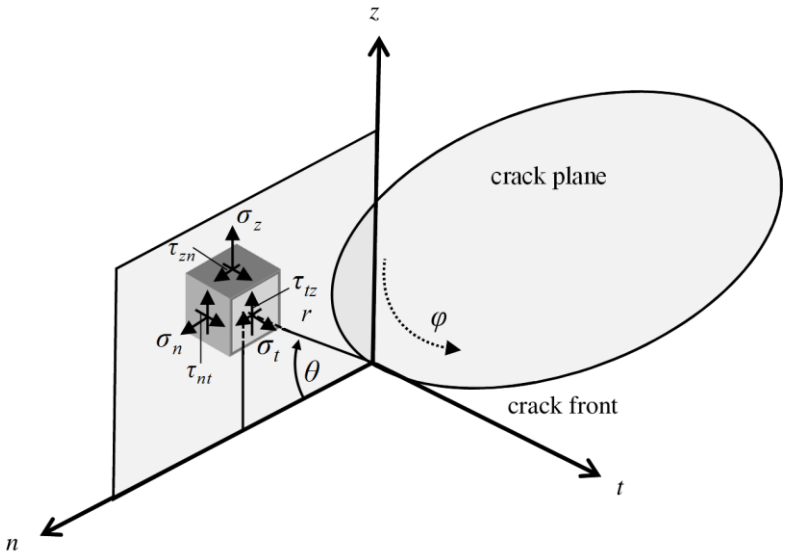

Fig. 14 Rectangular stress components in a plane normal to the crack border

Note that in Fig. 14 the angle θ is clockwise around the *t* axis. The conventional definition for this angle θ is applied (anticlockwise around the *t* axis) to convert the local stresses at the crack front in Eq. (10) from a cylindrical coordinate system to a spherical coordinate system using a rotation matrix i.e.:

$$
\begin{aligned}
\sigma_r &= \frac{1}{\sqrt{2\pi r}}\left[K_I(\varphi)\left(2\cos\left(\frac{\theta}{2}\right)-\cos^3\left(\frac{\theta}{2}\right)\right)+K_{II}(\varphi)\left(\sin\left(\frac{\theta}{2}\right)-3\sin^3\left(\frac{\theta}{2}\right)\right)\right]\\
\sigma_t &= \frac{2\upsilon}{\sqrt{2\pi r}}\left[K_I(\varphi)\cos\left(\frac{\theta}{2}\right)-K_{II}(\varphi)\sin\left(\frac{\theta}{2}\right)\right]
\end{aligned}
\tag{11}
$$

$$\sigma_\theta = \frac{\cos^2\left(\frac{\theta}{2}\right)}{\sqrt{2\pi r}}\left[K_I(\varphi)\cos\left(\frac{\theta}{2}\right) - 3K_{II}(\varphi)\sin\left(\frac{\theta}{2}\right)\right]$$

$$\tau_{rt} = \frac{K_{III}(\varphi)}{\sqrt{2\pi r}}\sin\left(\frac{\theta}{2}\right)$$

$$\tau_{r\theta} = \frac{\cos\left(\frac{\theta}{2}\right)}{2\sqrt{2\pi r}}\left[K_I(\varphi)\sin\theta + K_{II}(\varphi)(3\cos\theta - 1)\right]$$

$$\tau_{t\theta} = \frac{K_{III}(\varphi)}{\sqrt{2\pi r}}\cos\left(\frac{\theta}{2}\right)$$

The maximum tangential stress σ_θ, is used to determine the radial fracture propagation angles $\theta_c(\varphi)$ for the first quasi-static propagation step. These radial fracturing angles are calculated from mode I, $K_I(\varphi)$, and II, $K_{II}(\varphi)$, stress intensity factors. The following expression determines the radial fracture angles:

$$\theta_c(\varphi) = \begin{cases} 0^\circ & if\ K_{II}(\varphi) = 0 \\ 2\arctan\left[\dfrac{K_I(\varphi) \pm \sqrt{K_I(\varphi)^2 + 8K_{II}(\varphi)^2}}{4K_{II}(\varphi)}\right] & if\ K_{II}(\varphi) \neq 0 \end{cases} \quad (12)$$

These fracturing angles are evaluated via the following expression:

$$\sigma_\theta\sqrt{2\pi r} = \cos^2\left(\frac{\theta_c(\varphi)}{2}\right)\left[K_I(\varphi)\cos\left(\frac{\theta_c(\varphi)}{2}\right) - 3K_{II}(\varphi)\sin\left(\frac{\theta_c(\varphi)}{2}\right)\right] \quad (13)$$

To simplify the analysis, the fracture front after the first propagation step was assumed to form a planar polygon. This planar fracture front was evaluated and incorporated into FRANC3D during the numerical modelling process (see Appendix A for details of the calculation).

3.3 Numerical analysis using FRANC3D

The commercial software FRANC3D [9] was utilized to model the fracture propagation surfaces corresponding to the experiments. The surface was generated by setting the pressure inside the propagating crack to the breakdown pressure.

The same maximum tangential stress criterion was used to determine the fracture propagation surface at each quasi-static step. FRANC3D was used in all subsequent steps to calculate the stress intensity factors. FRANC3D links with various finite element commercial software packages (ANSYS, NASTRAN, and ABAQUS). The stress and displacements are solved, in this case, within ABAQUS. These modelled stress and

displacements, from ABAQUS, around the crack front, are converted to the stress intensity factors for mode I, II and III in FRANC3D, using the M-integral method [30].

To simplify the numerical analyses, it was assumed that the small 6.35 mm diameter borehole had little influence on the final propagation surface. The borehole was not considered in the numerical simulations at this stage. However, the closer the borehole size is to the fracture size the more influence it would have on the propagation surface. For future works, it is suggested to model the experiments with the consideration of the influence from the borehole.

As discussed in Section 3.2.2, the first propagation front location was calculated and inserted into the model. This was necessary since the fracture propagation algorithm in FRANC3D is problematic when considering a circular crack. To calculate this planar propagation front, all the radial fracture angles were used. The increment length inc, for these steps was 20% of the measured initial crack radius, corresponding to the point of maximum stress intensity factor for mode II. This was approximately the smallest possible increment length to generate a suitable finite element mesh of the kinked fracture.

Subsequent propagation steps used the inbuilt FRANC3D propagation algorithm. The radial increments $inc_{FRANC3D}(\varphi)$ were hence determined by the relative difference in mode I stress intensity factors $K_I(\varphi)$ and the median mode I stress intensity factor $K_{I(median)}$ to the power of a factor n:

$$inc_{FRANC3D}(\varphi) = a_{median}\left(\frac{K_I(\varphi) - K_{I(median)}}{K_{I(median)}}\right)^n \tag{14}$$

The median increment step size a_{median}, was set to 20% of the initial crack radius and the factor n, was set to one. FRANC3D provided functioning crack fronts from the propagation algorithm in the subsequent quasi-static steps, since the mode I stress intensity factors were no longer constant around the front of the kinked crack. By following this method, the propagation surfaces of the experiments could be modelled and compared.

4 Results and discussion

This section is divided into two parts; in the first part, the experimental and numerical fracture propagation surfaces for three examples are compared, and in the second part, the breakdown pressures for all experiments are analysed.

4.1 Comparison of fracture propagation surfaces

Three examples of fracture propagation surfaces were chosen to be presented below with the consideration that their original circular notches (each replicating a crack) were at the same dip angle β, of 30° for easier comparisons. These three examples are summarized in Table 6. Note that the axial and confining stresses are those obtained from the experiments when the breakdown pressure was reached.

Table 6 Summary of fracture propagation surface experiment examples

Specimen number	Dip angle (°)	Crack radius (mm)	Confining pressure (MPa)	Axial stress (MPa)	Normal stress (MPa)	Shear stress (MPa)	Maximum internal pressure (MPa)
7	30	9.96	11.754	9.443	10.021	1.001	24.273
27	30	9.93	12.629	9.135	10.008	1.513	22.431
22	30	9.99	14.375	8.581	10.030	2.509	23.518

These fracture propagation surfaces were modelled using FRANC3D. The mechanical parameters measured from the experiments listed above were used as inputs for the models. A cuboid model where the circular cross-section inscribes the surfaces of the rectangular prism has the size as the cylindrical specimen cross-section. Hence, the *x* and *y* dimensions of the cuboid were 63.5 mm, and the *z* dimension was 127 mm. The boundary conditions of these models were chosen to prevent rotation of the specimen, without restricting movement across the faces. Therefore, four corners were pinned in the negative *z* direction and likewise in the negative *x* and *y* directions (see Fig. 15).

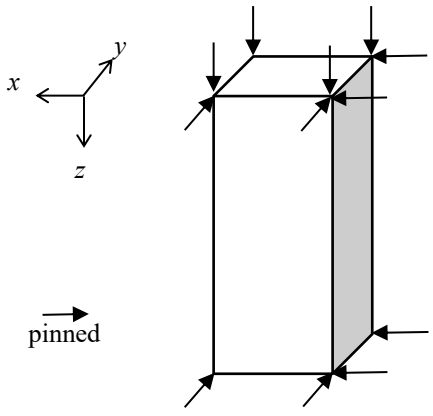

Fig. 15 Boundary conditions

For specimen number 7 the propagation surfaces align well (see Fig. 16 and Fig. 17 for the comparison). Note that the colour legends in the following figures (Fig. 16 to Fig. 21) correspond to the perpendicular distances to the plane of interest. The main discrepancy occurred at the outer surface of the specimen, where the fracture broke through. This may be caused by the sudden drop in pressure as the fracture propagates through the specimen

surface. This drop in pressure would realign the fracture propagation surface more towards being perpendicular to the *z* (minor principal stress) direction.

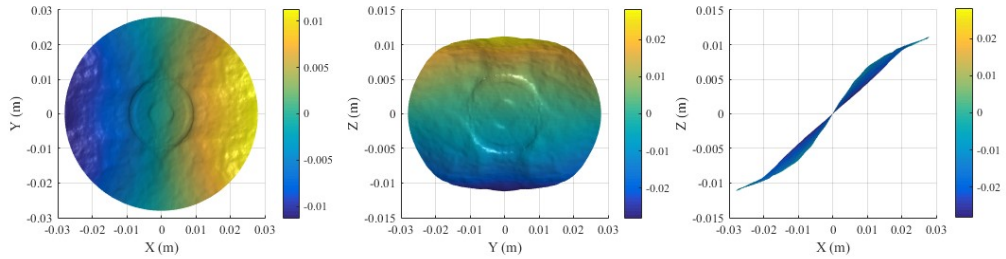

Fig. 16 Experimental fracture propagation surface for specimen number 7

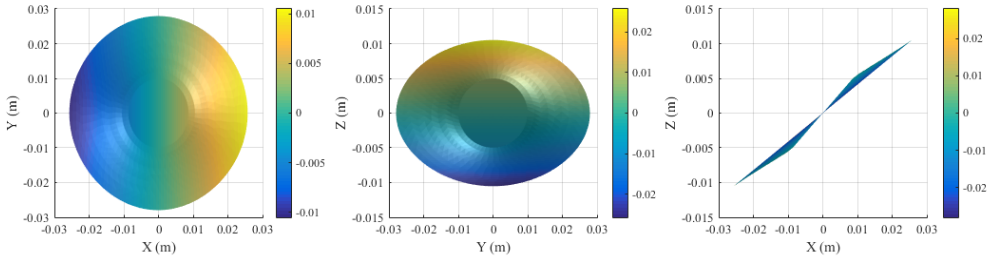

Fig. 17 Modelled fracture propagation surface for specimen number 7

For specimen number 27 the modelled and experimental fracture propagation surfaces align reasonably well (see Fig. 18 and Fig. 19 for the comparison). In this case, there is a large deviation between the two surfaces at the boundary of the specimen. As discussed above, this may be also caused by the sudden drop in pressure as the fracture propagates through the specimen surface. This drop in pressure would realign the fracture propagation surface more towards being perpendicular to the *z* (minor principal stress) direction.

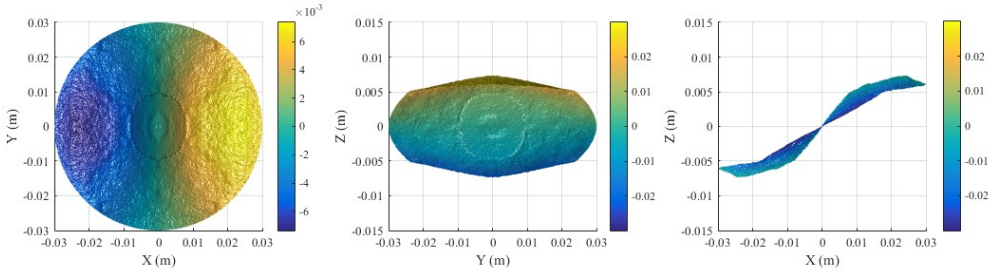

Fig. 18 Experimental fracture propagation surface for specimen number 27

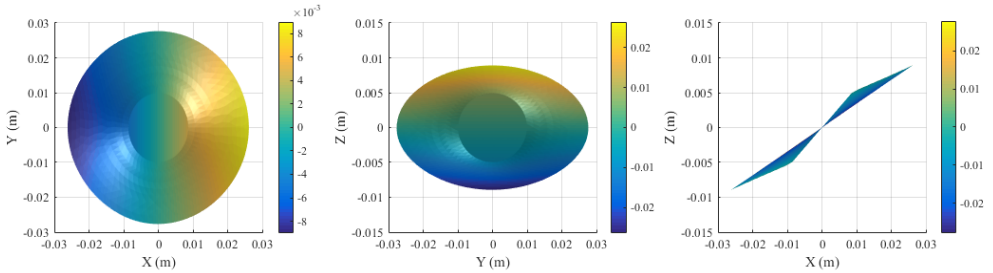

Fig. 19 Modelled fracture propagation surface for specimen number 27

For specimen number 22, the experimental and modelled fracture propagation surfaces align reasonably well (see Fig. 20 and Fig. 21 for the comparison).

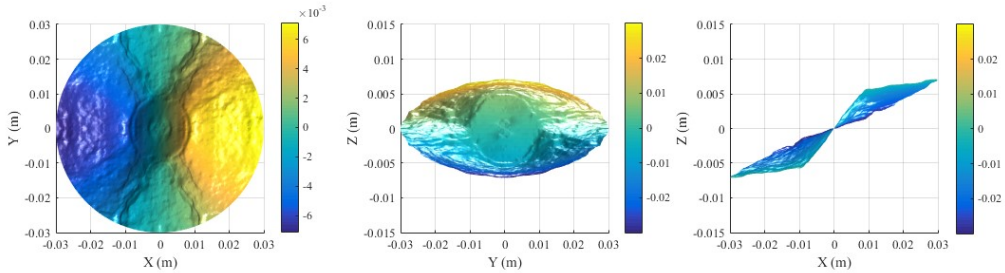

Fig. 20 Experimental fracture propagation surface for specimen number 22

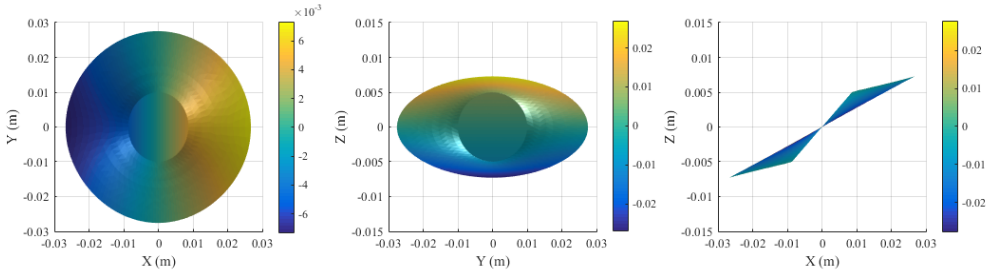

Fig 7 Modelled fracture propagation surface for specimen number 22

As the initial shear stress on the circular crack increases, there is a trend that with similar breakdown pressures, the fracture propagation surfaces become flatter. The greater the shear stress on the initial circular crack, the higher the mode II stress intensity factor, and

according to the maximum tangential stress criterion, the radial angle of fracturing increases.

In Appendix B, the internal pressure and external stresses versus time graphs are provided for the discussed examples (see Fig. B.1 to Fig. B.6). These graphs were provided for use in supplementary studies. There are two graphs per experiment. One shows the stress versus time graphs from -10 to 50 seconds, where zero seconds is taken as when the internal pressure is 1.0 MPa. The other graph shows the internal pressure versus time after breakdown.

4.2 Breakdown pressures

The net normal pressure and shear stress on the notch (replicating a crack) face were converted to mode I and II stress intensity factors at the time of fracturing for each experimental configuration (see Fig. 22), using Eq. (1). The mode I stress intensity factors are therefore equivalent to the fracture toughness of the material. See Table C.1 for individual results of the hydraulic fracturing experiments. Note that the provided confining and axial stresses are those when the maximum internal fluid pressure was reached. The apparent difference in the average mode I stress intensity factor for each set of mode II stress intensity factors is attributed to the different material properties produced from different batches of concrete.

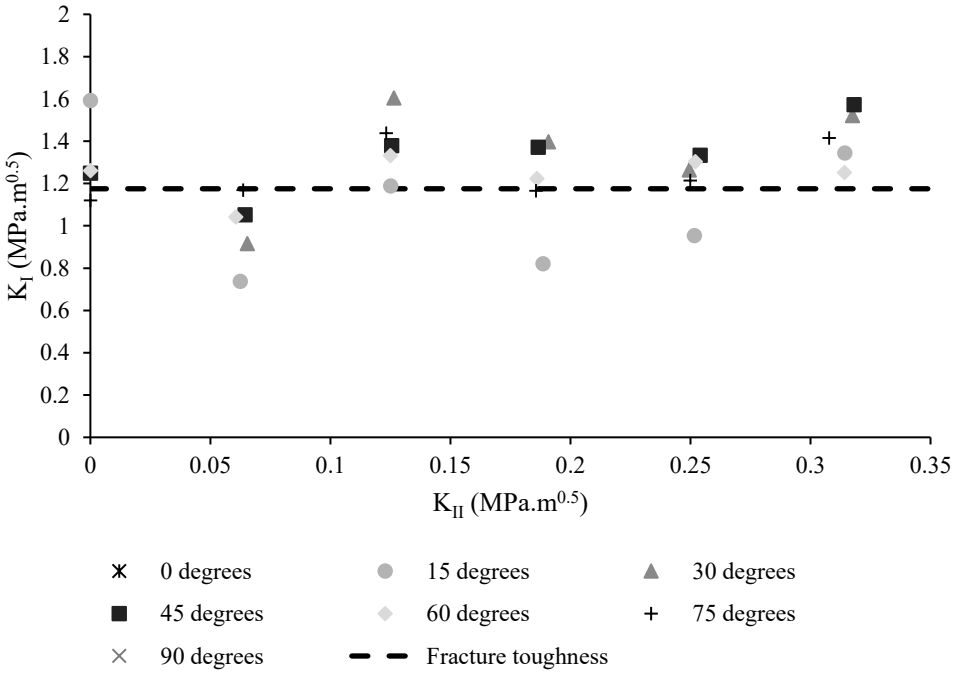

Fig. 22 Mode I versus mode II stress intensity factors from hydraulic fracturing experiments

The mode I stress intensity factors at the time of fracturing appear constant (see Fig. 22) within the range of mode II stress intensity factors tested. It is expected however, that the

mode I stress intensity factors at the time of fracturing will gradually decrease with increasing magnitude of mode II stress intensity factors. This relationship is anticipated since the mode I versus mode II stress intensity factors at failure envelope has been reported for many brittle materials [31-34]. The histogram for the measured mode I stress intensity factors at failure have a normal distribution (see Fig. 23). Although, a normal distribution of measured mode I stress intensity factors at failure would only hold within the range of mode II stress intensity factors tested.

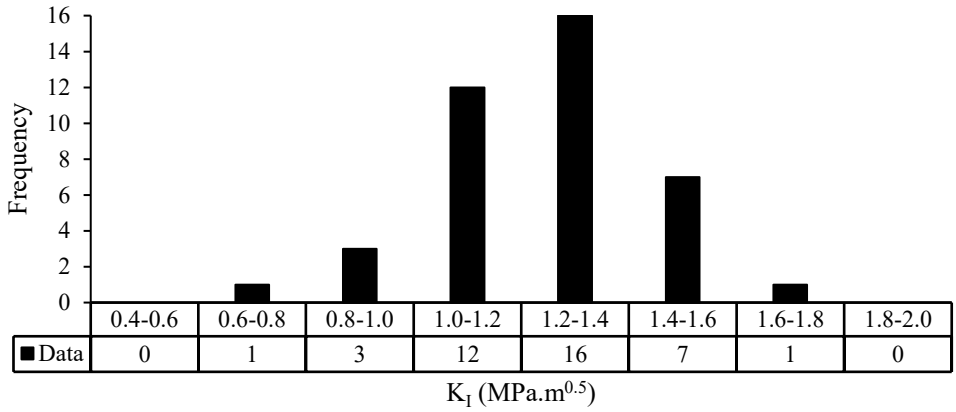

Fig. 23 Mode I stress intensity factor distribution for hydraulic fracturing experiments

The average mode I stress intensity factor was 1.24±0.20 MPa$\sqrt{\text{m}}$, which was comparable to the measured mode I fracture toughness K_{Ic} value of 1.18±0.05 MPa$\sqrt{\text{m}}$. The influence of the mode II stress intensity factors on the mode I stress intensity factor at failure, under the shear stress values tested, is minimal. Because of the minimal influence of the mode II stress intensity factor it is therefore sufficient to calculate the breakdown pressure P_f, for a circular crack tested under these shear stress values, when the mode I stress intensity factor, from Eq. (1), is equal to the mode I fracture toughness:

$$P_f = \sigma_n + \frac{K_{Ic}}{2}\sqrt{\frac{\pi}{a}} \tag{15}$$

The breakdown pressure values used in the modelling of fracture propagation surfaces were the measured quantities. Therefore, Eq. (15) was not used in these models, but this expression provides an accurate estimate of the breakdown pressure values in the presented experiments. Further work is needed to investigate the effects of greater shear stresses on the failure characteristics of pressurized circular notches (i.e., to replicate cracks).

5 Conclusions

In this research, the effects of circular cracks intersecting a pressurized borehole section on the breakdown pressures and the resultant fracture propagation surfaces have been investigated. Some important findings are summarized below:

- The breakdown pressures of circular notches, designed to replicate a crack, under the shear stress conditions tested, can be reliably predicted by the radius of the crack, the normal stress on the plane of the crack and the fracture toughness of the material, using a LEFM approach.
- The fracture propagation analysis method proposed gives results that compare well with the experimental fracture propagation surfaces. Therefore, it is acceptable to use the maximum tangential stress criterion to model fracture propagation in hydraulic fracturing.
- The greater the shear stress is on the plane of the circular crack, the shorter distance it takes for the fracture to re-orientate to be perpendicular to the minor principal stress direction. The magnitude of shear stress is increased when there is a greater difference between the external principal compressive stresses.
- For all experiments, the external stress conditions determine the direction of the fracture propagation surface. Specifically, the fracture propagation plane will eventually realign perpendicular to the minor principal stress direction.

Further work is needed to model the variation of the internal pressure versus time during the hydraulic fracturing process. This could then be used to extrapolate the experimental results to larger regions. In addition, as this work only considers the influence of a single circular notch, representing a crack, it is important to determine the influence of two or more cracks on the breakdown pressures and fracture propagation surfaces.

Acknowledgements

The authors would like to thank Adam Ryntjes and Simon Golding for their assistance with the laboratory setup and experiments.

Appendix

A. The crack propagation step when the crack is circular

The subsequent planar crack propagation front can be defined using all the corresponding crack propagation angles $\theta_c(\varphi)$ from the previous crack front, even if the propagation process kinks the crack. See Fig. A.1 for the geometric description of variables used to model the crack front.

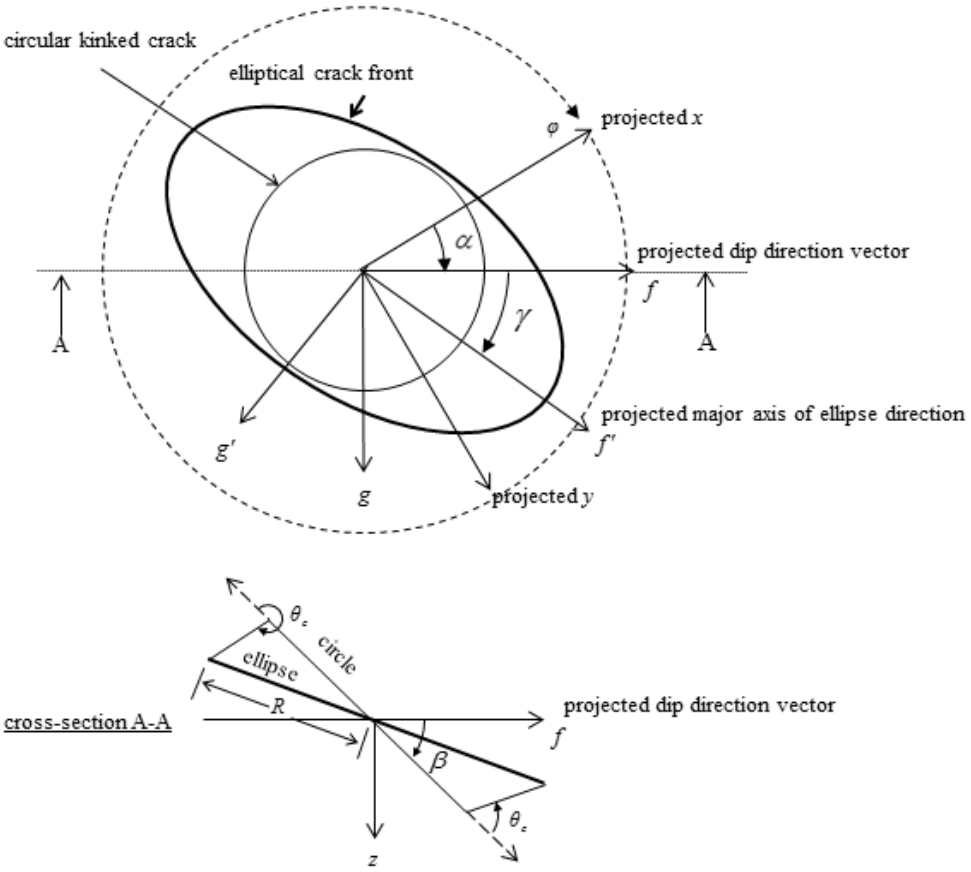

Fig. A.1 Geometric description of variables used in the calculation of circular crack propagation fronts

To generate a planar crack propagation front, a predefined constant increment value *inc*, is used at two particular points only, which are at $\varphi_{\max}$, corresponding to the maximum mode II stress intensity factor values. These two points are in the shear direction ω, and are 90° from the point φ_{zero}, where the stress intensity factor for mode II is zero, i.e.:

$$\varphi_{\max} = \varphi_{zero} \pm 90° \tag{A.1}$$

According to the maximum tangential stress criterion, at the φ_{zero} point, the crack propagation plane coincides with the initial crack plane, since the mode II stress intensity factor is equal to zero. For a circular crack, stress intensity factors for mode II are equal to zero when the crack front angle is at 90° from the shear angle ω, i.e.:

$$\varphi_{zero} = \omega \mp 90° \tag{A.2}$$

Subsequently, $\varphi_{\max}$ and $\theta_{c(\max)}$ can be calculated and hence a reference point on the crack propagation front can be determined (see Fig. A.2).

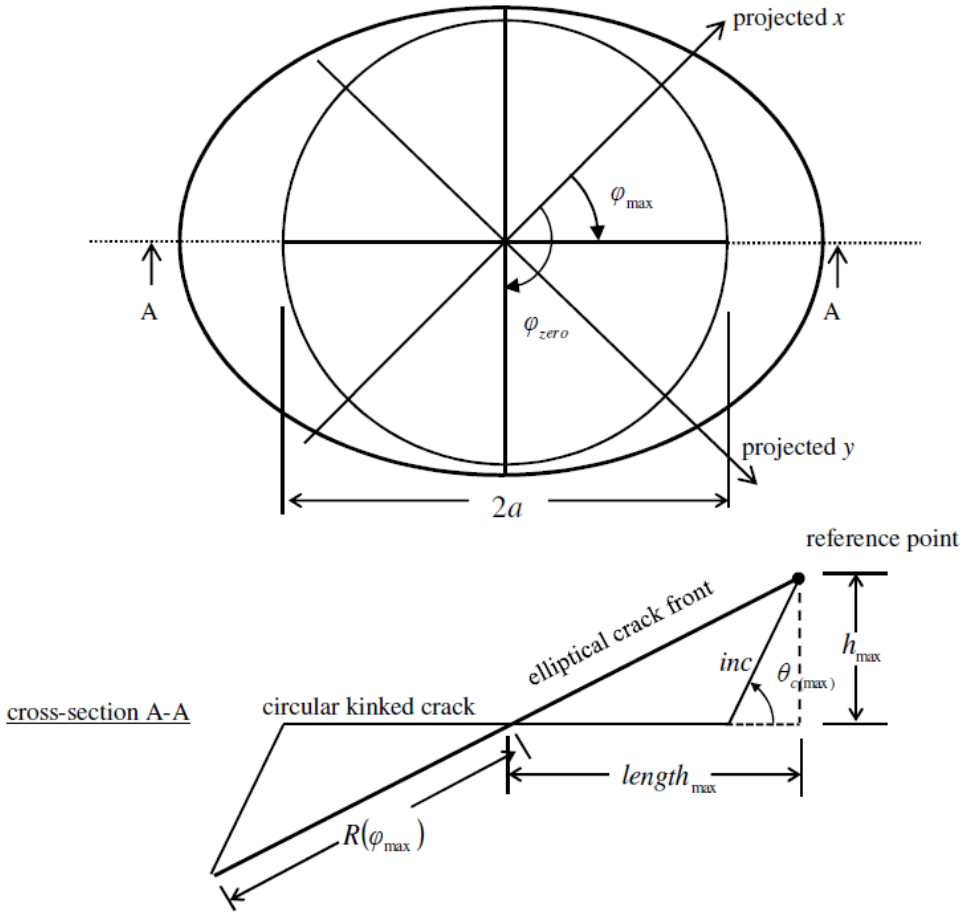

Fig. A.2 Circular to elliptical propagation step diagram

For the convenience of calculating the propagation profile, a local crack plane coordinate system is introduced, where f is in the dip direction of the original crack plane, g is perpendicular to f and on the plane of the circular crack, and h is perpendicular to the crack plane. Therefore, the slope of the crack plane after propagation is $h_{\max}/length_{\max}$ in the $\varphi_{\max}$ direction (see Fig. A.2), which can be calculated as:

$$\frac{h_{\max}}{length_{\max}} = \frac{(inc)\sin(\theta_{c(\max)})}{a + (inc)\cos(\theta_{c(\max)})} \tag{A.3}$$

The other orthogonal local coordinates h from the crack plane for different φ points are calculated as:

$$h(\varphi) = (inc)\sin(\theta_{c(\max)})\cos(\varphi - \varphi_{\max}) \tag{A.4}$$

Therefore, the radial coordinates of the crack front after crack propagation can be calculated from the following expression:

$$length(\varphi) = a + \frac{h(\varphi)}{\tan(\theta_c(\varphi))} \quad \text{if } \theta_c(\varphi) \neq 0° \tag{A.5}$$

When the crack propagation angle is zero, i.e. $\theta_c(\varphi) = 0,$ the crack growth is planar but Eq. A.5 does not evaluate and therefore an approximation is used by averaging the radial coordinates of the neighbourhood points.

The radial lengths from the origin to the subsequent propagation front can then be calculated from the following expression:

$$R(\varphi) = \sqrt{length^2(\varphi) + h^2(\varphi)} \tag{A.6}$$

The local vectors of the subsequent crack front after crack propagation can then be calculated as:

$$\begin{bmatrix} f(\varphi) \\ g(\varphi) \\ h(\varphi) \end{bmatrix} = \begin{bmatrix} length(\varphi)\cos(\varphi) \\ length(\varphi)\sin(\varphi) \\ h(\varphi) \end{bmatrix} \tag{A.7}$$

These coordinates are then transformed to the coordinates in the global system using the following expressions:

$$\begin{bmatrix} x(\varphi) \\ y(\varphi) \\ z(\varphi) \end{bmatrix} = \begin{bmatrix} f(\varphi)\cos(\beta)\cos(\alpha) - g(\varphi)\sin(\alpha) - h(\varphi)\cos(\alpha)\sin(\beta) \\ f(\varphi)\cos(\beta)\sin(\alpha) + g(\varphi)\cos(\alpha) - h(\varphi)\sin(\alpha)\sin(\beta) \\ f(\varphi)\sin(\beta) + h(\varphi)\cos(\beta) \end{bmatrix} \tag{A.8}$$

B. Stress versus time graphs for the fracture propagation surface examples

The graphs of stress versus time recorded in experiments are provided below for the examples of the fracture propagation surfaces discussed in Section 4.1 (see Fig. B.1 to Fig. B.6). Such detailed information, plus the measured values listed in Table C.1, will be very useful for further independent studies.

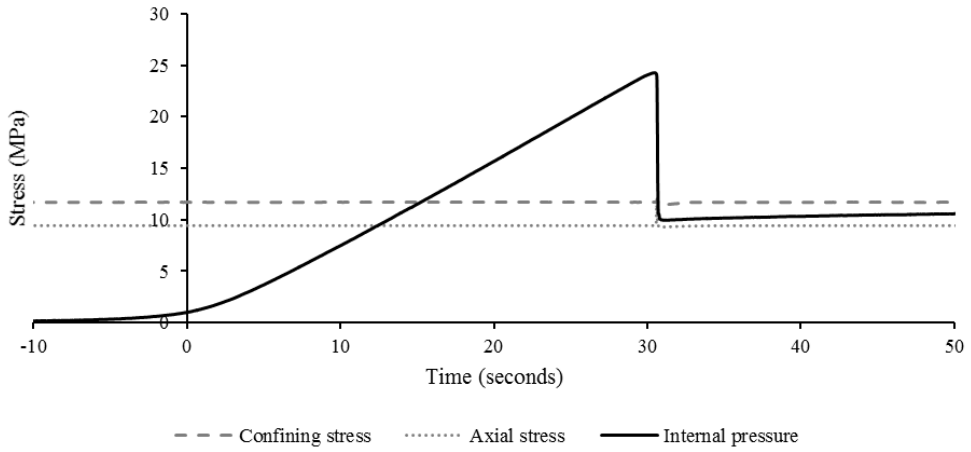

Fig. B.1 Stress versus time for specimen number 7

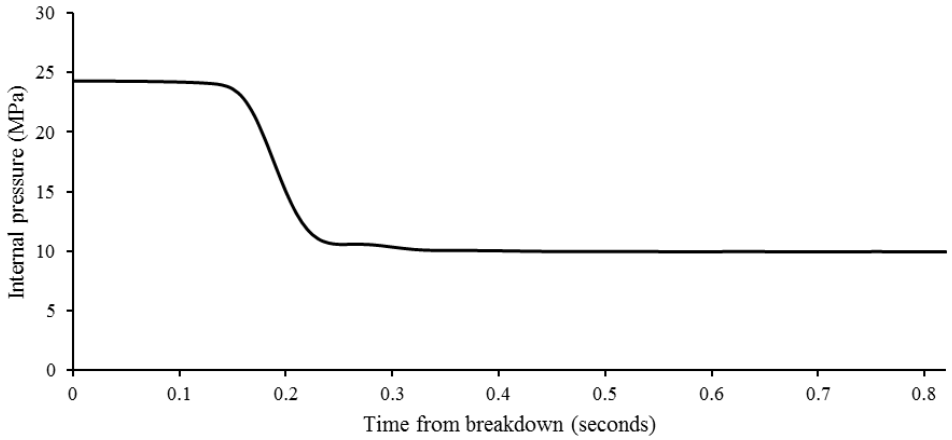

Fig. B.2 Internal pressure versus time after breakdown for specimen number 7

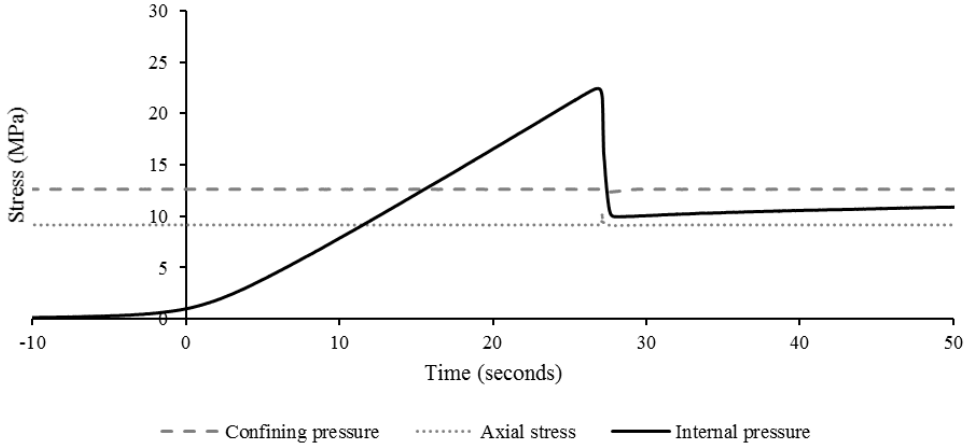

Fig. B.3 Stress versus time for specimen number 27

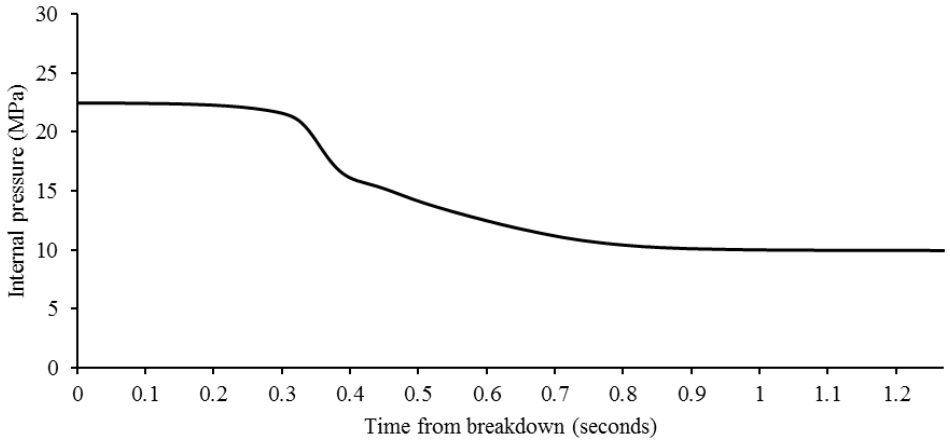

Fig. B.4 Internal pressure versus time after breakdown for specimen number 27

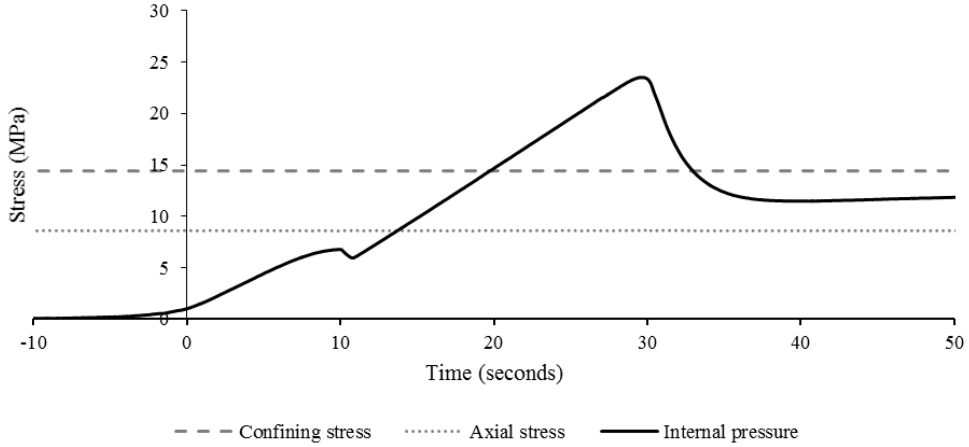

Fig. B.5 Stress versus time for specimen number 22

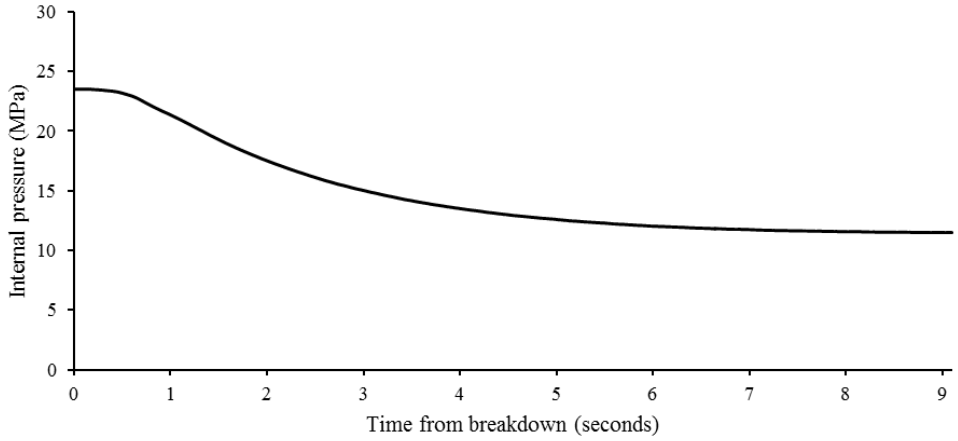

Fig. B.6 Internal pressure versus time after breakdown for specimen number 22

C. Hydraulic fracturing experimental values

Table C.1 Hydraulic fracturing results

Sample number	Dip angle (°)	Hoek cell specimen diameter (mm)	Hoek cell specimen length (mm)	Borehole diameter (mm)	Borehole depth (mm)	Circular notch diameter (mm)	Notch thickness (mm)	Confining pressure (MPa)	Axial stress (MPa)	Normal stress (MPa)	Shear stress (MPa)	Maximum internal pressure|(MPa)
4	0	63.17	127.97	6.16	61.00	19.52	1.64	0.000	0.000	0.000	0.000	9.696
5	0	63.62	127.92	6.24	61.75	19.46	1.67	0.000	0.000	0.000	0.000	10.520
6	0	63.29	128.05	6.27	63.50	19.53	1.63	0.000	0.000	0.000	0.000	10.234
7	0	63.78	125.25	6.27	59.70	19.48	1.69	0.000	0.000	0.000	0.000	11.485
8	0	63.71	123.48	6.26	57.60	19.56	1.76	0.000	0.000	0.000	0.000	13.036
36	15	63.27	124.59	6.18	64.02	19.63	1.71	0.000	0.000	0.000	0.000	14.240
37	30	63.53	124.50	6.38	63.02	20.15	1.32	0.000	0.000	0.000	0.000	11.081
38	45	68.59	127.70	6.50	48.60	19.03	2.12	0.000	0.000	0.000	0.000	11.347
34	60	63.26	127.16	6.45	64.51	18.62	1.87	0.000	0.000	0.000	0.000	11.581
40	75	63.26	127.23	6.47	49.56	18.88	1.79	0.000	0.000	0.000	0.000	10.215
1	90	63.27	126.06	6.50	57.66	19.69	1.40	0.000	0.000	0.000	0.000	10.517
2	90	63.69	129.26	6.45	62.89	19.80	1.42	0.000	0.000	0.000	0.000	10.586
3	90	63.15	123.52	6.42	63.51	19.72	1.42	0.000	0.000	0.000	0.000	9.545
4	90	63.68	132.78	6.52	58.81	19.92	1.51	0.000	0.000	0.000	0.000	12.500
5	90	63.35	128.57	6.41	55.80	19.60	1.36	0.000	0.000	0.000	0.000	11.982
1	15	63.02	127.05	6.18	65.49	19.70	1.62	8.153	10.139	10.006	0.496	16.587
2	30	63.32	121.41	6.18	65.44	20.06	1.37	10.906	9.717	10.014	0.515	18.120
33	45	63.30	127.91	6.32	63.40	19.85	1.48	10.523	9.500	10.012	0.511	19.372
4	60	63.78	126.91	6.20	65.08	19.87	1.25	9.759	10.866	10.036	0.480	19.303
35	75	63.37	125.28	6.47	48.27	19.35	1.68	10.173	8.131	10.036	0.510	20.568
6	15	63.17	128.20	6.17	63.09	19.51	1.25	13.771	9.753	10.022	1.005	20.684
7	30	63.21	129.13	6.15	64.76	19.92	1.29	11.754	9.443	10.021	1.001	24.273
8	45	63.16	128.57	6.00	64.06	19.79	1.31	11.013	9.020	10.016	0.996	22.302
9	60	63.54	128.73	6.11	64.04	19.75	1.38	9.439	11.734	10.013	0.994	21.894
10	75	63.46	126.23	6.14	61.83	19.21	1.57	9.762	13.734	10.028	0.993	23.035
11	15	63.08	129.23	6.18	63.25	19.62	1.29	15.665	9.648	10.052	1.504	17.396
27	30	62.98	128.84	6.45	62.81	19.86	1.45	12.629	9.135	10.008	1.513	22.431
28	45	63.13	130.13	6.39	65.15	19.45	2.07	8.511	11.501	10.006	1.495	22.324
14	60	63.10	129.31	6.12	61.73	19.34	1.47	9.159	12.610	10.022	1.494	21.051
15	75	63.21	129.44	6.20	63.95	18.91	1.48	10.440	4.409	10.036	1.508	20.658
16	15	63.77	125.43	6.18	64.78	19.69	1.23	2.519	10.417	9.888	1.975	18.519
17	30	63.24	123.79	6.11	61.89	19.50	1.24	6.552	11.202	10.039	2.014	21.359
18	45	63.27	123.66	6.09	61.80	19.95	1.38	12.028	8.038	10.033	1.995	21.856
19	60	63.71	120.73	6.09	61.74	19.76	1.40	11.174	6.402	9.981	2.066	21.644

Sample number	Dip angle (°)	Hoek cell specimen diameter (mm)	Hoek cell specimen length (mm)	Borehole diameter (mm)	Borehole depth (mm)	Circular notch diameter (mm)	Notch thickness (mm)	Confining pressure (MPa)	Axial stress (MPa)	Normal stress (MPa)	Shear stress (MPa)	Maximum internal pressure|(MPa)
20	75	63.79	123.90	6.17	62.70	19.42	1.65	10.560	2.494	10.020	2.016	20.938
21	15	63.51	128.54	6.13	64.64	19.65	1.25	19.363	9.346	10.017	2.504	22.031
22	30	63.29	126.94	6.38	63.50	19.98	1.43	14.375	8.581	10.030	2.509	23.518
23	45	63.34	127.02	5.99	64.21	20.11	1.33	12.518	7.504	10.011	2.507	23.909
24	60	63.25	128.59	6.15	64.30	19.87	1.32	8.581	14.330	10.018	2.490	21.142
25	75	63.25	129.27	6.10	60.79	18.99	1.81	9.347	19.327	10.016	2.495	22.890

References

1. Hubbert MK, Willis DG. Mechanics of hydraulic fracturing. *J Am Assoc Pet Geol.* 1957;18(12).

2. Zoback MD, Rummel F, Jung R, Raleigh CB. Laboratory hydraulic fracturing experiments in intact and pre-fractured rock. *Int J Rock Mech Min Sci.* 1977;14(2): 49-58.

3. Zhang GQ, Chen M. Dynamic fracture propagation in hydraulic re-fracturing. *J Pet Sci Eng.* 2010;70(3–4): 266-272.

4. Yan T, Li W, Bi X. An experimental study of fracture initiation mechanisms during hydraulic fracturing. *Pet Sci.* 2011;8(1): 87-92.

5. Sousa JL, Carter BJ, Ingraffea AR. Numerical simulation of 3D hydraulic fracture using Newtonian and power-law fluids. *International Journal of Rock Mechanics and Mining Sciences & Geomechanics Abstracts.* 1993;30(7): 1265-1271.

6. Hossain MM, Rahman MK. Numerical simulation of complex fracture growth during tight reservoir stimulation by hydraulic fracturing. *J Pet Sci Eng.* 2008;60(2): 86-104.

7. Huang K, Zhang Z, Ghassemi A. Modeling three-dimensional hydraulic fracture propagation using virtual multidimensional internal bonds. *Int J Numer Anal Meth Geomech.* 2012;37: 2021-2038.

8. Gupta P, Duarte C. Simulation of non-planar three-dimensional hydraulic fracture propagation. *Int J Numer Anal Meth Geomech.* 2014.

9. Wawrzynek P, Carter B, Ingraffea A. Advances in simulation of arbitrary 3D crack growth using FRANC3D NG. *12th International Conference on Fracture.* Ottawa; 2009.

10. Majer EL, Baria R, Stark M, et al. Induced seismicity associated with Enhanced Geothermal Systems. *Geothermics.* 2007;36(3): 185-222.

11. Zimmermann G, Reinicke A. Hydraulic stimulation of a deep sandstone reservoir to develop an Enhanced Geothermal System: Laboratory and field experiments. *Geothermics.* 2010;39(1): 70-77.

12. Fridleifsson IB, Freeston DH. Geothermal energy research and development. *Geothermics.* 1994;23(2): 175-214.

13. Caineng Z, Guangya Z, Shizhen T, et al. Geological features, major discoveries and unconventional petroleum geology in the global petroleum exploration. *Petroleum Exploration and Development.* 2010;37(2): 129-145.

14. Häring MO, Schanz U, Ladner F, Dyer BC. Characterisation of the Basel 1 enhanced geothermal system. *Geothermics.* 2008;37(5): 469-495.

15. Rogner H-H. An assessment of world hydrocarbon resources. *Annu Rev Energy Environ.* 1997;22: 217-262.

16. Arzúa J, Alejano LR. Dilation in granite during servo-controlled triaxial strength tests. *Int J Rock Mech Min Sci.* 2013;61(0): 43-56.

17. Backers T, Stephansson O, Rybacki E. Rock fracture toughness testing in Mode II—punch-through shear test. *Int J Rock Mech Min Sci.* 2002;39(6): 755-769.

18. Bell FG. *Engineering properties of soils and rocks*: Elsevier; 2013.

19. Stimpson B. Modelling materials for engineering rock mechanics. *International Journal of Rock Mechanics and Mining Sciences & Geomechanics Abstracts.* 1970;7(1): 77-121.

20. Yesiloglu-Gultekin N, Gokceoglu C, Sezer EA. Prediction of uniaxial compressive strength of granitic rocks by various nonlinear tools and comparison of their performances. *Int J Rock Mech Min Sci.* 2013;62(0): 113-122.

21. Nasseri MHB, Mohanty B. Fracture toughness anisotropy in granitic rocks. *Int J Rock Mech Min Sci.* 2008;45(2): 167-193.

22. Xu C. *Cracked Brazilian disc for rock fracture toughness testing: theoretical background, numerical calibration and experimental validation*: Verlag Dr. Muller; 2010.

23. Guo F, Morgenstern NR, Scott JD. An experimental investigation into hydraulic fracture propagation—Part 1. Experimental facilities. *Int J Rock Mech Min Sci.* 1993;30(3): 177-188.

24. Bieniawski Z, Bernede M. Suggested methods for determining the uniaxial compressive strength and deformability of rock materials. *International Journal of Rock Mechanics and Mining Sciences & Geomechanics Abstracts.* 16. Elsevier; 1979:138-140.

25. Fowell RJ. Suggested method for determining mode I fracture toughness using cracked chevron notched Brazilian disc (CCNBD) specimens. *International Journal of Rock Mechanics and Mining Sciences & Geomechanics Abstracts.* 32. Pergamon; 1995:57-64.

26. Tada H, Paris P, Irwin G. *The stress analysis of cracks handbook.* 3 ed: New York: ASME Press; 2000.

27. Rahman MK, Hossain MM, Rahman SS. An analytical method for mixed-mode propagation of pressurized fractures in remotely compressed rocks. *Int J Fract.* 2000;103(3): 243-258.

28. Young WC, Budynas RG. *Roark's formulas for stress and strain*: McGraw-Hill New York; 2002.

29. Sih GC, Liebowitz H. Mathematical theories of brittle fracture. In: Liebowitz H, ed. *Fracture. An Advanced Treatise.* Vol 2. Academic Press, Inc.; 1968:128-151.

30. Wawrzynek P, Carter B, Banks-Sills L. *The M-Integral for computing stress intensity factors in generally anisotropic materials*: National Aeronautics and Space Administration, Marshall Space Flight Center; 2005.

31. Erdogan F, Sih GC. On the crack extension in plates under plane loading and transverse Shear. *J Basic Eng.* 1963;85(4): 519-525.

32. Sih GC. Strain-energy-density factor applied to mixed mode crack problems. *Int J Fract.* 1974;10(3): 305-321.

33. Smith DJ, Ayatollahi MR, Pavier MJ. The role of T-stress in brittle fracture for linear elastic materials under mixed-mode loading. *Fatigue & Fracture of Engineering Materials & Structures.* 2001;24(2): 137-150.

34. Ayatollahi M, Aliha M, Hassani M. Mixed mode brittle fracture in PMMA—an experimental study using SCB specimens. *Mater Sci Eng: A.* 2006;417(1): 348-356.

Discussion

This thesis dealt with the initial conditions, i.e. magnitude of the internal pressures and directions of the fracture propagation surfaces, produced via hydraulic fracturing. The two conditions considered were a pressurised borehole within an intact rock and a notched section to represent a pre-existing crack. These initial conditions are important since they determine how the rock mass will behave during hydraulic fracturing. The predictions of breakdown pressures and resultant fracture propagation surfaces were achieved via analytical and numerical methods and theories. Experimental evidence was obtained to validate these approaches.

It was found that a pressurised circular crack realigns perpendicular to the remote minor principal stress direction in a distance at least three times the crack radius. However, this reorientating process is dependent on the breakdown pressure and the in-situ stress conditions. It was found that the realignment process occurs in a shorter distance when the resultant shear stress along the crack plane (produced from the remote principal stresses) is increased. Hence, this suggests that when the in-situ principal stress values are more deviatory, this will produce fracture propagation surfaces that are more planar. Therefore, when deciding which zones to hydraulically fracture the predicted shapes of the fracture propagation surfaces should be considered with respect to the pre-existing discontinuities and in-situ stress conditions. When predicting the fracture propagation surface from a pressurised circular crack the breakdown pressure can be used as the propagating pressure. However, it is suggested that a propagation algorithm, with varying pressure values for each quasi-static propagation step, could be developed to generate fracture propagation surfaces that are more realistic and aligned to the experimental results.

The breakdown pressures recorded for circular notches (representing cracks) when converted to mode I stress intensity factors, were closely aligned to the mode I fracture toughness of the material tested. The mode II (shear) stress intensity factors did not noticeably influence the breakdown pressures of these circular pressurised cracks. The maximum produced mode II stress intensity factors were about 30% of the mode I stress intensity factors generated at breakdown. This illustrates that to minimise the breakdown pressure magnitudes the notch should be positioned perpendicular to the minor principal stress direction and the discontinuities with the least normal stress values should be targeted.

For intact rock it was confirmed that the propagation surfaces produced via hydraulic fracturing were perpendicular to the remote minor principal stress direction. This means

the fracture surface can be determined accurately if the in-situ stresses are known prior to stimulation. Although, if there are discontinuities present in the rock mass this may alter the fracture network produced. The presence of multiple discontinuities was not addressed in this research, however, in reality they are present and can significantly influence the geometry of the fracture network.

In a structured experimental program it was shown that the recorded breakdown pressure values for intact homogeneous rock material are closely related to the remote minor principal stress values. For these tests, the breakdown pressure values were less related to the maximum tangential stress on the wall of these vertical boreholes $(3\sigma_h - \sigma_H)$, than the remote minor principal stress values. This suggests the remote minor principal stress value could be the only remote principal stress required to predict the breakdown pressures of intact rock.

By considering the initial conditions, i.e. internal pressures and fracture propagation surfaces, of two situations (intact and notched material) encountered when hydraulically fracturing rock, it was found that these mechanical processes can be predicted using fracture mechanics approaches. Hence, this research provides further understanding of the initial hydraulic fracturing process to assist with predicting its influence on rock masses.

Conclusions and recommendations

Hydraulic fracturing is a mechanical process commonly used in the resources industries to enhance the desired rock mass properties by creating induced fractures within the rock mass via pumping high pressure fluid into it. Since a rock mass can have pre-existing discontinuities, it is important to predict the interaction of the high pressure fluid and these pre-existing cracks to be able to design effectively the hydraulic fracturing treatments. This research focuses on understanding the behaviour of an arbitrarily orientated pre-existing crack, with respect to the external principal stress directions, intersecting a pressurised section of a borehole. The resultant fracture propagation surfaces have been predicted via developed analytical and numerical techniques, and verified by the experimental results. It has also been shown by the proposed approach that the breakdown (maximum injection) pressures of these configurations can be predicted effectively by the LEFM theory. In addition, the hydraulic fracturing experiments in an intact material confirmed that the fracture propagation surfaces aligned perpendicular to the minor principal stress direction. The experiments also provided evidence that the measured breakdown pressures are highly correlated to the magnitude of the minor principal stress.

Conclusions

- The three dimensional analytical technique proposed in Paper 1 provides an efficient method to predict the fracture propagation surface of a pressurised circular crack in a brittle rock material. This could potentially be a very useful tool for the energy and minerals industries.
    - This quasi-static analysis uses the maximum tangential stress criterion and the concept of an equivalent fictitious crack surface to approximate the fracture propagation surface.
    - This analytical method produces the final fracture propagation surfaces that realign perpendicular to the minor principal stress direction.
    - The fracture propagation surfaces align well with the published two dimensional fracture propagation paths.
- The hydraulic fracturing experimental study, investigating the role of a circular notch, to represent a crack, intersecting a pressurised borehole section on the breakdown pressures and fracture propagation surfaces, revealed that the LEFM theory could be used to predict these components:

- The mode I stress intensity factors at the breakdown of the circular cracks align well with the mode I fracture toughness of the material tested. Hence, under the shear stress conditions tested, the breakdown pressures of circular cracks in a brittle rock material can be predicted using the radius of the crack and the normal stress on the surface of the crack.
- The maximum tangential stress criterion provides fracture propagation surfaces that aligned well with the experimental results. In addition, increasing the magnitude of the shear stress on the surface of the circular crack decreases the distance that the fracture surface realigns orthogonal to the minor principal stress direction.
- In every experiment conducted the resultant fracture propagation surface realigned perpendicular to the minor principal stress direction.

- The hydraulic fracturing experiments, investigating the breakdown pressures of an intact material, confirmed the accuracy of the proposed theory to predict these values.
  - Conducting these experiments under the conventional triaxial compression conditions, in an ordered experimental design, revealed that there was a significant correlation between the magnitude of the minor principal stress and the breakdown pressures recorded.
  - There is a reduction in the breakdown pressure values under the remote hydrostatic stress conditions when compared to the remote non-hydrostatic stress states. This may be due to the production of multiple hydraulic fracture propagation surfaces in the remote hydrostatic stress conditions since; in this case, there is no preferred direction of fracture.
  - The predicted breakdown pressure distributions for the remote non-hydrostatic and hydrostatic stress states, using Monte Carlo simulations, align well with the measured breakdown pressure distributions, which demonstrate the effectiveness of the proposed theory when the uncertainty in the rock properties is considered.

Recommendations

- For the analytical approach, a coefficient should be derived to convert the current analytical stress intensity factors for the kinked crack to the numerical stress intensity factors. For example, this coefficient could be derived by the additional

shear stress induced from the initial planar crack surface to the planar fracture front.

- Under the same experimental setup, the normal stress on the plane of the circular crack should be increased incrementally to confirm its implied influence on the breakdown pressures.
- Different fluids should be used to investigate the influence of viscosity on the resultant fracture propagation surfaces from a circular crack intersecting a pressurised section of a borehole.
- Reproduction of the internal pressure versus time graphs, with respect to the fracture location, is required to model more accurately the fracture propagation surfaces of circular cracks. In particular, the relationship between the internal pressure versus time after breakdown, should be used to generate a fracture propagation algorithm.
- As this work only considers the influence of a single circular crack or notch, the effect of two or more cracks or notches, spaced in different configurations, on the fracture propagation surfaces and breakdown pressures should be investigated. This would involve further developing three dimensional numerical methods to study problems more closely related to reality.
- Intact materials, with transitional permeability values, should be investigated in the hydraulic fracturing experiments. This would either provide the threshold point to define impermeable and permeable materials used in the proposed approach or illustrate the characteristics of the transition of the breakdown pressure values in these materials.
- The gradual transition of the breakdown pressures, in an intact material, from the remote hydrostatic to non-hydrostatic stress conditions should be further studied.